Hubbard model with geometrical frustration

Dissertation
zur
Erlangung des Doktorgrades (Dr. rer. nat.)
der
Mathematisch-Naturwissenschaftlichen Fakultät
der
Rheinischen Friedrich-Wilhelms-Universität Bonn

vorgelegt von
Hunpyo Lee
aus
Kangnung, South Korea

Bonn, October 2009

Angefertigt mit Genehmigung der Mathematisch-Naturwissenschaftlichen Fakultät der Rheinischen Friedrich-Wilhelms-Universität Bonn.

1. Gutachter:	Prof. Dr. H. Monien
2. Gutachter:	Prof. Dr. R. Flume
Tag der Promotion:	8.10.2009
Erscheinungsjahr:	2010

Abstract

At first we present the details of the dual fermion (DF), the cluster extension of dynamical mean field theory (CDMFT) and continuous-time quantum Monte Carlo (CT QMC) methods. Using a panoply of these methods we explore the Hubbard model on the triangular and hyperkagome lattice. We find a first-order transition and continuous transition on the triangular and hyper-kagome lattice, respectively. Moreover, we find the reentrant behavior due to competition between the magnetic correlation and itinerancy of electrons by source of geometrical frustration on both lattices.

Contents

Chapter 1

Approximations and impurity solvers

1.1 Introduction

In compounds with the broad energy band, the electrons are highly itinerant and delocalized. These systems are well described as conventional band structure calculation (wave-like picture) [1], in which individual wavefunctions are calculated from an effective one-electron periodic potential. On the other hand, in compounds in the narrow energy band the electrons prefer to stay at a given site for longer time, because electron correlations between them are more important (particle-like picture). In a limitation in which all electrons prefer to stay at a given site, these compounds will become insulator which is called a Mott insulator [2]. However, it is difficult to understand a Mott physics in conventional band structure calculation. Most interesting compounds such as CuO [3] which shows the nature of high-temperature superconductivity and LiV_2O_4 [4] which exhibits the character of heavy fermion, coexist with the nature of the wave-like picture and particle-like picture. The simplest model is the Hubbard model with electron hopping and the Coloumb repsulsion which can describe such a system called the strongly correlated electron system. The simple diagram and Hubbard model to explain the wave-like and particle-like picture is plot in Fig. (1.1). Since development of computer, a variety of approximations and numerical methods were used to study the Hubbard model. Especially, remarkable numerical tools in the lattice calculation are quantum Monte Carlo (QMC) and exact diagonalization methods. These methods can directly calculate the physical quantities without any approximation in the given lattices. However, in spite of big contribution of these methods, they need an amount of computational time in a large system. Moreover, QMC method has a bad Fermionic sign problem at away half-filling case and in the frustration system. Due to these limitations of the QMC and exact diagonalization methods in the lattice calculation, the new approximation

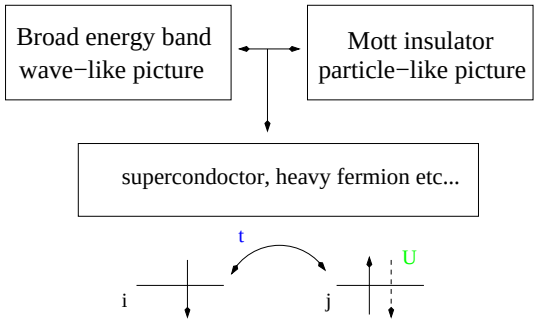

Figure 1.1: The simple diagram to explain the wave-like and particle-like picture.

methods are desirable.

The single-site dynamical mean field theory (DMFT) [5, 6, 7] is a big step to understand the strongly correlated systems in large dimensions. If we assume that the single-site impurity is connected to an external bath with an infinity coordination number, the lattice self-energy coincides with the local self-energy and all nonlocal self-energy terms have been disappeared. If this local self-energy is considered to be the averaged self-energy in the momentum space with a self-consistency condition, we can derive the DMFT equation. While this method can describe the Mott transition and the basic physics of heavy fermion compounds in the multi-band Hubbard model, it cannot capture the Ruderman-Kittel-Kasuya-Yosida (RKKY) interaction and d-wave superconductor due to lacks of non-local correlations. The cluster-extension of the DMFT methods, such as the dynamical cluster approximation (DCA) [8, 9] and the Cellular dynamical mean field theory (CDMFT) [10], are noteworthy methods to consider the short range fluctuations. The main idea of these methods is to reduce the complexity of the lattice problem by mapping to a finite-size cluster problem with self-consistent condition on the mean field level. They can treat correlations up to a cluster size accurately. These methods predict interesting results such as antiferromagnetic ground state [42], d-wave superconductor [12] and metal-insulator transition [39] in the Hubbard model. Recently, in order to describe long range correlations the approximation of new type, which is based on the single-site DMFT method, was developed. After solving the single-site DMFT problem exactly, new auxiliary fields are constructed by a dual transformation. Each lattice site can be viewed as a decoupled impurities in the the single-site DMFT while these impurities in this method, which is called the dual fermion (DF) method [11], are perturbatively coupled by auxiliary fields. Eventually, the nonlocal contributions are constructed to the DMFT from local two-particle vertex. In addition, the continuous-time QMC (CT QMC) methods [13, 14] were developed as cluster solvers. Unlike the traditional determinant QMC method [15], it can access low temperature region easily without the Tortter decomposition error.

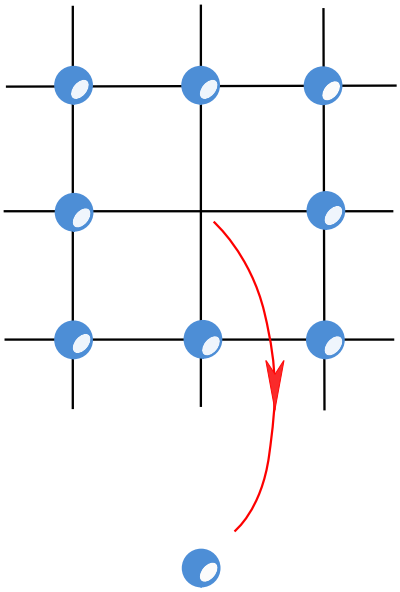

Figure 1.2: Cavity created in the full lattice by removing a single site and its adjacent bonds.

In this chapter we would like to present the single-site DMFT, cluster-extension of DMFT, DF methods as approximations and the CT QMC and semiclassical approximation (SCA) [16] methods as impurity (cluster) solvers.

1.2 Approximations

1.2.1 Dynamical mean field theory

To start with, I would like to introduce the dynamical mean field theory (DMFT) method [5, 6, 7] at a glance. The famous Hamiltonian of the Hubbard model is given as

$$H = \sum_{ij\sigma} t_{ij} c^{+}_{i,\sigma} c_{j,\sigma} + U \sum_{i} n_{i\uparrow} n_{i\downarrow}, \tag{1.1}$$

where $c_{i\sigma}(c^{+}_{i\sigma})$ is the annihilation (creation) operator of an electron with spin σ at the ith site, t_{ij} is the hopping matrix element and U represents the Coulomb repulsion. Its first limitation was introduced by W. Metzner and D. Vollhardt in 1989 [6]. They considered the model that a given lattice site is connected with an external bath, which is created by all other degree of freedom, like cavity construction in Fig. (1.2). They also assume that the coordination number between a given site and an external bath are infinity. The total action has three parts: $S = S^0 + S^{bath} + S^I$. Here S^0 is the action of single impurity, S^{bata} is non-interacting part and S^I is the hybridization

between impurity and bath. When the bath degree of freedom is integrated out, the effective action is given as

$$S_{eff} = -\int d\tau \int d\tau' \sum_{\sigma} c_{\sigma}^{+}(\tau) G_0^{-1}(\tau - \tau') c_{\sigma}(\tau') + U \int d\tau n_{\uparrow}(\tau) n_{\downarrow}(\tau), \tag{1.2}$$

where the bare Green's function $G_0(i\omega_n)$, which is only depended on frequency by the Fourier transformation, is

$$G_0^{-1}(i\omega_n) = i\omega_n + \mu - \triangle(i\omega_n), \tag{1.3}$$

and ω_n is the Matsubara frequency and $\triangle(i\omega_n)$ is the hybridization function. In this case, all diagrams except local term contributing to self-energy can be collapsed like:

$$\Sigma_{ij}(i\omega) = \delta_{ij}\Sigma(i\omega), \quad \Sigma(k, i\omega) = \Sigma(i\omega). \tag{1.4}$$

Now let us return as the original lattice model. In 1992 A. Georges and G. Kotliar approximated the lattice Green's function as an averaged local Green's function with self-consistent condition in the momentum space [7]. The lattice Green's function of the original lattice model is expressed as

$$G(k, i\omega_n) = \frac{1}{i\omega_n + \mu - \epsilon_k - \sum(k, i\omega_n)}. \tag{1.5}$$

Here they approximated the lattice Green's function into the local Green's function by summing over momentum k in Eq. (1.5):

$$G(i\omega_n) = \sum_k \frac{1}{i\omega_n + \mu - \epsilon_k - \sum(k, i\omega_n)}, \tag{1.6}$$

where ϵ_k is the bare dispersion relation and μ is the chemical potential. By Eq. (1.6) and Dyson's equation, which is given as

$$\sum(i\omega_n) = G_0^{-1}(i\omega_n) - G^{-1}(i\omega_n), \tag{1.7}$$

we can arrive at the self-consistent loop. The loop for the simulation is shown in below.

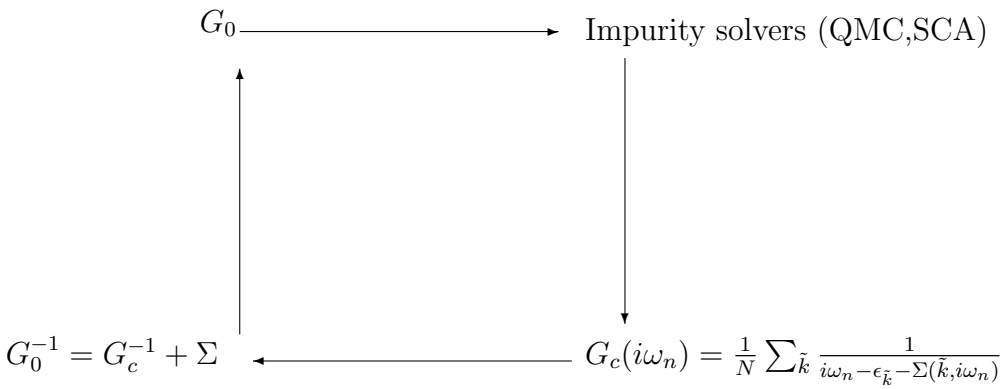

After several iterations, the converged Green's function is obtained.

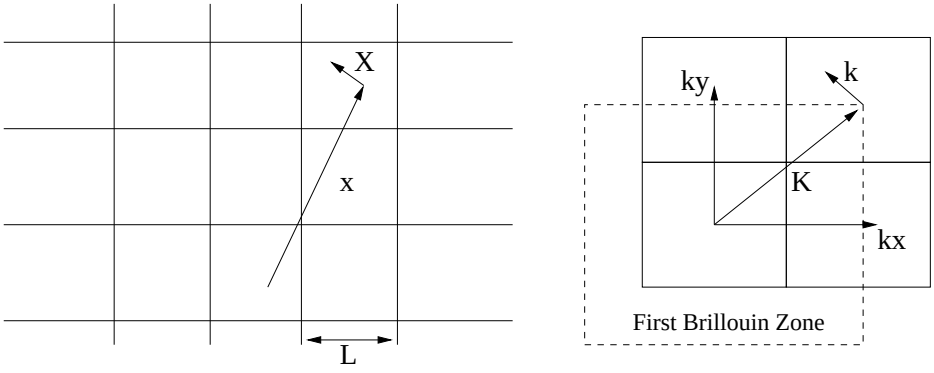

Figure 1.3: The example of the graphical cluster in real (left) and reciprocal (right) space. The origin of the cluster is labeled by x, and the sites within the cluster is labeled by X. The reciprocal space to X is labeled by K, and the wave vectors of the superlattice within a cell is labeled by k.

1.2.2 Cluster-extension of the DMFT method

In spite of success of the DMFT method [5, 6, 7], it cannot capture spin-liquid physics and d-wave superconductivity due to the lack of non-local fluctuations. In order to consider the non-local fluctuations, the dynamical cluster approximation (DCA) [8, 9] and cellular dynamical mean field theory (CDMFT) [10] were developed by Hettler et al. in 1998 and Kotliar et al. in 2001, respectively. Unlike the DMFT method which is considered as a single-site impurity problem with an external bath, the cluster degrees of freedom in these methods are separated out from the system. In this case the system is split into intracluster and intercluster parts:

$$t(x_i - x_j) = t_c \delta_{x_i,x_j} + \delta t(x_i - x_j) \tag{1.8}$$

$$\Sigma(x_i - x_j, i\omega) = \Sigma_c(i\omega)\delta_{x_i,x_j} + \delta\Sigma(x_i - x_j, i\omega) \tag{1.9}$$

All the quantities are $N_c \times N_c$ matrices in the cluster sites, t_c and Σ_c are the intracluster hopping and self-energy, while $\delta t(x)$ and $\delta\Sigma(x, i\omega)$ are intercluster quantities. The example of the graphical cluster is shown in Fig. (1.3). The origin of a cluster and the sites within a cluster are labeled by x and X, respectively. The reciprocal space to X and x are K and k. The site indices of the original lattice are $X + x$, and the wave vector in full Brillouin zone are given by $K + k$

Dynamical cluster approximation In the dynamical cluster approximation (DCA) method, the intercluster hopping $\delta t(\tilde{k})$ is finite for sites on the surface of the cluster and zero for bulk sites. It means that surface sites only hybridize with the host in

which the hopping matrix is given as

$$[t(\tilde{k})]_{X_i,X_j} = \frac{1}{N_c}\sum_{K} e^{iK(X_i-X_j)}e^{i\tilde{k}(X_i-X_j)}\epsilon_{K+\tilde{k}}. \tag{1.10}$$

The violation of translational symmetry is caused by the phase factors $e^{i\tilde{k}(X_i-X_j)}$ associated with the superlattice wave factor $\tilde{k}$. Due to omission of the superlattice wave factor $\tilde{k}$, we can freely sum over wave vector $\tilde{k}$ of the superlattice:

$$G_c(K, i\omega_n) = \sum_{\tilde{k}} G(K+\tilde{k}, i\omega_n) \tag{1.11}$$

and translational symmetry can be restored. In this method the Laue function is given as

$$\triangle_{DCA} = N_c\delta_{K_1+K_2+\ldots,K_1'+K_2'+\ldots}. \tag{1.12}$$

By thermodynamically consistent approximation developed by Baym and Kadanoff [See appendix [54, 53]], the DCA self-energy

$$\sum_{c}(K, i\omega_n) = \frac{\delta\Phi[G(K, i\omega_n, \bar{U})]}{\delta G(K, i\omega_n)} \tag{1.13}$$

depends on the cluster momenta K. Here $\bar{U}(K)$ is

$$\bar{U}(K) = \frac{N_c}{N}\sum_{\tilde{k}} U(K+\tilde{k}). \tag{1.14}$$

Since the grand potential is stationary with respect to G, the self-consistent condition for DCA method is

$$G(K, i\omega_n) = \frac{N_c}{N}\sum_{\tilde{k}}[G_0^{-1}(K+\tilde{k}, i\omega_n) - \sum_{c}(K, i\omega_n)]^{-1}, \tag{1.15}$$

with the bare Green's function $G_0(K+\tilde{k}, i\omega_n) = [i\omega_n - \epsilon_{K+\tilde{k}} + \mu]^{-1}$.

Cellular dynamical mean field theory The Green's function is given as

$$G(\tilde{x_i}-\tilde{x_j}, i\omega_n) = g(i\omega_n)\delta_{\tilde{x_i},\tilde{x_j}} + g(i\omega_n)\sum[\delta t(\tilde{x_i}-\tilde{x_j}) + \delta\sum(\tilde{x_i}-\tilde{x_j}, i\omega_n)]G(\tilde{x_i}-\tilde{x_j}, i\omega_n), \tag{1.16}$$

where $g(i\omega_n) = [(i\omega_n+\mu) - t_c - \sum_c(i\omega_n)]^{-1}$ is the Green's function of the cluster decoupled from remainder of the system. By the Fourier transformation of Eq. (1.16), the Green's function is rexpressed as

$$G(\tilde{k}, i\omega_n) = g(i\omega_n) + g(i\omega_n)[\delta t(\tilde{k}) + \delta\sum(\tilde{k}, i\omega_n)]G(\tilde{k}, i\omega_n). \tag{1.17}$$

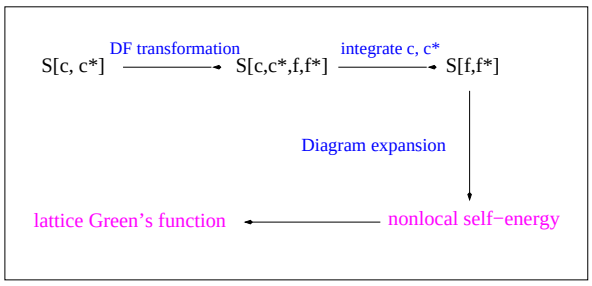

Figure 1.4: The simple diagram to explain the idea of the DF method.

In this method we neglect $\delta\sum$ and the Green's function becomes

$$G(\tilde{k}, i\omega_n) = g(i\omega_n) + g(i\omega_n)\delta t(\tilde{k})G(\tilde{k}, i\omega_n). \tag{1.18}$$

In the CDMFT method, the Laue function is given as

$$\triangle_{CDMFT} = \sum_X e^{iX(K_1+\tilde{k_1}+\cdots-K_1'-\tilde{k_1'}-\ldots)}. \tag{1.19}$$

Thus, the phase factors $e^{i\tilde{k}X}$ are kept and the phase factors $e^{i\tilde{k}\tilde{x}}$ are omitted. The grand potential is stationary with respect to the lattice Green's function. Finally, the self-consistent condition for CDMFT is give as

$$G(i\omega_n) = \frac{N_c}{N}\sum_{\tilde{k}}[G_0^{-1}(\tilde{k}, i\omega_n) - \sum(i\omega_n)]^{-1} \tag{1.20}$$

with the bare Green's function $G_0(i\omega_n) = [(i\omega_n + \mu)1 - t(\tilde{k})]^{-1}$.

1.2.3 Dual fermion method

The dual fermion (DF) method is relatively new method which is developed by A. Rubtsov et al. in 2008 [11]. The idea of the DF method is presented in Fig. (1.4).

- The dual fields f and f^* is constructed by a dual transformation.
- Integrate c and c^*.
- The self-energy is calculated by the diagram expansion.
- The lattice Green's function is calculated.

The cluster-extension of the DMFT method can describe the short range correlations in the cluster size exactly and consider the long range correlations on the mean field level, while the DF method constructs the nonlocal contributions to DMFT from two-particle vertex and includes the long range information. Based on the single-site DMFT method, there is no Fermionic sign problem in the QMC method and it is cheap in terms of computational time. Now we start explaining the detail formalism of the DF method.

Formalism I will give an example for 2D Hubbard model on the square lattice, and this formalism follows the original work of A. Rubtsov [11]. At the beginning, we consider the imaginary-time action which is given by

$$S[c,c^*] = \sum_{\omega k\sigma} (\epsilon_k - \mu - i\omega_n)\, c^*_{\omega k\sigma} c_{\omega k\sigma} + U \sum_i \int_0^\beta n_{i\uparrow\tau} n_{i\downarrow\tau} d\tau. \tag{1.21}$$

Here β and μ are the inverse temperature and chemical potential, respectively, $\omega_n = (2n+1)\pi/\beta, n = 0, \pm 1, ...$ are the Matsubara frequencies, $\sigma = \uparrow, \downarrow$ is the spin projection. The bare dispersion law of the 2D Hubbard model on the square lattice is $\epsilon_k = -2t(\cos k_x + \cos k_y)$, c^*, c are the Grassmann variables, $n_{i\sigma\tau} = c^*_{i\sigma\tau} c_{i\sigma\tau}$, where the indices i and k label sites and quasi-momenta. If we consider the single-site reference system which is connected with an external bath, we can rewrite the action which is given as

$$S[c,c^*] = \sum_i S_{imp}[c_i, c_i^*] - \sum_{\omega k\sigma} (\Delta_\omega - \epsilon_k) c^*_{\omega k\sigma} c_{\omega k\sigma}. \tag{1.22}$$

The impurity action at a given site is

$$S_{imp} = \sum_{\omega,\sigma} (\Delta_\omega - \mu - i\omega) c^*_{\omega,\sigma} c_{\omega,\sigma} + U \int_0^\beta n_{\uparrow\tau} n_{\downarrow\tau} d\tau. \tag{1.23}$$

The impurity Green's function and two-particle Green's function are obtained by CT QMC impurity solver in DMFT method. When we compare Eq. (1.21) with Eq. (1.23), the second term $(\Delta_\omega - \epsilon_k) c^*_{\omega k\sigma} c_{\omega k\sigma}$ of Eq. (1.22) is obtained and $\triangle_\omega$ is the hybridization function which is independent of k. By a dual transformation, we obtain a set of new Grassmann variables f and f^*. The following Gaussian identity (dual transformation) is

$$e^{A^2 c^*_{\omega k\sigma} c_{\omega k\sigma}} = B^{-2} \int e^{-AB(c^*_{\omega k\sigma} f_{\omega k\sigma} + f^*_{\omega k\sigma} c_{\omega k\sigma}) - B^2 f^*_{\omega k\sigma} f_{\omega k\sigma}} df^*_{\omega k\sigma} df_{\omega k\sigma}, \tag{1.24}$$

where $A^2 = (\Delta_\omega - \epsilon_k)$ and $B^2 = g_\omega^{-2} (\Delta_\omega - \epsilon_k)^{-1}$ for each set of indices ω, k, σ. With this identity, the partition function of the lattice problem $Z = \int e^{-S[c,c^*]} \mathcal{D}c^* \mathcal{D}c$ can be presented as a form $Z = Z_f \int\int e^{-S[c,c^*,f,f^*]} \mathcal{D}f^* \mathcal{D}f \mathcal{D}c^* \mathcal{D}c$, where

$$S[c,c^*,f,f^*]=\sum_i S_{imp}[c_i,c_i^*]+\sum_{\omega k\sigma}\left[g_\omega^{-1}(f^*_{\omega k\sigma}c_{\omega k\sigma}+c^*_{\omega k\sigma}f_{\omega k\sigma})+g_\omega^{-2}(\Delta_\omega-\epsilon_k)^{-1}f^*_{\omega k\sigma}f_{\omega k\sigma}\right] \tag{1.25}$$

and Z_f is a product $\Pi_{\omega k}g_\omega^2(\Delta_\omega-\epsilon_k)$. In Eq. (1.25), we concentrate on the coupling term $\sum_{\omega k\sigma}(f^*_{\omega k\sigma}c_{\omega k\sigma}+c^*_{\omega k\sigma}f_{\omega k\sigma})$. Because of integration over c and c^* separately for each site, we can define that $\Sigma_k\left(f_k^*c_k+c_k^*f_k\right)$ coincides with $\Sigma_i\left(f_i^*c_i+c_i^*f_i\right)$. For more detail calculation we split Eq. (1.25) into S_{ccff} and S_{ff}:

$$S_{ccff}=\sum_i S_{imp}[c_i,c_i^*]+\sum_{\omega k\sigma}[g_\omega^{-1}(f^*_{\omega k\sigma}c_{\omega k\sigma}+c^*_{\omega k\sigma}f_{\omega k\sigma})] \tag{1.26}$$

$$S_{ff}=\sum_{\omega k\sigma}[g_\omega^{-2}(\Delta_\omega-\epsilon_k)^{-1}f^*_{\omega k\sigma}f_{\omega k\sigma}] \tag{1.27}$$

$$S[c,c^*,f,f^*]=S_{ccff}+S_{ff}. \tag{1.28}$$

We would like to expand $e^{\sum_{\omega k\sigma}[g_\omega^{-1}(f^*_{\omega k\sigma}c_{\omega k\sigma}+c^*_{\omega k\sigma}f_{\omega k\sigma})]}$ over f and f^* in Eq. (1.26) by fourth order terms. In our calculation we neglect the higher order terms. The following equation is

$$e^{\sum_i[g_w^{-1}(f_i^*c_i+c_i^*f_i)]}\approx\sum_i[g_w^{-1}f^*f+\gamma^{(4)}_{1234}f_1^*f_2f_3^*f_4]. \tag{1.29}$$

The odd terms have been vanished by the Grasmann integration and the $\gamma^{(4)}_{1234}$ is the exact four-point reducible vertex for the original fermions which plays the role of the bare effective two-particle interaction for the dual fermion. By energy conservative law the $\gamma^{(4)}_{1234}$ is given as

$$\gamma^{(4)}_{1234}(\omega_1,\omega_2,\omega_3,\omega_2-\omega_1-\omega_3)=\frac{\langle c_1^*c_2c_3^*c_4\rangle-g_{14}g_{23}+g_{13}g_{24}}{g_{11}g_{22}g_{33}g_{44}}. \tag{1.30}$$

We can obtain a new action through reweighting Eq. (1.29). The new action is

$$\int e^{-S_{site}}\mathcal{D}c_i^*\mathcal{D}c_i=Z_{imp}e^{(-\sum_{\omega\sigma}g_\omega^{-1}f^*_{\omega i\sigma}f_{\omega i\sigma}-\gamma^{(4)}_{1234}f_1^*f_2f_3^*f_4)}, \tag{1.31}$$

where Z_{imp} is a partition function of the impurity problem in Eq. (1.23). Now we combine S_{ff} and Eq. (1.31) in order to obtain an action S which depends only on the new variable f and f^*. The action is given by

$$S[f,f^*]=\sum_{\omega k\sigma}g_\omega^{-2}\left((\Delta_\omega-\epsilon_k)^{-1}+g_\omega\right)f^*_{\omega k\sigma}f_{\omega k\sigma}+\sum_i V_i, \tag{1.32}$$

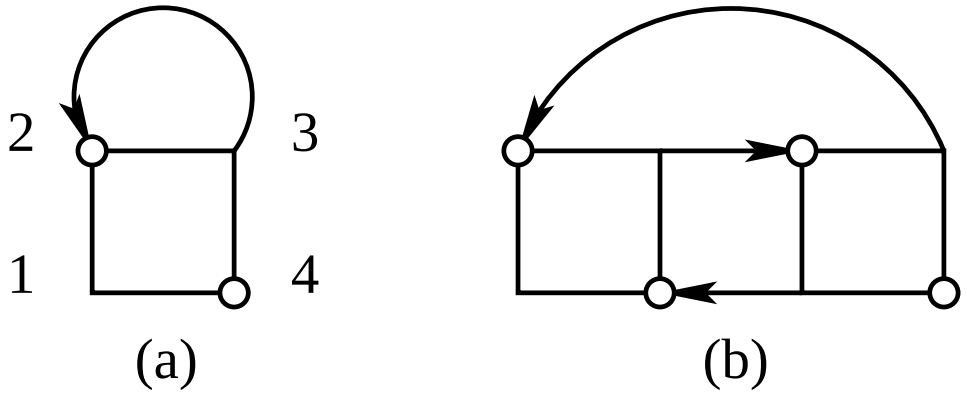

Figure 1.5: The first-order (a) and second-order (b) dual self-energy diagrams. They are composed of the local two-particle vertex function γ^4 (indicated as boxs) and the renormalized dual Green's functions (indicated as lines).

where V_i is $-\gamma^{(4)}_{1234} f^*_1 f_2 f^*_3 f_4$. Now we can establish an exact relation between the lattice Green's function $G_{\omega,k}$ and the partition function Z. For this we define $G^{daul}_{\omega,k} = -\langle T_\tau f f^* \rangle$ and the lattice Green's function $G_{\omega,k}$ is calculated by

$$G_{\omega,k} = -\frac{1}{Z}\frac{\delta Z}{\delta \epsilon_k} \tag{1.33}$$

$$G_{\omega,k} = g_\omega^{-2}(\Delta_\omega - \epsilon_k)^{-2} G^{dual}_{\omega,k} + (\Delta_\omega - \epsilon_k)^{-1}, \tag{1.34}$$

where g_ω is the impurity Green's function determined by the single-site DMFT method. From Eq. (1.32), the bare dual Green's function is

$$G_0^{(dual)} = g_\omega^{-2}[(\Delta_\omega - \epsilon_k)^{-1} + g_\omega]. \tag{1.35}$$

A regular diagrammatic expansion in powers of V_i in each site can be performed. We draw skeleton diagram in Figs. (1.5(a)-(b)) by the second-order. The lines in diagrams are the renormalized dual Green's functions and the vertices are $\gamma^{(4)}$. In this approximation we only consider the first-order in Fig. (1.5(a)) and the second-order diagram in Fig. (1.5(b)). The first-order diagram vanishes in the bare DF because the diagram exactly corresponds to the DMFT self-consistent condition which is only depended on one frequency. Therefore, the first non-local contribution is given by the second-order diagram because $\gamma^{(4)}$ is nonlocal in imaginary time. The self-energy

for these two diagrams is

$$\Sigma^{(1)}_{\sigma}(k) = -\frac{T}{N^d}\sum_{\sigma',k'} G^d_{\sigma'}(k')\gamma^{(4)}_{\sigma\sigma'}(\omega,\omega';\omega',\omega), \tag{1.36a}$$

$$\begin{aligned}\Sigma^{(2)}_{\sigma}(k_1) = -\frac{T^2}{2N^{2d}}\sum_{2,3,4} & G^d_{\sigma_2}(k_2)G^d_{\sigma_3}(k_3)G^d_{\sigma_4}(k_4) \\ & \gamma^{(4)}_{\sigma_{1234}}(\omega_1,\omega_2;\omega_3,\omega_4)\gamma^{(4)}_{\sigma_{4321}}(\omega_4,\omega_3;\omega_2,\omega_1) \\ & \delta_{k_1+k_2,k_3+k_4}\delta_{\sigma_1+\sigma_2\sigma_3+\sigma_4}.\end{aligned} \tag{1.36b}$$

Together with the bare dual fermion Green's function $G^d_0(k) = -g^2_\nu/[(\Delta_\nu - \epsilon_k)^{-1} + g_\nu]$, the new dual Green's function can be derived from the Dyson equation which is expressed by

$$[G^d(k)]^{-1} = [G^d_0(k)]^{-1} - \Sigma^d(k). \tag{1.37}$$

This formula leads to the conserving theories exactly given by

$$\frac{\delta\Phi^{dual}}{\delta G^{dual}} = \Sigma^{dual} \tag{1.38}$$

$$\Sigma^{(dual)}_{\omega,k} = G^{-1(dual)}_{0\omega,k} - G^{-1(dual)}_{\omega,k}, \tag{1.39}$$

In order to decide $\triangle_\omega$ we employ the DMFT self-consistent condition which is given by

$$\sum_k G^{(dual)}_{\omega,k} = \sum_k g^{-2}_\omega[(\Delta_\omega - \epsilon_k)^{-1} + g_\omega] = 0. \tag{1.40}$$

Since the diagram (a) in Fig. (1.5) is exactly zero in the bare DF Green's function (DMFT self-consistency condition), nonlocal contributions come from the second diagram (b) in Fig. (1.5), where the renormalized DF Green's function is updated from Eq. (1.37). As a result, the hybridization function should also be updated before the next DMFT loop is performed . This is simply done by setting the local full DF Green's function to zero, together with the condition that the old hybridization function forces the bare local DF Green's function to be zero ($\sum_k G^{0,d}_{\nu,k} = 0$), we obtain a set of equations

$$\frac{1}{N}\sum_k [G_{\omega,k} - (\Delta^{New}_\omega - \epsilon_k)^{-1}]g^2_\omega(\Delta^{New}_\omega - \epsilon_k)^2 = 0 \tag{1.41a}$$

$$\frac{1}{N}\sum_k [G^0_{\omega,k} - (\Delta^{Old}_\omega - \epsilon_k)^{-1}]g^2_\omega(\Delta^{Old}_\omega - \epsilon_k)^2 = 0 \tag{1.41b}$$

which yields

$$\Delta^{New}_\omega - \Delta^{Old}_\omega \approx \frac{1}{N}\sum_k (G_{\omega,k} - G^0_{\omega,k})(\Delta^{Old}_\omega - \epsilon_k)^2. \tag{1.42}$$

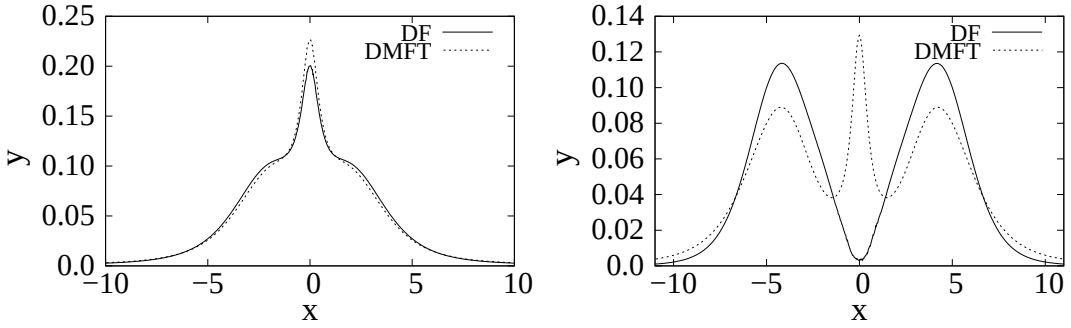

Figure 1.6: Local density of states for the 2D Hubbard model at half-filling obtained from DMFT and DF calculation for U/t=4 and U/t=8 at β=4.5. An x-axis and y-axis indicate the Fermi energy and local density of states, respectively. [Phys. Rev. B. 77, 195105 (2008) [17]]

This equation finally gives us the relation between the new and old hybridization function:

$$\Delta_\omega^{New} = \Delta_\omega^{Old} + g_\omega^2 G_{loc}^d. \tag{1.43}$$

With this method we can explore the physics in both weak-coupling and strong-coupling regions, unlike other perturbative approaches which can cover the weak-coupling regions. If U is small in the weak-coupling region, $\gamma^{(4)}$ is proportional to U. In the self-energy diagram given by Figs. (1.5(a)-(b)), the vertices (box in Fig. (1.5)) will also be small. On the other hand, the renormalized dual Green's function (line in Fig. (1.5)) in the diagram is small in the strong-coupling regions. This makes a diagrammatic expansion in the strong-coupling regions. In Fig. (1.6) we present the density of states for the 2D Hubbard model at half-filling in both weak-coupling region (U/t=4) and strong-coupling region (U/t=8) [17]. In the weak-coupling region the result obtained with the DMFT method is very close to that obtained with the DF method. However, while the DMFT is still stable the metallic state in the strong-coupling regions, the DF captures the gap structure which is caused by the nonlocal fluctuations.

Practical procedure for simulation I present the details of algorithm for the DF method.

1. Obtain the converged impurity Green's function g_ω in the single-site DMFT method.

2. Decide an initial value of $\triangle_\omega$ from Eq. (1.40). The self-consistency condition of the DMFT method ensures that the first diagram of the DF self-energy is

zero in Eq. (1.40). We initially use $\triangle_\omega$ calculated by

$$\triangle_\omega = i\omega_n - \frac{1}{g_0(i\omega_n)}, \tag{1.44}$$

where $g_0(i\omega_n)$ is the Weiss field in the single-site DMFT method. In principle, this relation is exact. However, in order to obtain $\triangle_\omega$ very accurately, we employ the iteration method given by

$$\triangle_\omega = \frac{\sum \frac{\epsilon_k}{g_\omega(\triangle_\omega - \epsilon_k)+1)}}{\sum \frac{1}{g_\omega(\triangle_\omega - \epsilon_k)+1)}}. \tag{1.45}$$

The Eq. (1.45) and Eq. (1.40) are the same.

3. Go through the DMFT loop once again to calculate the two-particle Green's function which is related to the vertex function γ^4. In the CT QMC part, we will introduce how to calculate it in more detail.

4. Determine the converged dual Green's function and in the end the lattice Green's function by Eq. (1.34).

   (a) Calculate the dual self-energy from Eq. (1.36a), (1.36b) and the Dyson equation Eq. (1.37)

   (b) Repeated use Eq. (1.36a), (1.36b) and Eq. (1.37) until the converged dual fermion Green's function is obtained.

   (c) The lattice Green's function is given by Eq. (1.34).

5. Calculate the local lattice Green's function by summing over momentum space. Determine a new hybridization function $\triangle_\omega$ from the on-site Green's function and the old hybridization function in Eq. (1.43).

6. Go back to the step 3 and iteratively perform until the hybridization $\triangle_\omega$ does not change any more. The symmetric figure for simulation is introduced next page.

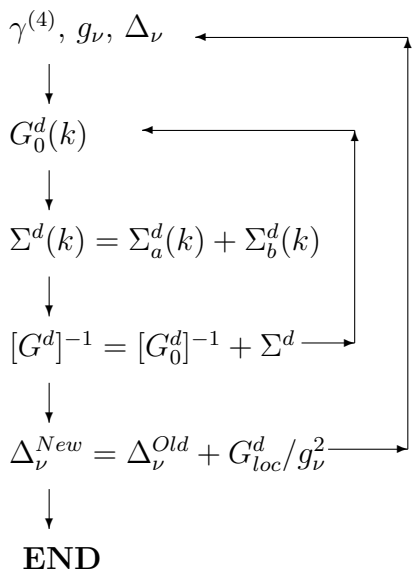

The two-particle properties for DF method In the lattice QMC or cluster-DMFT method it takes substantial effort to calculate the two-particle properties. On the other hand, one can calculate them through simple approximation [17, 18, 19] in the DF method without computational difficulty. In this part we will present the formalism for the two-particle properties and discuss the results. The two-particle properties are analogously derived to the single-particle Green's function. The definition of the two-particle properties is

$$\chi = \frac{1}{Z}\frac{\delta^2 Z}{\delta\epsilon_k \epsilon_{k'}} = -\frac{1}{Z}\frac{\delta}{\delta\epsilon_k}(ZG_{\omega k\sigma}), \tag{1.46}$$

where the lattice Green's function $G_{\omega k\sigma}$ is given by Eq. (1.34). By expanding Eq. (1.46), χ is reexpressed as

$$\chi = G_{\omega k\sigma}G_{\omega k\sigma} - \frac{\delta G_{\omega k\sigma}}{\delta\epsilon k}, \tag{1.47}$$

with

$$\frac{\delta G_{\omega k\sigma}}{\delta_{\epsilon k}} = (\triangle_\omega - \epsilon_k)^{-2}(1 + 2g_\omega^{-2}(\triangle_\omega - \epsilon_k)^{-1}G_k^{dual} + g_\omega^{-2}\frac{\delta G_k^{dual}}{\delta\epsilon_k}). \tag{1.48}$$

The $\frac{\delta G_k^{dual}}{\delta\epsilon_k}$ is given as

$$\frac{\delta G_k^{dual}}{\delta\epsilon_k} = g_\omega^- 2(\triangle_\omega - \epsilon_k)^- 2(G_{\omega k\sigma}^{dual}G_{\omega k\sigma}^{dual} - \chi^{dual}). \tag{1.49}$$

The lattice susceptibility is expressed as

$$\chi = (\triangle_\omega - \epsilon_k)^{-2}(1 + 2g_\omega^{-2}(\triangle_\omega - \epsilon_k)^{-1}G_k^{daul} + g_\omega^{-2} + g_\omega^{-4})(G_{\omega k\sigma}^{dual}G_{\omega k\sigma}^{dual} - \chi^{dual}). \tag{1.50}$$

Now we would like to calculate the full vertex function through solving the Bethe-Salpeter equation. In this dissertation, we will only calculate the dual two-particle properties which can capture the basic physics. If reader would like to see the full lattice two-particle properties, we refer the reader to our paper. The full dual vertex Γ is defined by

$$\chi^{\sigma\sigma'}_{\omega_1\omega_2\omega_3\omega_4} = G^{\sigma}_{\omega_1} G^{\sigma'}_{\omega_3} \Gamma^{\sigma\sigma'}_{\omega_1,\omega_2,\omega_3,\omega_4} G^{\sigma}_{\omega_2} G^{\sigma'}_{\omega_4} + G^{\sigma}_{\omega_1} G^{\sigma'}_{\omega_3} - \delta_{\sigma\sigma'} G^{\sigma}_{\omega_2} G^{\sigma'}_{\omega_4}, \tag{1.51}$$

where we omit the "dual" index and all quantities are only depended on dual variable. We will just use the bare four-point interaction γ^4 as the irreducible vertex and will not go beyond this approximation for the simulation. The three different Bethe-Salpeter equations, based on γ^4, are exhibited in Fig. (1.7). The first diagram represents the particle-particle (pp) channel and the two diagrams are in the particle-hole (ph) channel. The two ph-channels (ph) are distinguished from each other by the total spin (0,1) of the scattered particle-hole pair. The Bethe-Salpeter equations in the singlet and triplet particle-hole (ph) channels are

$$\begin{aligned} \Gamma^{ph0,\sigma\sigma'}_{\omega\omega'\Omega}(q) = \gamma^{\sigma\sigma'}_{\omega\omega'\Omega} \quad - \quad & \frac{1}{\beta N^d} \sum_{\omega''\sigma''} \sum_{k} \gamma^{\sigma\sigma''}_{\omega\omega''\Omega} G^{\mathrm{d}\sigma''}_{\omega''}(k) \times \\ & \times G^{\mathrm{d}\sigma''}_{\omega''+\Omega}(k+q)\, \Gamma^{ph0,\sigma''\sigma'}_{\omega''\omega'\Omega}(q) \end{aligned} \tag{1.52}$$

$$\begin{aligned} \Gamma^{ph1,\sigma\bar{\sigma}}_{\omega\omega'\Omega}(q) = \gamma^{\sigma\bar{\sigma}}_{\omega\omega'\Omega} \quad - \quad & \frac{1}{\beta N^d} \sum_{\omega''} \sum_{k} \gamma^{\sigma\bar{\sigma}}_{\omega\omega''\Omega} G^{\mathrm{d}\bar{\sigma}}_{\omega''}(k) \times \\ & \times G^{\mathrm{d}\sigma}_{\omega''+\Omega}(k+q)\, \Gamma^{ph1,\sigma\bar{\sigma}}_{\omega''\omega'\Omega}(q)\ , \end{aligned} \tag{1.53}$$

where Ω and ω denote the Bosonic and Fermionic Matsubara frequency, respectively. Here, γ is the irreducible vertex and $G^{d\sigma}_{\omega}$ denotes the fully self-consistent nonlocal dual Green's function. Now we would like to discuss how to solve the Bethe-Salpeter equations. The simplest methods is iterative one. The following procedure is:

1. Calculate the dual Green's function and Γ=$\gamma^{(4)}$.
2. Input Γ=$\gamma^{(4)}$ into Eq. (1.52) and (1.53).
3. Obtain new $\Gamma^{(1)}$ by the Bethe-Salpeter equations in Eq. (1.52) and (1.53).
4. Replace Γ=$\Gamma^{(1)}$ and calculate new $\Gamma^{(2)}$.
5. Repeat Step. [2] and Step. [3] and then obtain converged Γ.

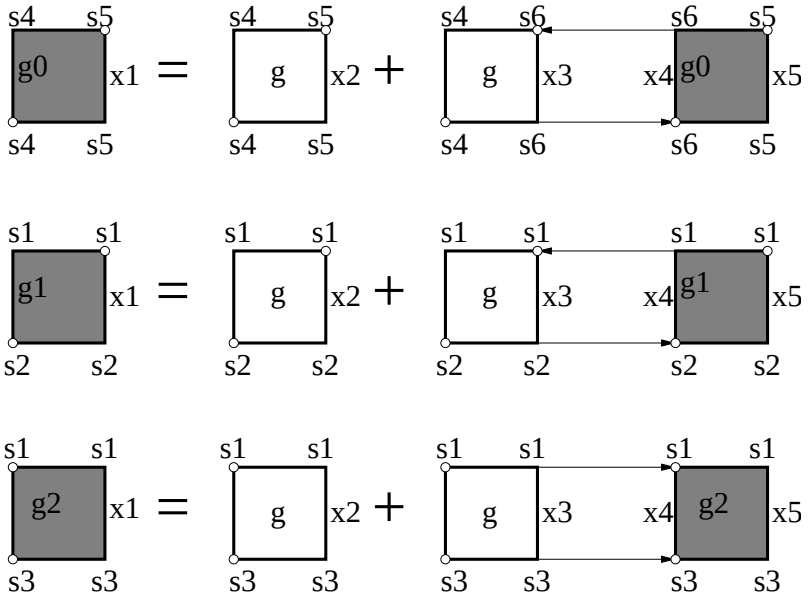

Figure 1.7: The Bethe-Salpeter equation in three different channels. The γ^4 is used as the irreducible vertex function. [Phys. Rev. B. 77, 195105 (2008) [17]]

We can also solve the Bethe-Salpeter equations by the inversion of matrix. However, close to the instability, one is faced with the problem of inverting a matrix with a very small determinant value. Once a converged solution for the two-particle vertex Γ is obtained, for paramagnetic case we have

$$\langle S_z\, S_z\rangle(\Omega,q) = \frac{1}{2}(\langle n_\uparrow\, n_\uparrow\rangle - \langle n_\uparrow\, n_\downarrow\rangle)(\Omega,q)\ , \tag{1.54}$$

where $\langle n_\sigma\, n_{\sigma'}\rangle(\Omega,q) = \chi_0^{\sigma\sigma'}(\Omega,q) + \chi^{\sigma\sigma'}(\Omega,q)$. The bubble diagram is

$$\tilde{\chi}_0^{\sigma\sigma'}(\Omega,q) = -\frac{1}{\beta N^d}\sum_{\omega}\sum_{k} G_{\omega}^{\mathrm{d}\sigma}(k) G_{\omega+\Omega}^{\mathrm{d}\sigma'}(k+q)\ , \tag{1.55}$$

and nontrivial part of the susceptibility is given by

$$\begin{aligned}\tilde{\chi}^{\sigma\sigma'}(\Omega,q) = \\ \frac{1}{\beta^2 N^{2d}}\sum_{\omega\omega'}\sum_{k,k'} \Gamma_{\omega\omega'\Omega}^{ph0,\sigma\sigma'}(q) G_{\omega}^{\mathrm{d}\sigma}(k) G_{\omega+\Omega}^{\mathrm{d}\sigma}(k+q) \times \\ \times G_{\omega'}^{\mathrm{d}\sigma'}(k') G_{\omega'+\Omega}^{\mathrm{d}\sigma'}(k'+q)\ .\end{aligned} \tag{1.56}$$

Finally, the spin susceptibility is obtained by Eq. (1.54). In Fig. (1.8), the DF

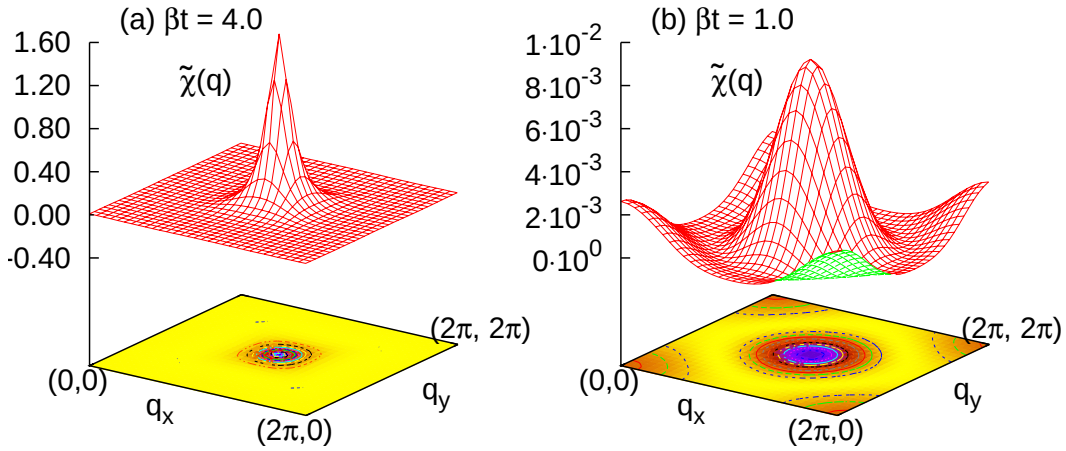

Figure 1.8: The nontrivial part of the DF spin susceptibilities as a function of momentum in 2D Hubbard model for U/t=4.0, βt=1.0 (right panel) and βt=4.0 (right panel).

spin susceptibilities are shown for U/t=4.0 at temperature βt=4.0 (left panel) and βt=1.0 (right panel) for 2D Hubbard model on the square lattice at half-filling. The momentum $\chi(q_x, q_y)$ is run from 0 to 2π. In the high temperature region (right panel), the all values of DF spin susceptibility are small because thermal fluctuations destroy the AF order. At low temperature region (left panel), the momentum $\chi(\pi, \pi)$ is increased rapidly. This means the enhancement of AF states. To clarify the simulation we calculate $\chi(\pi, \pi)$ and $\chi(\pi, \pi)$ as a function of temperature in Fig. (1.2.3). As temperature is decreased, the susceptibility strongly peaks at wave vector (π,π) which is shown the evidence of the antiferromagnetic instability.

1.3 Impurity solvers

1.3.1 Continuous-time quantum Monte Carlo method

The Hirsch-Fye quantum Monte Carlo (HFQMC) Method [15] has been used as an impurity solver successfully during last twenty years. The basic idea of this method is to discretize the imaginary time into N slices by the Trotter decomposition $\Delta\tau = \beta/N$ and to decouple the interaction term by the Hubbard-Stratonovich transformation. The random work of the HFQMC method is visited by Ising-like spin of the discrete auxiliary field. The limitation of this method is that the accuracy depends on the matrix size given by the Trotter decomposition which determines

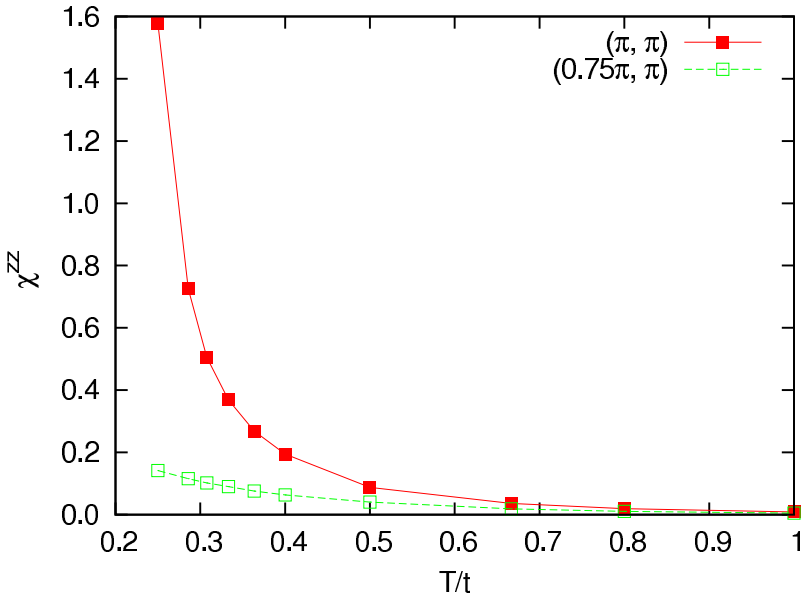

Figure 1.9: The dual susceptibility for different k points as a function of temperature. The divergence of χ(q) at q=(π , π) indicated the antiferromagnetic instability.

to computational time. The main point is that the matrix size scales by $\langle k \rangle \sim 2N_cU\beta$ in order to obtain the reliable results in the HFQMC. It is not easy to perform calculation at low temperature or large cluster due to the large matrix size. Moreover, since the Green's functions are measured in the imaginary time space, the error is happened in the process of Fourier transformation in the DMFT self-consistent equation. Recently, A. Rubtsov et al. and P. Werner et al. suggested weak-coupling expansion [13] and hybridization-coupling expansion [14] methods, respectively. Unlike the HFQMC method which is carried out by interacting over the auxiliary Ising-like spins, these QMC methods perform a random walk in the space of the perturbation expansion and imaginary time without the Trotter error. So it is called the continuous-time quantum Monte Carlo (CT QMC) method because there is no Trotter error. Concerning computational time, the weak-coupling CT QMC scales on $\langle k \rangle \sim 0.5N_cU\beta$ and is also superior to the HFQMC method. Another advantage is that because the Green's functions are measured in the Matsubara frequency space directly unlike the HFQMC method, the errors in process of the Fourier transformation are removed. Moreover, the hybridization-coupling CT QMC in the single-site impurity problem has much smaller computational burden than the weak-coupling CT QMC and HFQMC methods. We will discuss the weak-coupling CT QMC method and in the last part of this section refer to the hybridization-coupling CT QMC method shortly and point out the advantages and limitations of both CT QMC methods.

Formalism In order to discuss the weak-coupling CT QMC method I will consider the single-site impurity problem as a simple example. The starting point of this method is to spilt the total action into unperturbed part and interaction part. The unperturbed and interaction part of the action are given as

$$S_0 = -\int d\tau d\tau' \sum_\sigma c_\sigma(\tau) G_\sigma(\tau-\tau')^0 c^\dagger_\sigma(\tau'), \tag{1.57}$$

and

$$S_U = U\int d\tau[(n_\uparrow(\tau)-\frac{1}{2})(n_\downarrow(\tau)-\frac{1}{2})], \tag{1.58}$$

respectively. To obtain a more symmetric form we decompose $(n_\uparrow-\frac{1}{2})(n_\downarrow-\frac{1}{2})$ into

$$(n_\uparrow-\frac{1}{2})(n_\downarrow-\frac{1}{2}) = \frac{1}{2}\Big[(n_\uparrow+\alpha)(n_\downarrow-1-\alpha)+(n_\uparrow-1-\alpha)(n_\downarrow+\alpha)\Big], \tag{1.59}$$

and introduce α to remove or suppress the bad Fermionic sign problem because the term $-U^k$ leads the sign problem in the cases of repulsive interaction or away-half filling. In Eq. (1.59), we redefine $(n_\uparrow+\alpha)(n_\downarrow-1-\alpha)$ and $(n_\uparrow-1-\alpha)(n_\downarrow+\alpha)$ into $S_\uparrow$ and $S_\downarrow$, respectively. During performing QMC update, $S_\uparrow$ and $S_\downarrow$ are selected randomly. At half-filling, the α technic can not only remove the Fermionic sign problem completely, it but also can decrease the expansion order k related to computational time dramatically. Now we would like to expand $Z = TrT_\tau e^{-(S_0+S_U)}$ in powers of U. The partition function is given by

$$\begin{aligned} Z &= \sum_k \frac{(-U)^k}{k!}\int d\tau_1\dots d\tau_k TrT_\tau e^{-S_0} \\ &\quad\times <(n_\uparrow(\tau_1)+\alpha)(n_\downarrow(\tau_1)-1-\alpha)...(n_\uparrow(\tau_k)-1-\alpha)(n_\downarrow(\tau_k)+\alpha)> \end{aligned} \tag{1.60}$$

where T_τ is the time-ordering operator. We will use $D_{\mathcal{G}_0,\sigma}(\tau_1,...,\tau_k)(i,j)$ instead of $<(n_\uparrow(\tau_1)+\alpha)(n_\downarrow(\tau_1)-1-\alpha)...(n_\uparrow(\tau_k)-1-\alpha)(n_\downarrow(\tau_k)+\alpha)>$. The $D_{\mathcal{G}_0,\sigma}(\tau_1,...,\tau_k)(i,j)$ is matrix which is determined by the Wick's theorem and the non-interacting Green's function, like

$$D_{\mathcal{G}_0,\sigma}(\tau_1,\dots,\tau_k)(i,j) = \begin{pmatrix} \mathcal{G}^0_\sigma(0)-\alpha & \mathcal{G}^0_\sigma(\tau_1-\tau_2) & \cdots & \mathcal{G}^0_\sigma(\tau_1-\tau_k) \\ \mathcal{G}^0_\sigma(\tau_2-\tau_1) & \mathcal{G}^0_\sigma(0)-\alpha & \cdots & \mathcal{G}^0_\sigma(\tau_2-\tau_k) \\ \vdots & \vdots & \cdots & \vdots \\ \mathcal{G}^0_\sigma(\tau_k-\tau_1) & \mathcal{G}^0_\sigma(\tau_k-\tau_2) & \cdots & \mathcal{G}^0_\sigma(0)-\alpha \end{pmatrix}.$$

Here α is selected randomly by $S_\uparrow$ and $S_\downarrow$. In the Fermionic case, the perturbation order k in Eq. (1.60) is converged because $k!$ in denominator should be increased faster than the eigenstates in numerator. In the Bosonic case, it is impossible to simulate with this method since the eigenstates in numerator are diverging. The

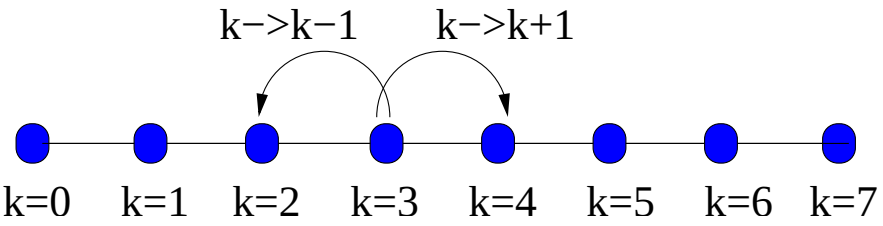

Figure 1.10: Schematic picture of random walks in the perturbation space.

Monte Carlo process is performed by increasing $k \to k+1$ or decreasing $k \to k-1$ like Fig. (1.10). An example of distribution for the perturbation order k is exhibited in Fig. (1.11). The distribution in Fig. (1.11) has a Gaussian form at α=0.001 and the perturbation order is converged around k=100. The Green's function is defined by

$$G(\tau-\tau') = Z^{-1} < Tc^{+}(\tau)c(\tau')e^{-U} >= \int d\tau_1 \dots d\tau_k g(\tau_1, \dots, \tau_k) D_{\mathcal{G}_0,\sigma}(\tau_1, ..., \tau_k)(i,j), \tag{1.61}$$

where $g(\tau_1, \dots, \tau_k)$ is

$$g(\tau_1, \dots, \tau_k) = D_{\mathcal{G}_0,\sigma}(\tau_1, ..., \tau_k)(i,j)^{-1} < T_\tau c^{+}(\tau)c(\tau')c^{+}(\tau_1)c(\tau_1), \dots, c^{+}(\tau_k)c(\tau_k) > . \tag{1.62}$$

In Eq. (1.62), $D_{\mathcal{G}_0,\sigma}(\tau_1, ..., \tau_k)(i,j)$ represents the weight function for QMC update. We further expand Eq. (1.62) into

$$g(\tau-\tau') =< Tc^{+}(\tau)c(\tau') > -\frac{1}{D_{\mathcal{G}_0,\sigma}(\tau_1, ..., \tau_k)(i,j)} D_{\mathcal{G}_0,\sigma}(\tau_1, ..., \tau_k)(i,j)^{T}, \tag{1.63}$$

where T represents the matrix transpose. Finally, the Green's functions are directly obtained in Matsubara frequency space by the Fourier transformation and Wick's theorem in Eq. (1.63). The Green's function is expressed as

$$g(i\omega_n) = g_0(i\omega_n) - g_0(i\omega_n)[\tfrac{1}{\beta}\sum_{i,j} M_{i,j} e^{i\omega_n(\tau_i-\tau_j)}]g_0(i\omega_n), \tag{1.64}$$

where $g_0(i\omega_n)$ is a bare Green function and $M_{i,j}$ is the inverse matrix of $D_{\mathcal{G}_0,\sigma}(\tau_1, ..., \tau_k)(i,j)$. Higher correlators can also be obtained from Wick's theorem.

Non-interacting Green's function The non-interacting Green's function is obtained by performing the infinite sum over Matsubara frequencies which is given by the Fourier transformation:

$$G(\tau) = \frac{1}{\beta}\sum_{-\infty}^{\infty} e^{-i\omega_n\tau} G(i\omega_n). \tag{1.65}$$

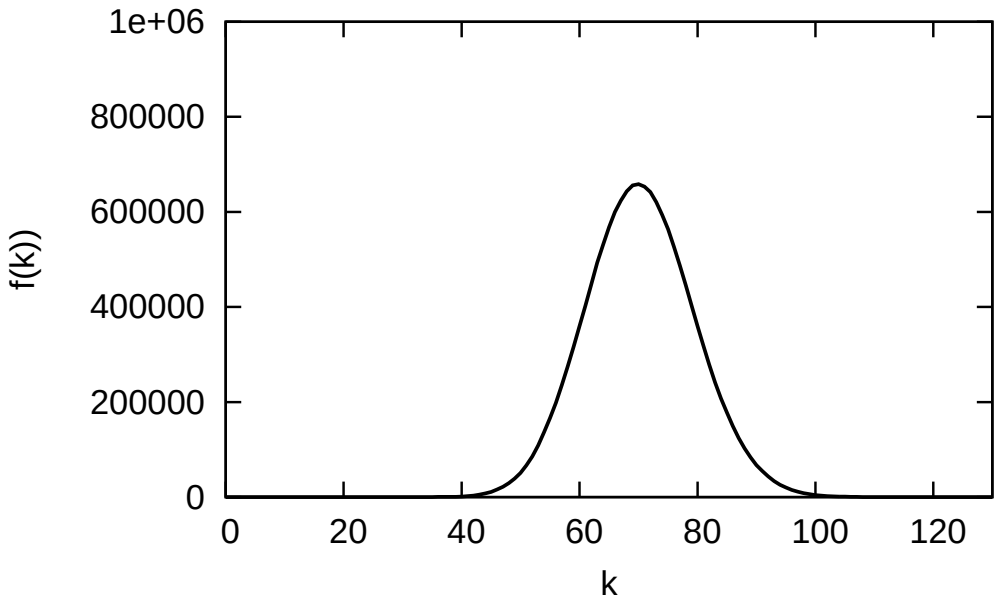

Figure 1.11: The distribution function as a function of k for $\beta = 5.0$, $U = 8.0$ and N_c=4. We use α=0.001 and the distribution function has Gaussian form.

Specifically, because the high order terms of the on-site Green's function, which is converged as $\frac{1}{(2n+1)}$, has large finite values, it is important to sum the high order terms exactly. The sum can be done analytically. The infinity sum becomes

$$\frac{1}{\beta}\sum_{-\infty}^{\infty} e^{-i\omega_n\tau}\frac{1}{i\omega_n} = -\frac{2}{\pi}\sum_{n=0}^{\infty}\frac{\sin(2n+1)\frac{\pi\tau}{\beta}}{2n+1} = -0.5. \tag{1.66}$$

The on-site Green's function $G(\tau)$ should be calculated by

$$G(\tau) = \frac{1}{\beta}(\sum_{n=-N}^{N} e^{-i\omega_n\tau}G(i\omega_n) + \sum_{n=-\infty}^{\infty} e^{-i\omega_n\tau}\frac{1}{i\omega_n} - \sum_{n=-N}^{N} e^{-i\omega_n\tau}\frac{1}{i\omega_n}). \tag{1.67}$$

The two-particle Green's function Since the vertex function $\gamma^{(4)}$ in the DF method is related to the two-particle Green's function, we need to calculate it. In the CT QMC method, the noninteracting action has Gaussian form which ensures the applicability of Wick's theorem to measure the two-particle Green's function which is given as

$$\begin{aligned}\chi_{\sigma\sigma'}(\nu_1,\nu_2,\nu_3,\nu_4) &= T[\overline{G_\sigma(\nu_1,\nu_2)G_{\sigma'}(\nu_3,\nu_4)} \\ &- \delta_{\sigma\sigma'}\overline{G_\sigma(\nu_1,\nu_4)G_\sigma(\nu_3,\nu_2)}].\end{aligned} \tag{1.68}$$

The overline indicates the Monte Carlo average. In each Monte Carlo measurement, $\overline{G(\nu,\nu')}$ depends on two different argument ν and ν' only in the average level, and $\overline{G(\nu,\nu')} = G(\nu)\delta_{\nu,\nu'}$ is a function of single frequency.

Global update It is difficult to tranfer the original phase into another phase in most statistical systems due to the deep valley in the free energy around the critical point. This problem is called the "trapping problem". In order to avoid this "trapping problem" in the free energy, we use the Wang-Landau updates or a new update process, which is called the global updates. We will discuss the Wang-Landau update later. In this part we would like to discuss the global update. In the global update, the Fermionic operators are permuted randomly spin indices of the current realization. I will give a very simple second-order perturbation example which is given as

$$< (n_\uparrow(\tau_1)+\alpha)(n_\downarrow(\tau_1)-1-\alpha)(n_\downarrow(\tau_2)-1-\alpha)(n_\uparrow(\tau_2)+\alpha) > . \tag{1.69}$$

To perform the global update the second-order term is exchanged with the first-order term:

$$< (n_\uparrow(\tau_1)+\alpha)(n_\downarrow(\tau_1)-1-\alpha)(n_\downarrow(\tau_2)-1-\alpha)(n_\uparrow(\tau_2)+\alpha) > \tag{1.70}$$
$$\rightarrow < (n_\downarrow(\tau_1)-1-\alpha)(n_\uparrow(\tau_1)+\alpha)(n_\uparrow(\tau_2)+\alpha)(n_\downarrow(\tau_2)-1-\alpha) > \tag{1.71}$$

All other quantities like imaginary time remain the same, because the interaction part is symmetrical with respect to permutations of spin. Because the global update does not change the weight value for QMC update, the movement is always accepted.

Implementation The random walk of CT QMC method is running in perturbation order k and imaginary time space. The standard Metropolis acceptance is given by

$$P_{k\rightarrow k+1} = \frac{U\beta}{k+1}\frac{D(\tau_1,...,\tau_k,\tau_{k+1})}{D(\tau_1,...,\tau_k)} \tag{1.72}$$

for the incremental step and

$$P_{k\rightarrow k-1} = \frac{k}{U\beta}\frac{D(\tau_1,...,\tau_k)}{D(\tau_1,...,\tau_{k-1})} \tag{1.73}$$

for the decremental steps. The most time consuming parts of this method is to calculate the determinant in Eq. (1.72) and Eq. (1.73) and the inverse matrix. Instead of taking k^3 operations, there is a fast-update formula which allows to calculate the determinant k^2 operation or less operation. We will discuss the detail formulas in the appendix part. Now I would like to present the simulation procedure for the CT QMC method based on Metropolis dynamics.

1. Calculate the non-interacting Green's function from Eq. (1.67).
2. Set up the initial condition : perturbation k=0 and matrix $M_{i,j}$=0.
3. Perform random walk in the perturbation order k line and imaginary time τ space.
4. Determine acceptance and rejection ratio for QMC steps. In this calculation the fast-update formula is used.
5. After sweeping, measure the Green's function given by Eq. (1.64).

At the half filling the average perturbation order $< k >$ is determined by

$$< k >= \beta U N_c[0.5- < n_\uparrow n_\downarrow > +\alpha(\alpha+1)]. \tag{1.74}$$

In the case of the square lattice at the half-filling, the best choice of α is α=-0.5. In this selection, the average perturbation order has the smallest one which is scaled by $< k > = 0.15 \times \beta U N_c$. On the other hand, in case of away half-filling we only take α=0.0001 (small value) to elevate the Fermionic sign problem and $< k >$ is scaled by $< k > = 0.5 \times \beta U N_c$.

The Wang-Landau update for CT QMC method Before introducing the quantum Wang-Landau method [22] for C-T QMC method, we would like to discuss the classical Wang-Landau method [20, 21] shortly. The classical Wang-Landau method [20, 21] was suggested by F. Wang and D. Landau in 2001. The idea is that the density of states $\rho(E)$ in the canonical distribution is directly calculated in a random walk in energy space. In this case the $\rho(E)$ does not depend on the temperature at all. Therefore, if we can calculate the $\rho(E)$ for all energies accurately, we can construct canonical distribution at any temperature. We will not discuss the formalism of the classical Wang-Landau method and only give the simulation steps.

1. Set up an initial modification factor f and $\rho(E)$=1.
2. Perform random walk in the energy space. The transition probability is given by P($E_1 \to E_2$)=min[$\frac{\rho(E_1)}{\rho(E_2)}$].
3. Each time an energy level E is visited, we modify the density of states by a modification factor f: $\rho(E) \to \rho(E)f$.
4. Count the histogram $H(E)$.
5. If the $H(E)$ is reasonablely flat, the $H(E)$ is reset to zero.
6. A modification factor f is decreased by $f \leftarrow \sqrt{f}$ and the precess starts Step. [2] again.

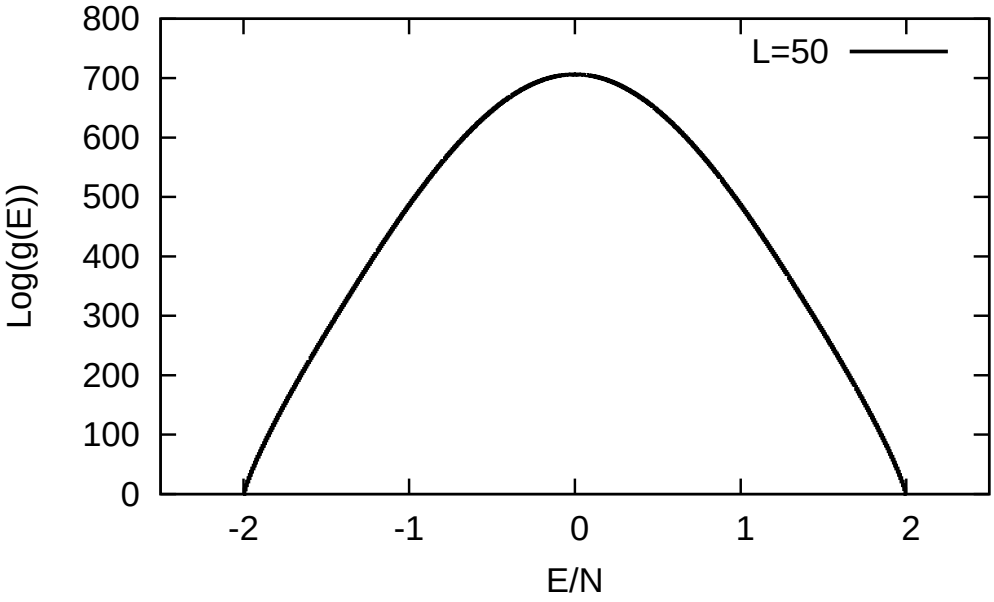

Figure 1.12: The density of states obtained by classical Wang-Landau method for 2D Ising model. The system size is L×L (L=50).

7. Repeat from Step. [2] to Step. [6] till obtaining $f \simeq 1.000000001$.

8. Determine the density of states $\rho(E)$.

As a test, we have reproduced the density of states $\rho(E)$ for 2D Ising model in Fig. (1.12) using the classical Wang-Landau method. The result coincides with the original result of Wang and Landau. When the density of states $\rho(E)$ is known, we can calculate the partition function given as

$$Z = \sum_E \rho(E) e^{-\beta E}. \tag{1.75}$$

The free energy can be calculated by $F(T) = -k_B T \ln(Z)$ and the internal energy, entropy, specific heat and other thermal properties are obtained by differentiating the free energy. The Wang-Landau method [22] was expanded as quantum systems by M. Troyer et al in 2003. In the quantum systems the partition function is given by

$$Z = Tr(e^{\beta H}) \tag{1.76}$$

which can not be cast in the form of Eq. (1.75), unless the complete set of eigenvalues of the Hamiltonian operator H is known. We use this partition function

$$Z = \Sigma_{k_1,...,k_n} g(k_1, ..., k_n) D_{\mathcal{G}_0,\sigma}(\tau_1, ..., \tau_k)(i, j), \tag{1.77}$$

where $D_{\mathcal{G}_0,\sigma}(\tau_1,...,\tau_k)(i,j)$ is the weight function. We need to decide the maximum perturbation order which is mainly given as

$$k_{max} = 2 \times U\beta N_c. \tag{1.78}$$

Like the classical Wang-Landau method, the histogram in each perturbation order is counted. Now I will give the crucial steps of the quantum Wang-Landau method for the CT QMC method. The steps are similar to those suggested by M. Troyer et al. [22].

1. Set up an initial $g(k)$ and the maximum perturbation order. Here we use $g(k) = e^{g_0(k)}$, where $g_0(k) = 0$ and $g(k) = 1$.

2. Set up an initial Wang-Landau factor f: ie) an initial factor $f = 0.01$.

3. Each time a configuration of k-th order is visited, $g_0(k)$ is plused by the Wang-Landau factor f ; i.e) $g_0(k) \longrightarrow g_0(k) + f$.

4. Count the histogram H(k).

5. If the $H(k)$ is reasonablely flat, the $H(k)$ is reset to zero. The Wang-Landau factor f is decreased by $f \leftarrow \sqrt{f}$ and the process starts from step. [2] again.

6. Repeat around four times from step. [2] to step. [5]and then we can get $g(k)$.

7. Perform the CT QMC calculation. The incremental and decremental weight functions are given as $W = \frac{g(k+1)}{g(k)} \frac{\beta U}{k+1} \frac{D^{k+1}}{D^k}$ and $W = \frac{g(k-1)}{g(k)} \frac{k}{\beta U} \frac{D^k}{D^{k-1}}$, respectively.

Hybridization-coupling CT QMC method A new impurity solver was developed by P. Werner et al. [14]. Unlike the weak-coupling CT QMC method which is expanded over interaction U, this CT QMC method is expanded over hybridization terms so it is called hybridization-coupling CT QMC method [14]. For the hybridization expansion like the weak-coupling CT QMC method, the action is decomposed into hybridization part and the local part:

$$S_{hybri} = -\int d\tau d\tau' \sum_{\sigma} c_\sigma(\tau) F_\sigma(\tau - \tau') c^\dagger_\sigma(\tau') \tag{1.79}$$

$$S_{local} = -\mu \int d\tau (n_\uparrow + n_\downarrow) + U \int d\tau n_\uparrow n_\downarrow. \tag{1.80}$$

The partition function Z is given as $Z = TrT_\tau e^{-(S_{hybri}+S_{local})}$. When the partition function Z is expanded in powers of F_σ, the partition function is expressed as

$$\begin{aligned} Z &= TrT_\tau e^{-S_L} \prod_\sigma \sum_{k_\sigma} \frac{1}{k_\sigma!} \int_0^\beta d\tau_1^\sigma ... d\tau_k^\sigma \int_0^\beta d\tilde{\tau}_1^\sigma ... d\tilde{\tau}_k^\sigma \\ &\times \Big[c_\sigma(\tau_1) F_\sigma(\tau_1 - \tilde{\tau}_1) c_\sigma^\dagger(\tilde{\tau}_1) \dots \\ &\quad \dots c_\sigma(\tau_{k_\sigma}) F_\sigma(\tau_{k_\sigma} - \tilde{\tau}_{k_\sigma}) c_\sigma^\dagger(\tilde{\tau}_{k_\sigma}) \Big], \end{aligned} \tag{1.81}$$

with $D_{F,\sigma}(\tau_1, \dots, \tau_{k_\sigma}; \tilde{\tau}_1, \dots, \tilde{\tau}_{k_\sigma})(i,j) = F_\sigma(\tau_i - \tilde{\tau}_j)$ which can be calculated by the fast-update formula. Finally, the partition function is

$$Z = TrT_\tau e^{-S_L} \prod_\sigma \sum_{k_\sigma} \int d\tau_1^\sigma ... d\tau_k^\sigma d\tilde{\tau_1^\sigma} ... d\tilde{\tau_k^\sigma} D_{F,\sigma} \times c_\sigma(\tau_k) c_\sigma^\dagger(\tilde{\tau_k}) ... c_\sigma(\tau_1) c_\sigma^\dagger(\tilde{\tau_1}). \tag{1.82}$$

The Green's function is calculated by

$$G(i\omega_n) = -\frac{1}{\beta} \sum_{i_e, i_s} e^{i\omega_n(i_e - i_s)} M_{i_s, i_e} \tag{1.83}$$

where M_{i_s,i_e} is the inversion of $D_{F,\sigma}(\tau_1, \dots, \tau_{k_\sigma}; \tilde{\tau}_1, \dots, \tilde{\tau}_{k_\sigma})(i,j)$. Now I would like to compare the matrix size, which is related to the computational time, in the HFQMC, weak-coupling CT-QMC and hybridization-coupling CT QMC methods. The result is shown in Fig. (1.13). The α is used as 0.01 for the weak-coupling CT QMC method and the matrix size of HFQMC is scaled as $< k > = \beta U$. The hybridization-coupling CT QMC method has much smaller matrix size than other QMC methods. Moreover, as the interaction U is increased, the matrix size is decreasing. However, in spite of nice advantages, much more QMC sweeps are needed in order to obtain exact results because the high frequency part has large noise, unlike the weak-coupling CT QMC method. In the cluster-DMFT methods, computational effort is increasing exponentially with the cluster size because of calculation part of the second term in Eq. (1.82).

1.3.2 Semiclassical approximation method

At high temperature the Monte Carlo integration over the auxiliary classical field $\phi(\tau)$ can be approximated by assuming $\phi(\tau) \approx$ const. This approximation is useful to check the QMC results at high temperature with strong coupling quickly. Moreover, the spectral function can be calculated directly in real frequency space without analytical continuation. In this part I will introduce the SCA method as an impurity solver. The partition function is defined as

$$Z = \int \mathcal{D}[c_i^\dagger c_i] e^{-S_{eff}}, \tag{1.84}$$

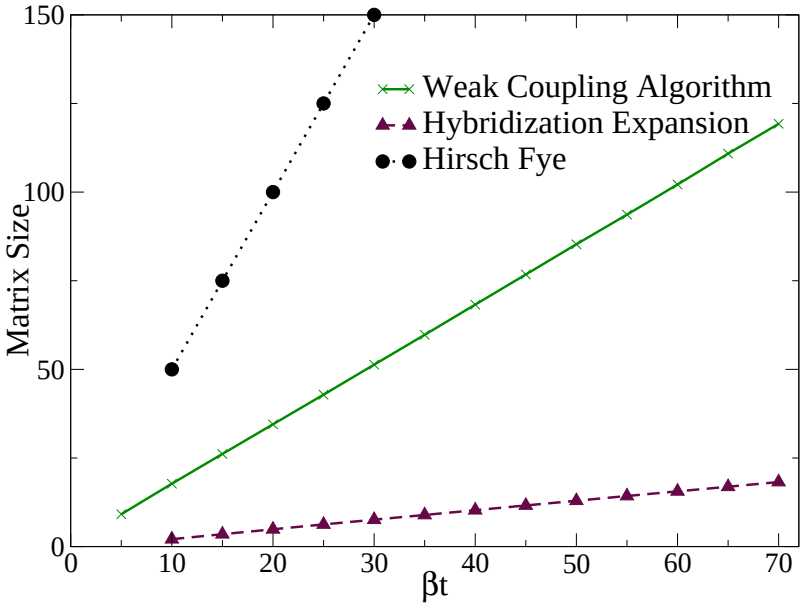

Figure 1.13: Scaling of the matrix size with inverse temperature for U/t=4. [Phys. Rev. B 75, 085108 (2007) [57]]

where

$$\begin{aligned} S_{eff} = &\int_0^\beta d\tau \int_0^\beta d\tau' d\tau \; c^\dagger(\tau)\mathbf{a}_\sigma(\tau,\tau')c(\tau') \\ &+ \int_0^\beta d\tau \sum_{i=0}^{N_c-1} U n_{i,\uparrow}(\tau)n_{i,\downarrow}(\tau), \end{aligned} \tag{1.85}$$

Here $\mathbf{a}_\sigma(\tau,\tau')$ is the Weiss field, β=1/T is the inverse temperature, N_c is the number of site, c and $c^\dagger$ are site-dependent spinor fields and $n = c^\dagger c$ is the particle number operator. We decouple the interaction term as

$$U n_{i\uparrow}(\tau)n_{i\downarrow}(\tau) = \frac{U}{4}\left[N_i^2(\tau) - M_j^2(\tau)\right], \tag{1.86}$$

with $n_\uparrow n_\downarrow = \frac{1}{4}\left((n_\uparrow + n_\downarrow)^2 - (n_\uparrow - n_\downarrow)^2\right) = \frac{1}{4}(N^2 - M^2)$. N is the particle number and M is the magnetization. Now the action is given by

$$S_{eff} = \int_0^\beta d\tau \int_0^\beta d\tau' d\tau \; c^\dagger(\tau)\mathbf{a}_\sigma(\tau,\tau')c(\tau') + \frac{U}{4}\int_0^\beta d\tau \sum_{i=0}^{N_c-1}(N_i^2(\tau) - M_i^2(\tau)). \tag{1.87}$$

We only consider the case of a half-filling, therefore the particle number is constant ($N_i(\tau)$=1). Using a continuous Hubbard-Stratonovich (HS) transformation which is

given by

$$\int dx e^{-\pi x^2 + 2\sqrt{\pi} A x} = e^{A^2}, \tag{1.88}$$

we can obtain a new partition function

$$Z = \int D[c^\dagger c] D[\phi] e^{\int d\tau \int d\tau' c^\dagger(\tau) a(\tau,\tau') c(\tau') - \int d\tau (\frac{1}{4U}\phi^2(\tau) - \frac{1}{2}\phi(\tau) M(\tau))}. \tag{1.89}$$

Here we assume that $\phi(\tau)$ is τ-independent. With this approximation and after a Grassmann integration, we can rewrite the partition function which is represented as the fermionic Matsubara frequency:

$$Z = \int d\vec{\phi_j} e^{-S_{eff}[\mathbf{a}(i\omega_n), \phi_j]}, \tag{1.90}$$

where the effective action $S_{eff} = \beta V$ is defined by

$$V(\vec{\phi_j}) = \frac{\sum_j \phi_j^2}{U} - T \sum_{\omega_n, \sigma} \ln \det[-\beta \mathbf{a}(i\omega_n) + \hat{1}\phi_j \sigma_z]. \tag{1.91}$$

Here j is site index and σ_z is the z-component Pauli matrix. The impurity Green's function is calculated by

$$G_j = \frac{1}{N_c} \frac{\delta \ln Z}{\delta a_j}. \tag{1.92}$$

In the SCA method we can calculate the spectral function directly in the real frequency space. For example, in the single-site case the impurity Greens function is given by

$$G(i\omega_n) = \frac{1}{Z} \int d\phi e^{-\beta V(\phi)} (\mathbf{a}(i\omega_n) + \phi\sigma_z)^{-1}. \tag{1.93}$$

The spectral function is obtained by replacing $\mathbf{a}(i\omega_n)$ to $\mathbf{a}(\omega)$ and performing the integration in Eq. (1.93).

1.4 Conclusion

In this section we present the DMFT, cluster-extension of DMFT, DF, CT QMC and SCA methods. To summarize we would like to discuss the advantages and limitation of each method.

DMFT method : Even if nonlocal correlations are fully suppressed in the DMFT method, it can describe the basic nature of the metal-insulator transition and heavy fermion compounds. Recently, the DMFT method was combined with a first-principle calculation which is called the local density approximation (LDA) + DMFT method.

It is really big step forward to treat the electronic correlations in the first-principle calculation. In DMFT + QMC, the QMC methods do not exhibit the Fermionic sign problem even in the case of away-half filling. Moreover, the newly developed CT QMC methods can access by very low temperature regions ($T < 0.001$). On the other hand, it cannot describe the Ruderman-Kittel-Kasuya-Yosida (RKKY) interaction and d-wave superconductor because the nonlocal correlations are neglected.

Cluster extension of DMFT and DF methods : There are two kinds of methods which can overcome limitation of the DMFT method. The first idea is to apply a cluster extension of the DMFT methods which is called the DCA and CDMFT methods. These methods reduce the complexity of the lattice problem by mapping it to a finite-size cluster self-consistently embedded in a mean field level. The main difference of these methods is boundary condition which is given by the Laue condition. These methods can capture the nonlocal correlations in the cluster size exactly and have smaller computational load and Fermionic sign problem than a lattice calculation. On the other hand, these methods are still expensive in terms of computational time and long range correlations are considered on the mean field level only.

Recently, another approach was invented. Unlike the cluster extension of DMFT method, it makes new auxiliary fields and vertex function by a dual transformation and perturbation expansion. Since this vertex function, which is related to two-particle Green's function, is nonlocal in imaginary time, nonlocal correlations can be described. This method has no Fermionic sign problem at any case and small computational load because of the single-site problem. Through Bethe-Salpeter equation it can also capture the two-particle properties easily. The limitation of this method is still calculated nonlocal correlations within perturbative approach.

weak-coupling and hybridization-coupling CT-QMC methods : New methods, which are based on a diagram expansion, were developed as impurity solver. Compared with the HFQMC method, they allow a calculation at lower temperature region without the Trotter decomposition error. They are distinguished by expansion terms. The weak-coupling CT QMC method is expanded over interaction U. Since the matrix size has form of $< k >= 0.5 N_c U \beta$, this method is suitable for the large cluster calculation and weak-coupling regions. Another method, which is called hybridization-coupling CT QMC method, expands over the hybridization part. As the interaction is increased, the matrix size is decreased unlike the weak-coupling CT QMC method, so it has nice computational advantages in the strong-coupling regions. However, when the cluster size is increased, the computational time is increasing exponentially and noise in the high-frequency parts is quite serious problem.

SCA method : The SCA method, which is based on continuous HS transformation, is strong-coupling approximation under condition of $\phi(\tau)$=constant. Due to this condition, this method can obtain reliable results at high temperature and strong-coupling regions. The powerful advantage of this method is that it can calculate the density of states directly in the real frequency space. So it is useful to check the QMC result with analytical continuation at high temperature in the strong-coupling region.

Chapter 2

Hubbard model in the DMFT and cluster-DMFT methods

2.1 Introduction

The Hubbard model is the simplest model which can describe the strongly correlated electron systems such as high-temperature superconductor, antiferromagnetism and heavy fermion compounds. However, this model is not be solved exactly except some special cases in spite of a lot of efforts. Recently, substantial progress has been made by the DMFT and cluster-DMFT methods. In this section we employ them to study the Hubbard model on the Bethe lattice and square lattice.

Even if the nonlocal terms are absent in the single-site DMFT method, the powerful advantage of this method is that we can explore very low temperature regions with small computational effort without the infamous Fermionic sign problem using the CT QMC method as impurity solver. Usually, the CT QMC method can easily access by βt=500 in the single-site problem. First we will discuss the physics in the two-plane Hubbard model on the Bethe lattice using the DMFT method. The YBCO superconductor was discovered in 1986 [3]. Through the photoemission experiments in YBCO [23, 24], one found that there is a difference between bonding and antibonding CuO-plane bands as a result of the hopping between the CuO-planes in the YBCO compound. This experimental situation in the YBCO compound is related to the two-plane Hubbard model which is shown in Fig. (2.1). Moreover, we can understand the nature of Mott-band insulator and metal-band insulator transition at very low temperature through exploring this model.

At the next part we would like to discuss the Hubbard model on the square lattice. Theoretically, the nature of the Fermi-liquid theory, metal-insulator transition and antiferromagnetism by the size of cluster is shown in this model. We explore the case of small cluster (N_c=4) using both the CDMFT and DCA methods. We obtain the CDFMT result from Phys. Rev. Lett. 101, 186430[28]. Since the long range

correlations are fully suppressed, the metal-insulator transition and Fermi liquid theory should be exhibited due to the weak frustration effect. We compare the results obtained from the DCA with those obtained from the DMFT and CDMFT methods and see the difference of results. Finally, we discuss the Slater-Mott mechanism, total internal energy and Fermi-liquid theory on the square lattice with N_c=4.

2.2 Two-plane Hubbard model on the Bethe lattice

The nature of transition between band-insulator and Mott insulator is still unclear and interesting. While the strong Coulomb interaction induces the gap which is called Mott insulator, the band insulator is caused by either a filled or an empty band. Theoretically, the two-plane Hubbard model is the simplest model which can explore this system. Recently, this model was studied through DMFT (HFQMC, iteration pertubative theory) [26, 59], CDMFT (exact diagonalization) [25] and HFQMC [27] methods. However, due to limitation of HFQMC and exact diagonalization methods as impurity solver, it is difficult to explore very low temperature regions or to obtain reliable results. In this part, we study the physics in low temperature regime using the DMFT method combined with the CT QMC method.

2.2.1 Model and formalism of the DMFT method

As the simplest model, we consider the two-plane Hubbard model on the Bethe lattice like Fig. (2.1). The Bethe lattice is a connected cycle-free graph, where each node is connected to coordination number neighbors and has a semicircular density of states:

$$D(\epsilon) = \frac{1}{2\pi t^2}\sqrt{4t^2 - \epsilon^2}. \tag{2.1}$$

The electrons move between each lattice as well as each plane by hopping. The Hamiltonian is defined as

$$H = -t \sum_{\langle i,j\rangle\sigma,\alpha} c^\dagger_{i\sigma\alpha} c_{j\sigma\alpha} - t_{AB} \sum_{i,\sigma\alpha} c^\dagger_{i\sigma\alpha} c_{i\sigma\alpha} + U \sum_{i,\alpha} n_{i\uparrow\alpha} n_{i\downarrow\alpha}, \tag{2.2}$$

where $c_{i\sigma}(c^\dagger_{i\sigma})$ is the annihilation (creation) operator of an electron with spin σ at the i-th site, α (AB) is a site of plane, $t(t_{AB})$ is the hopping matrix element and U represents the Coulomb repulsion. We set t=0.5 and the bandwidth is 1.0. We employ the DMFT method which is combined with the CT QMC method. On the Bethe lattice the DMFT self-consistent equation is easily given as

$$G_0^{-1}(i\omega_n) = \begin{pmatrix} i\omega_n & -t_{AB} \\ -t_{AB} & i\omega_n \end{pmatrix} - t^2 G(i\omega_n), \tag{2.3}$$

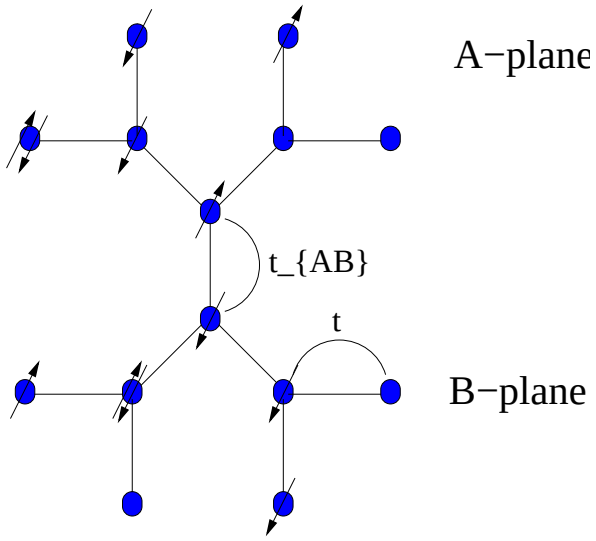

Figure 2.1: Graphical two-plane model on the Bethe lattice. The electrons hop between neighboring sites or between corresponding site of both lattices.

where ω_n is the Matsubara frequency. The bare Green's function $G_0(i\omega_n)$ is used as an input values to the impurity solver and the converged Green's function is obtained after several iterations.

2.2.2 From Band insulator to Mott insulator

In former HFQMC study of our group [26], the metal, band-insulator and Mott-insulator are presented at βt=40. Below around $U = 2t_{AB}$, a first-order metal-insulator transition (coexitence region) is shown. As t_{AB} is increased, a first-order transition is changed into a continuous transition. In this study a clear boundary between band-insulator and Mott-insulator was not found. Now we would like to explore a nature of transition in the low temperature regions (βt = 100) with advantages of the CT QMC method. At first we measure the double occupancy to check the difference between transition of the metal and Mott-insulator and transition of the metal and band-insulator. The double occupancy results are presented in Fig. (2.2) for several t_{AB}. The double occupancy as a function of U at t_{AB}=0.5 has a dropping around critical interaction U_c=1.6 and shows the hysteresis which is associated with a first-order transition. A clear boundary between metal and insulator is also seen. At t_{AB}=0.8 the double occupancy is decreased smoothly and a first-order transition is changed into a continuous transition. We guess that the difference of both behaviors is caused by the type of transition. In order to see the difference between both transitions clearly, we measure the quasiparticle weight Z.

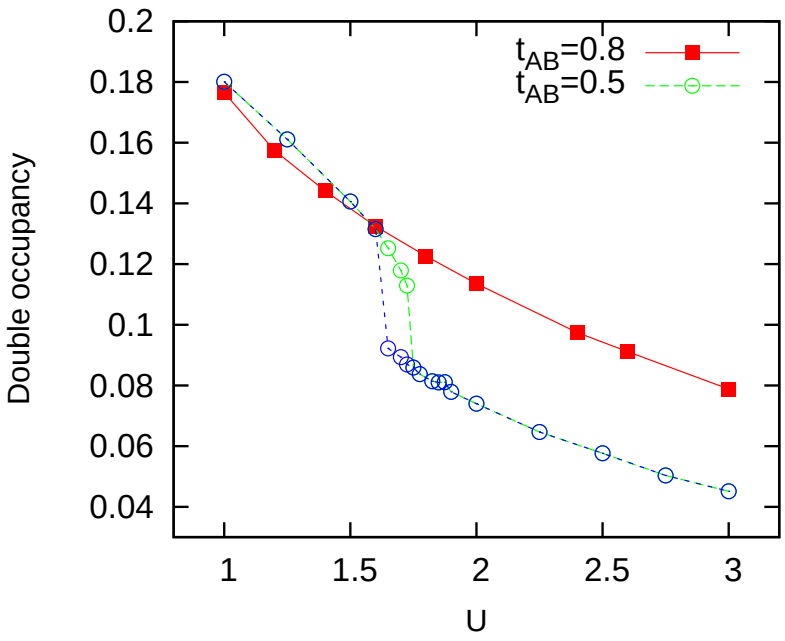

Figure 2.2: The double occupancy as a function of U for several t_{AB}.

The quasiparticle weight Z is approximately calculated by

$$Z \approx \frac{1}{1 - \frac{Im(\Sigma(\omega_0))}{\omega_0}}, \tag{2.4}$$

where w_0 is the lowest imaginary Matsubara frequency value and the symmetry self-energy is

$$\Sigma(\omega_0) = \Sigma_0(\omega_0) + \Sigma_1(\omega_0). \tag{2.5}$$

While the quasiparticle weight Z should be zero in the Mott insulator at zero temperature due to the enhancement of effective mass, it remains as finite values in the metallic state and band insulator. The quasiparticle weight Z as a function of U is exhibited in Fig. (2.3). As the interaction U is increased, the quasiparticle weight Z is decreasing in both cases of t_{AB}=0.5 and 0.8. In the regions (t_{AB}=0.5) in which a first-order transition is represented, there is a kink of quasiparticle Z in the critical interaction U_c=1.6. At t_{AB}=0.8 this kink is disappeared due to a continuous transition. Now we clarify the transition of the metal-band insulator and of metal-Mott insulator. Next we would like to find the boundary of Mott-band transition and compare QMC results with those in the atomic limit in the strong-coupling regions. If there is a boundary between them, an anomalous behaviors such as a kink and jump in double occupancy should be observed. We show the double occupancy as a function of t_{AB} for U=3 in Fig. (2.2.2). The double occupancy in QMC and atomic

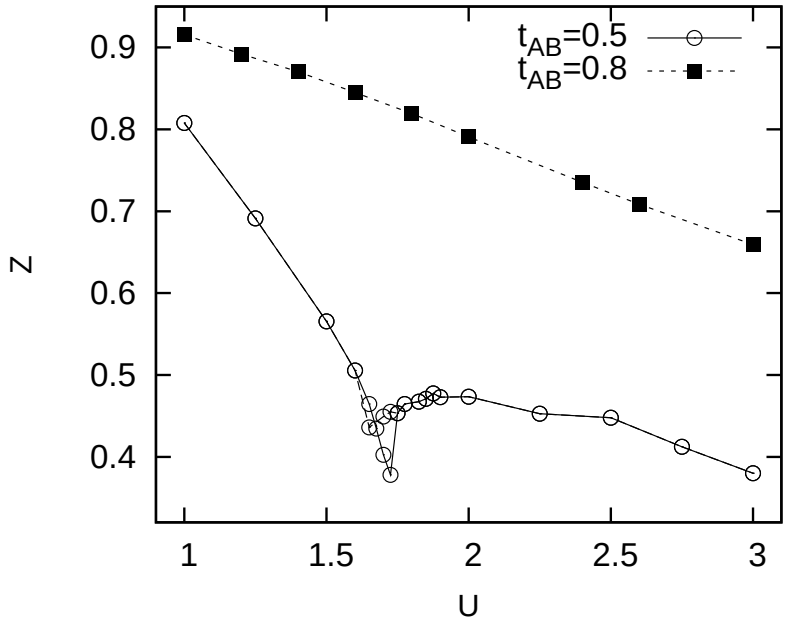

Figure 2.3: The quasiparticle weight Z as a function of U for several t_{AB}.

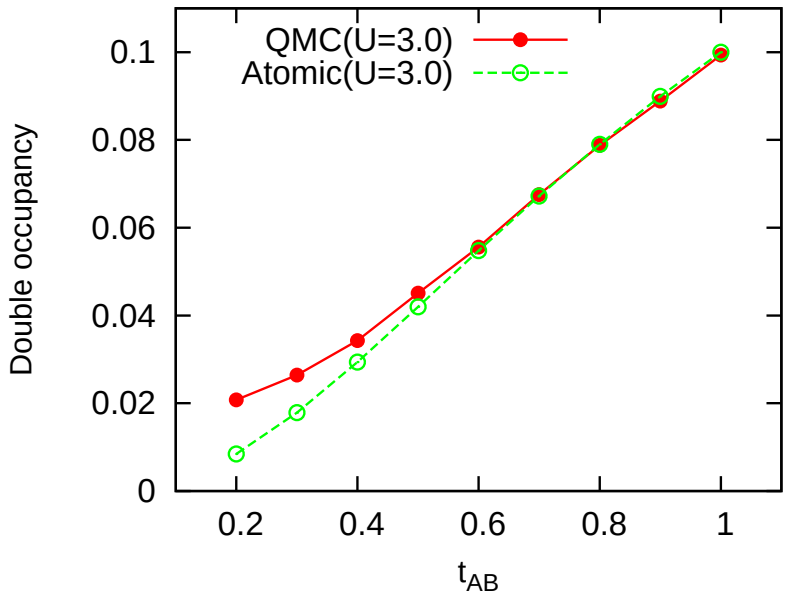

Figure 2.4: The double occupancy as a function of t_{AB} for U=3.

limit are smoothly increasing, as t_{AB} is increased. Unlike expectation, we do not find a clear boundary between Mott-insulator and band-insulator and in the atomic limitation the behavior of the double occupancy is similar. At βt=250 the behavior is similar to that for βt=100.

2.3 Mott transition in the cluster-DMFT methods

In this part we would like to determine the difference of between the CDMFT [10] and DCA [8, 9] methods with N_c=4 on the square lattice. We will employ the real space representation for comparison of both methods in the same condition and compare the critical interaction U_c obtained from both methods. We will also explore the physical quantities such as the double occupancy for the Slater-Mott mechanism and total internal energy for the Fermi-liquid behavior on the square lattice.

2.3.1 Formalism of CMDFT and DCA methods

In the CDMFT method [10] a four-site superlattice, which periodically tiles in the lattice, is selected as the left figure of Fig. (2.5). The hopping matrix of the superlattice is written by

$$t^{CDMFT}(\tilde{\mathbf{k}}) = \begin{pmatrix} 0 & t(1+e^{-2ik_x}) & t(1+e^{-2ik_y}) & 0 \\ t(1+e^{2ik_x}) & 0 & 0 & t(1+e^{2ik_y}) \\ t(1+e^{2ik_y}) & 0 & 0 & t(1+e^{2ik_x}) \\ 0 & t(1+e^{-2ik_y}) & t(1+e^{-2ik_x}) & 0 \end{pmatrix},$$

in the real space and breaks the lattice translational symmetry, because the intersite correlations within a superlattice are different from those between superlattice. The Green's functions are freely summed over the wave vectors $\tilde{\mathbf{k}}$ of the superlattice due to omission of the phase factors and are determined by self-consistent equation which is written by

$$\begin{aligned} G_0^{-1}(i\omega_n) &= \left(\int d\tilde{\mathbf{k}} \frac{1}{i\omega_n + t^{CDMFT}(\tilde{\mathbf{k}}) - \Sigma(i\omega_n)} \right)^{-1} \\ &+ \Sigma(i\omega_n). \end{aligned} \tag{2.6}$$

Unlike the CDMFT method, the hopping matrix $t(\tilde{\mathbf{k}})$ of the superlattice in the DCA method is given within periodic boundary condition and the lattice translation symmetry is kept. The hopping matrix in the real space is

$$t^{DCA}(\tilde{\mathbf{k}}) = \begin{pmatrix} 0 & -2t\cos(k_x) & -2t\cos(k_y) & 0 \\ -2t\cos(k_x) & 0 & 0 & -2t\cos(k_y) \\ -2t\cos(k_y) & 0 & 0 & -2t\cos(k_x) \\ 0 & -2t\cos(k_y) & -2t\cos(k_x) & 0 \end{pmatrix},$$

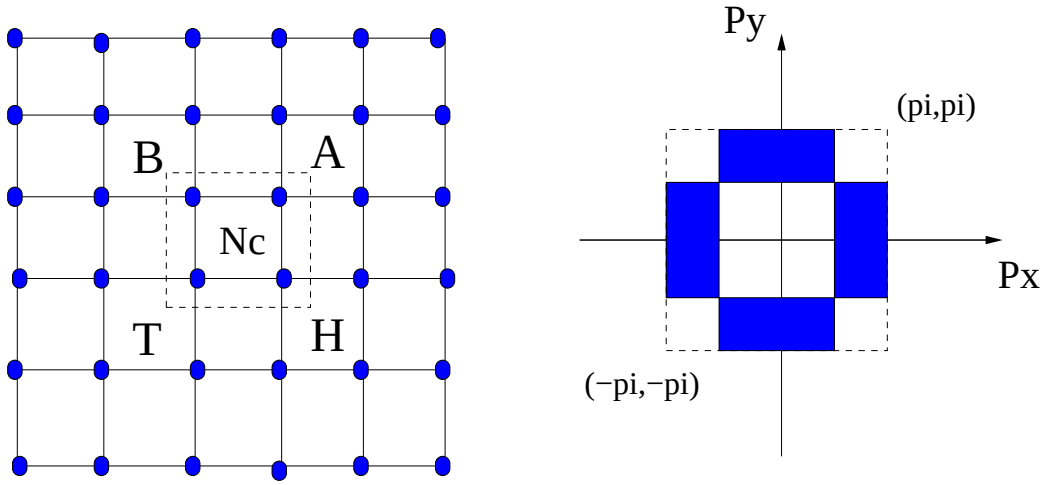

Figure 2.5: (Left figure): The entire infinite lattice is tiled with identical clusters of size N_c in the real space (Description for the CDMFT method) (Right figure): The reduced Brillouin zone, which is divided as the number of cluster. (Description for the DCA method)

where $-2t\cos(k_x)$ is from $t(e^(ik_x) + e^(- ik_x)$. By summing over wave vectors like the CDMFT method, one can directly integrate by replacing $t^{CMDFT}(\tilde{\mathbf{k}})$ for $t^{DCA}(\tilde{\mathbf{k}})$ in Eq. (2.6). The main difference of both methods lies in the boundary condition of the cluster given by the Laue function in chapter 1. Even if the DCA method can be written in the real space, it is also constructed by diagonalizing the Green's function in the momentum space easily. In this case the DCA equation is given as

$$\overline{G}_\sigma(\mathbf{K}, i\omega_n) = \frac{1}{N}\sum_{\tilde{\mathbf{k}}} \frac{1}{i\omega_n - \epsilon_{\mathbf{K}+\tilde{\mathbf{k}}} - \Sigma_\sigma(\mathbf{K}, i\omega_n)}, \tag{2.7}$$

where N is the number of lattice sites in each first Brillouin zone, $\mathbf{K}$ is the cluster momenta, the summation over $\tilde{\mathbf{k}}$ is calculated in each of them and $\epsilon_{\mathbf{K}+\tilde{\mathbf{k}}}$ is the bare dispersion relation which is given by

$$\epsilon_{\mathbf{K}+\tilde{\mathbf{k}}} = -2t(\cos(\mathbf{K_x} + \tilde{\mathbf{k}_x}) + \cos(\mathbf{K_y} + \tilde{\mathbf{k}_y})). \tag{2.8}$$

Here the cluster momenta are $\mathbf{K} = (0,0)$, $\mathbf{K} = (\pi,0)$, $\mathbf{K} = (0,\pi)$ and $\mathbf{K} = (\pi,\pi)$. The lattice self-energy is constant in each first Brillouin zone, which is created by partitioning the original Brillouin zone. The detail reduced Brillouin zone and cluster momenta are exhibited in Fig. (2.5). Like the standard procedure of the DMFT method, the converged Green's function in both the CDMFT and DCA methods is determined self-consistently after several iterations.

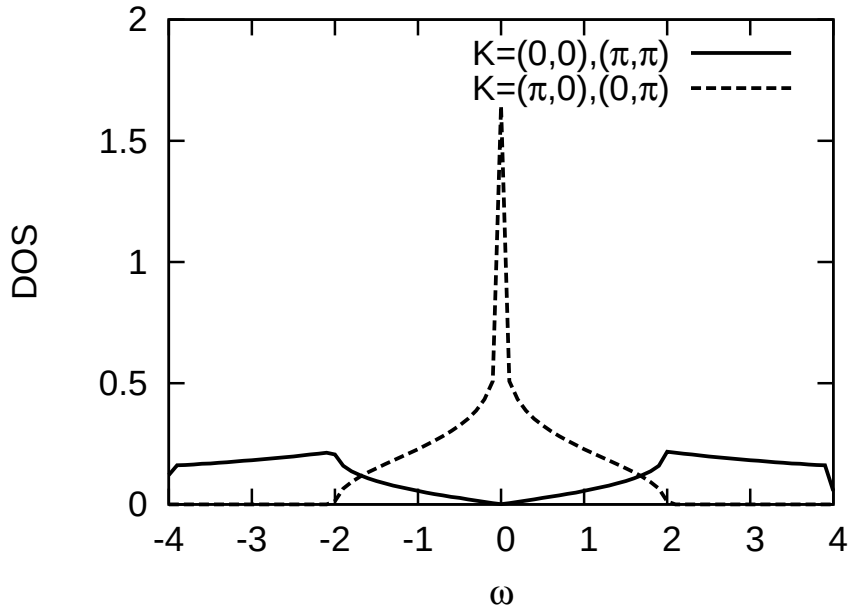

Figure 2.6: Non-interacting density of states for the each cluster momenta on the square lattice within DCA method.

2.3.2 Non-interacting density of states

In this part we obtain the density of states on the square lattice in the different orbitals (cluster momenta) within DCA method with N_c=4 by setting U=0. The density of states in each cluster momenta is calculated by Eq. (2.7) and for the exact integration we employed the tetrahedra method [55] [See appendix]. The density of states of each cluster momenta are plotted in the right figure of Fig. (2.6). In the Fermi surface ($\mathbf{K} = (0, \pi)$ and $\mathbf{K} = (\pi, 0)$), the Van Hove singluarity is shown around Fermi energy $\omega = 0$ and the band gap between $K = (0, 0)$ and $K = (\pi, \pi)$ is presented due to shifting of energy. There are an overlap between each cluster momenta.

Metal-insulator transition in CDMFT and DCA methods

We would like to compare the critical interaction U_c obtained from the single-site DMFT, CDMFT and DCA methods with N_c=4. The phase diagram of single-site DMFT and CMDFT methods with N_c=4, which is obtained from Phys. Rev. Lett. 101, 186403 (2008) [28], is presented in Fig. (2.8). We also present the double occupancy as a function of U for β=20 in Fig. (2.7) using the DCA method with N_c=4. The double occupancy is decrased rapidly around U/t=4.5 which is indicated as the critical interaction U_c. Now we will analyze the critical U_c of the DMFT, CDMFT

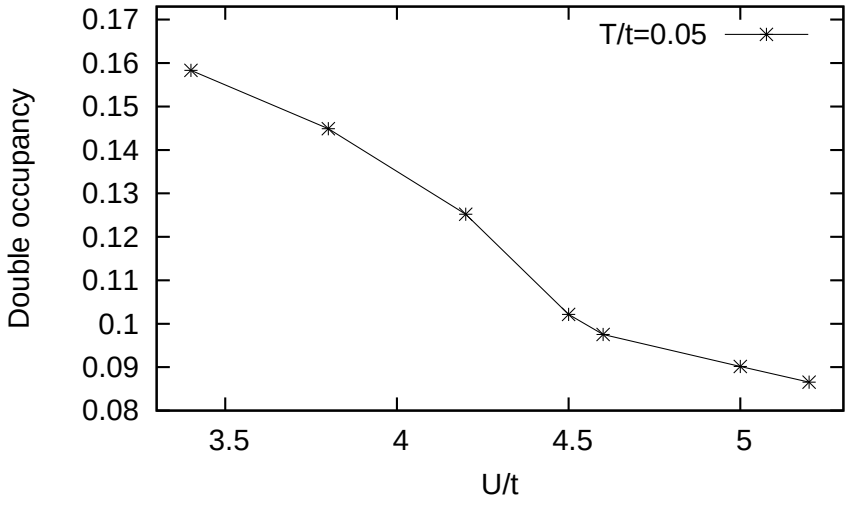

Figure 2.7: The double occupancy as a function of U/t for T=0.05. The Mott-insulator is presented around U/t=4.5.

and DCA methods. The critical interaction for β=20 is U_c=9.4 in the single-site DMFT method. Since the single impurity is controlled by a paramagnetic external bath and nonlocal correlations are disappeared, the system is highly frustrated and the large critical interaction is presented. The critical interaction for β=20 in the CDMFT method is U_c=5.8 approximately in Fig. (2.8) and this result is bigger than that obtained from the DCA method. Due to the restriction to small clusters with N_c=4, the long range correlations are fully suppressed and the boundary condition, which is given by each method, can be important. This means that the model with an intermediate degree of frustration by dominant short range correlations have the character of the metal-insulator transition, unlike the case of square lattice with long range correlations [42]. Even if the critical interaction has different value due to the boundary condition, both DCA and CDMFT methods can describe the metal-insulator transition clearly and the critical interaction U_c of both methods should be converged as the value of U_c=0 in the large clusters at zero temperature. We continue with the analysis about the nature of phase transition which is presented in Phys. Rev. Lett. 101, 186403 (2008) [28]. According to the analysis of the, the existence of the anomalous metallic state was predicted at very low temperature ($\beta t = 100$) and two orbitals [(π ,0) and (0, π)] were exhibited as a Mott transition, while the remaining orbitals [(0,0) and (π ,π)] were undergone as a band transition. This requires the Slater or Mott transition in each different momentum space. Moreover, at N_c=4 the singlet plaquette ground state is dominant in Fig. (2.8 (a) inset) [28]. We will discuss our analysis of Slater-Mott mechanism later. We also observed the

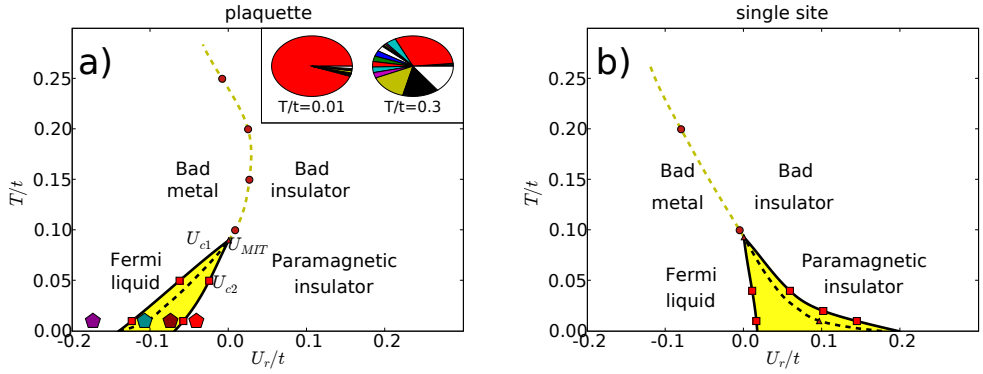

Figure 2.8: (a) The phase diagram of the half-filled Hubbard model with N_c=4. Inset: The histogram of the two insulating states. It shows the probability for a given cluster eigenstate among 16 eigenstates of the half filled plaquette. The singlet plaquette ground state has the highest probability (b) For comparison, the corresponding phase diagram of the single-site DMFT is shown. The coexistence region is shown as the shaded region. For easier comparison, the x axis is rescaled and the reduced value of $U_r = \frac{U-U_{MIT}}{U_{MIT}}$ is used. The critical value of U is $U_{MIT} = 6.05t$ in the cluster case and $U_{MIT} = 9.35t$ in the single-site case. [Phys. Rev. Lett. 101 186403 (2008) [28]]

similar interval between the critical interaction U_c on the triangular lattice in both CDMFT and DCA methods. To find the reason, why there is a difference between both methods clearly, might be a future subject.

2.3.3 Slater-Mott mechanism

It is well known that the antiferromagnetic long range correlations or local orders are induced the energy gap on the square lattice in the weak-coupling regions according to some references [56, 58]. This theory is called the Slater mechanism. However, it is still unclear whether the Slater gap is opened in the intermediate or strong-coupling regions. In order to check that we calculated the double occupancy as a function of temperature. It is valuable to study this mechanism because many materials, such as high temperature superconductors and heavy fermion compounds, seem to be in the intermediate coupling regime in which theoretical understanding is incomplete. As temperature is decreased in the right figure of Fig. (2.9) for U/t=4.6, the double occupancy is also decreased. The transition is caused by a rapid decrease in the double occupancy. This indicates that if the Slater physics is dominant, the opening of a gap can decrease the interaction energy. In the left figure of Fig. (2.9), the double occupancy is constant or increased due to the enhancement of local fluctuations, as

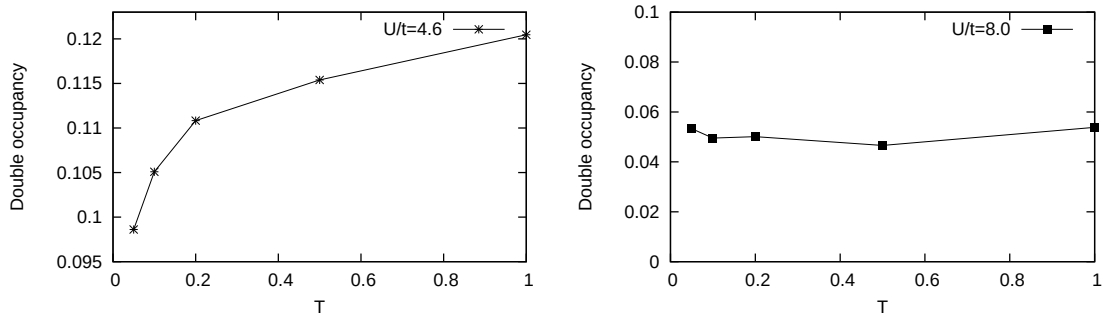

Figure 2.9: Temperature dependence of the double occupancy for $U/t = 4.6$ (Left panel) and $U/t = 8.0$ (Right panel).

temperature is decreased. This situation is called as the Mott physics. Our results and analysis about the Slater-Mott mechanism is very close to the recent works [56].

2.3.4 Energy and specific heat in the metallic state

In this part we will measure the total internal energy very precisely in the metallic state using the DCA method with N_c=4. Even if the hybridization CT QMC method can perform the calculation in the very low temperature regions without computational problem, it produces data with much large noise in the high frequency part of the self-energy due to the statistical error. Unlike the hybridization CT QMC method, the weak-coupling CT QMC method does not have this noise in the high frequency part due to the equation given by

$$G(i\omega_n) = G_0(i\omega_n) - G_0(i\omega_n)\frac{1}{\beta}\sum_{i,j} M_{i,j}e^{i\omega(\tau_i-\tau_j)}G_0(i\omega_n). \tag{2.9}$$

This equation makes the system to be stable in the low frequency as well as in the high frequency. The self-energy, which is obtained using both methods in single-site DMFT, is shown in Fig. (2.10) [57]. Due to this reason, the weak-coupling CT QMC method is suitable to calculate the total internal energy accurately without serious computational error. We performed around 10^7 QMC sweeps and consider the Matusbara frequencies in $w < 50.0$ for high frequency part in order to obtain numerically exact results. The total internal energy can be calculated in this formalism in terms of the Green's function and double occupation:

$$E_{int} = \frac{T}{N}\sum_{n,k,\sigma} \epsilon_k G_\sigma(k, i\omega_n) + UD, \tag{2.10}$$

where D is the double occupation, T is temperature and ϵ_k is the bare dispersion relation. In the weak-coupling CT QMC method, the double occupation D is also

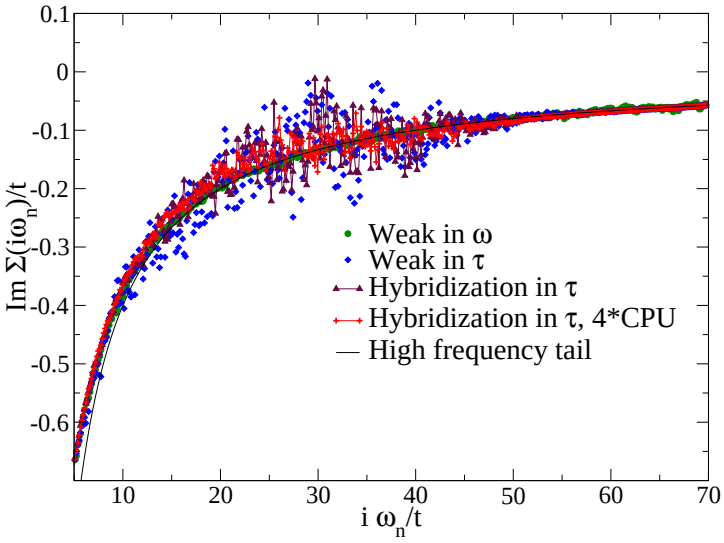

Figure 2.10: Noise in the higher frequencies of hybridization method is clearly visible. The weak-coupling algorithm converge smoothly to the high frequency tail. [Phys. Rev. B 75, 085108 (2007) [57]]

calculated by

$$D = 0.5 + \alpha(1+\alpha) - \frac{< k >}{\beta U N_c}, \tag{2.11}$$

where $< k >$ is the average perturbation order, α is a small number to remove the Fermionic sign problem and N_c is the cluster size. Since we used α=-0.4 due to the symmetry form, the matrix size for the simulation is reasonable in respect of computational time. We employ the two methods to estimate the total internal energy as a function of temperature and the ground state energy. As the first method, we assume that the system follows the Fermi-liquid theory. According to the Fermi-liquid theory, the total internal energy at low temperature is given as

$$E(T) = E(T=0) + \frac{1}{2}\gamma T^2, \tag{2.12}$$

because the specific heat is $C_v = \gamma T$. We calculate the total internal energy at T=0.05, T=0.04, T=0.025 and T=0.02 for U/t=3.5. Specifically, the total internal energy at T=0.05 and T=0.04 are calculated very exactly. We insert these values into Eq. (2.12) and we can calculate the total internal energy as a function of temperature by solving the second-order equation. The curve, which is obtained from the second-order equation, has the form

$$E_{second-order}(T) = -0.853725 + 0.550004T^2. \tag{2.13}$$

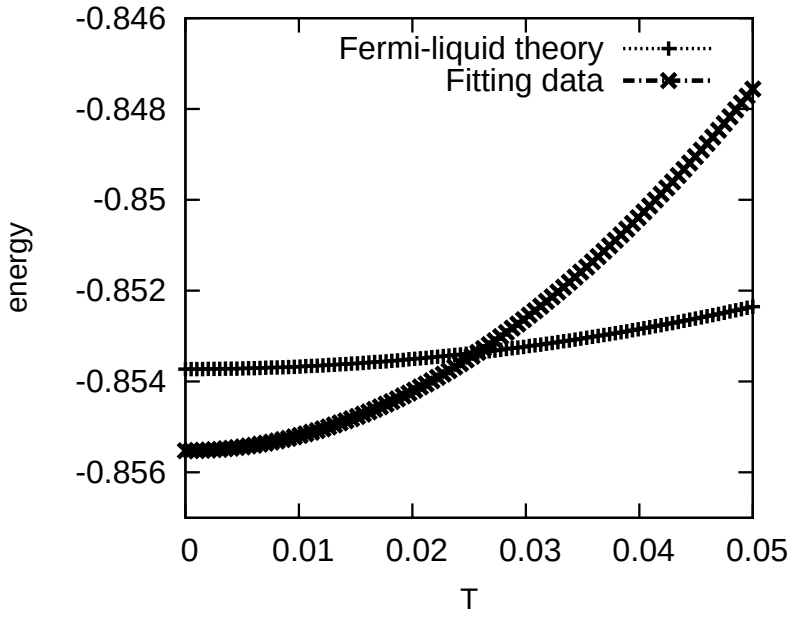

Figure 2.11: The curve (indicated as Fermi-liquid theory) calculated by Eq. (2.12). The curve (indicated as Fitting data) is obtained from the third-order fitting method.

As another method, we estimate the total internal energy by fitting of data at T=0.05, T=0.04 and T=0.025 (third-order). The fiting curve to this data is given as

$$E_{third-order}(T) = -0.85552177 + 3.286007T^2 - 40.5782557T^4. \tag{2.14}$$

The graph of both fitting curves is exhibited in Fig. (2.3.4). The ground state energy of both methods estimate -0.853725 and -0.85552177 (The total internal energy is -0.8545644 at T=0.02). Moreover, the γ in second-order and third-order estimate γ=1.1 and γ=6.56, respectively. In this calculation the values of both data are quite different. There are two possible reasons for this difference. The first one is that the deviation comes from numerical error. Practically, in order to obtain reliable QMC data we need to remove a computational error below 10^{-5}. In our calculation the error is approximately 10^{-4}. The second one is that there might be a kink structure in the specific heat data. According to a recent paper [29] by A. Toschi et al., an abrupt change from one linear behavior to a second one with a reduced slope at higher temperatures for strongly correlated electron system, using the single-site DMFT method combined with exact diagonalize method, was found. They also compared their results with experimental results. We present their results in Fig. (2.12). The experiment data came from measurement for the specific heat of LiV_2O_4 and there is a kink at T=6 Kalvin [4]. One also found a kink in the specific heat of

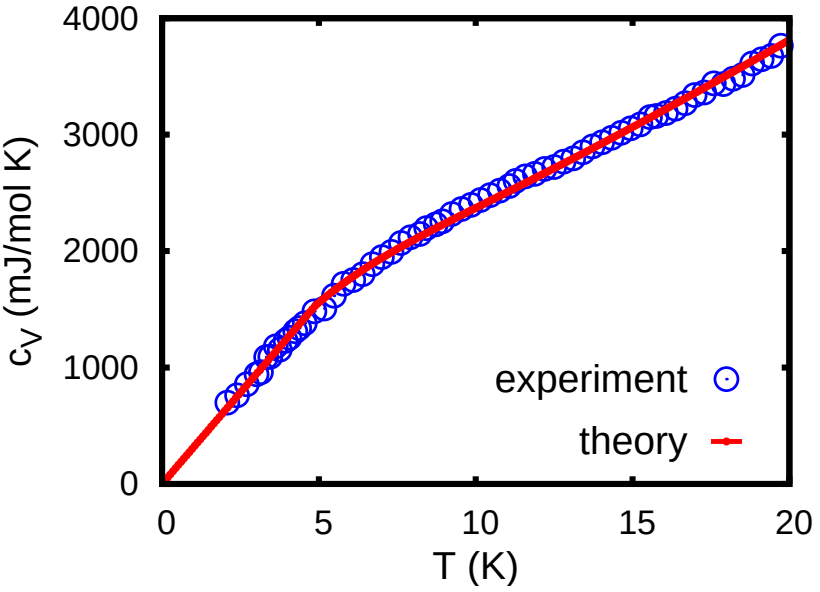

Figure 2.12: Kink in the low temperature specific heat of Li_2O_4 clearly visible at T=6K. [arXiv:0712.3723 (2007) [29]]

f-electron heavy Fermions like $YbRh4_2Si_2$ [30]. As temperature is decreased, we can guess that a slope should be increased like Fig. (2.12) in our calculation. However, the theoretical results in our simulation and in that of A. Toschi have still problems because we need very accurate data. In this part we do not make a conclusion about the Fermi-liquid theory and specific heat. More detailed study and careful numerical simulation are needed to decide if the Fermi liquid theory is applicable. This is the subject of ongoing research.

2.4 Conclusion

In this section we discussed the two-plane Hubbard model on the Bethe lattice and the Hubbard model on the square lattice using the DMFT and cluster-DMFT methods, respectively. In the two-plane Hubbard model, we found that the quasiparticle weight Z has a kink behavior around a first-order transition regions. As t_{AB} is increased, this kink disappears because a continuous transition is presented. We have measured the double occupancy in order to find a clear boundary between band insulator and Mott insulator by tuning t_{AB} at strong Hubbard interaction U/t=6 because the Mott-band insulator transition is expected on this line. In our double occupancy calculation, we found a crossover behavior.

Next we discussed the Hubbard model on the square lattice using different ap-

proximations such as the DMFT, DCA and CDMFT methods. We found that the critical U_c in CDMFT method at N_c=4 is bigger than that of DCA method. This means that the short range fluctuations in CDMFT method is more dominant. Finally, we discussed the Slater-Mott mechanism and Fermi-liquid theory on the square lattice with N_c=4. We found that while the Slater mechanism is dominant in weak-coupling regions, the Mott mechanism is dominant in the strong-coupling regions. We also measured the total internal energy to study the Fermi-liquid theory. Our data suggest that the total internal energy does not allow a definite conclusion about Fermi-liquid theory.

Chapter 3

Hubbard model on the triangular lattice

3.1 Introduction

The physics of systems, which exhibit strong electronic correlations and geometric frustrations at the same time, is still unclear and therefore interesting. Specifically, a recent interesting experiment was performed on organic conductors κ-(BEDT-TTF)$_2$X [31]. The family of quasi-two-dimensional layered organic conductors κ-(BEDT-TTF)$_2$X are model systems which is described as a triangular lattice to study Mott transition, where the BEDT-TTF is bistetrathiafulvalene and X stands for various kinds of anions. In the conducting layer, the BEDT-TTF dimers form triangular lattice in two dimensions. This material can be understood as an antiferromagnetic Mott insulator driven by strong electron correlations. The phase diagram obtained from experiment is shown in Fig. (3.1). At the high temperature there is a crossover behavior between metal and insulator, when this material is put under pressure. As the temperature is decreased, the crossover behavior disappears and this material undergoes a superconducting transition at a pressure of 30MPa. As the temperature is decreased, the system also displays reentrant behavior (insulator-metal-insulator). Theoretically, this system is described by a two-dimensional Hubbard model on the triangular lattice and the pressure, which can induce the transition, is related to the Hubbard interaction U/t. In this section we will explore this model using the single-DMFT, DCA and DF methods which are combined with weak-coupling CT QMC and SCA methods.

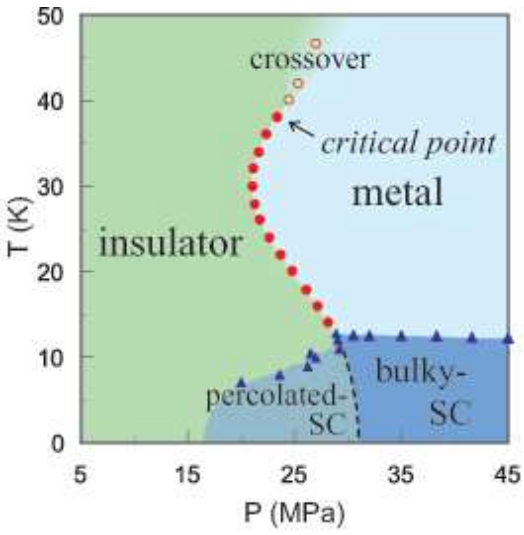

Figure 3.1: Pressure-temperature phase diagram of κ-Cl. Closed circles and open circles represent points at which resistance shows jump. The superconducting transition defined by the resistance vanishing is marked by closed triangles. [Phys. Rev. B 69, 064511 (2004) [49]]

3.2 Model and Motivation

Theoretically, this system is described by a two-dimensional one-band Hubbard model on the triangular lattice. The Hamiltonian is given as

$$H = -t \sum_{\langle i,j \rangle \sigma} c^{\dagger}_{i\sigma} c_{j\sigma} + U \sum_{i} n_{i\uparrow} n_{i\downarrow}, \tag{3.1}$$

where $c_{i\sigma}(c^{\dagger}_{i\sigma})$ is the annihilation (creation) operator of an electron with spin σ at the i-th site, t is the hopping matrix element and U represents the Coulomb repulsion. In order to consider the Brillouin zone , we set the the primitive vectors $\overrightarrow{a_1}$ and $\overrightarrow{a_2}$ for the triangular lattice. The primitive vectors are

$$\overrightarrow{a_1} = (1, 0), \overrightarrow{a_2} = (\frac{1}{2}, \frac{\sqrt{3}}{2}) \tag{3.2}$$

The corresponding primitive vectors $\overrightarrow{b_1}$ and $\overrightarrow{b_2}$ of the reciprocal lattice are given by

$$\overrightarrow{b_1} = (2\pi, -\frac{2\pi}{\sqrt{3}}), \overrightarrow{b_2} = (0, \frac{4\pi}{\sqrt{3}}) \tag{3.3}$$

The Brillouin zone like Fig. (3.4), which has an hexagonal structure, is determined by bisecting of the primitive vectors of the reciprocal lattice. It is well known that on

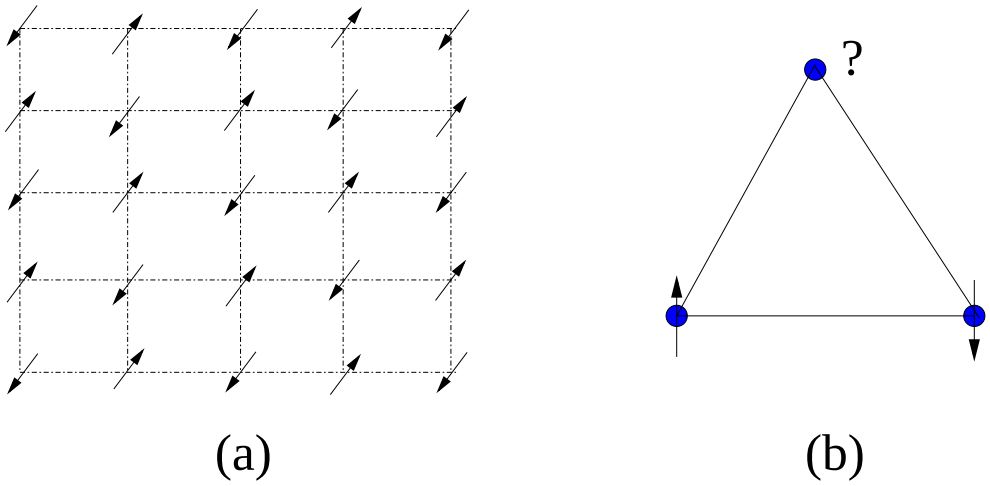

Figure 3.2: (a) The graphical description of an antiferromagnetic state on the square lattice. (b) The graphical description of the triangular lattice. One spin is frustrated due to the geometrical frustration.

the square lattice at half-filling the ground state is a Mott insulator with AF order like Fig. (3.2(a)) because of perfect nesting. There is no metal-insulator transition at zero temperature and the spin density wave is stable on the square lattice at half-filling. However, if we consider the triangular lattice system classically like Fig. (3.2(b)), one spin can not be decided the direction and the spin should be frustrated. Due to this geometrical frustration, this model has broken particle-hole symmetry even at half-filling. The non-interacting density of states at half-filling is shown in Fig. (3.2). The Van Hove singularity is shown around ω=2. Unlike the case of the square lattice, this geometrical frustration suppresses AF order and we expect to find a metal-insulator transition. This model has been studied using varieties of methods such as the path-integral renormalization-group method, quantum Monte Carlo method, the DMFT and the cluster-extension method of DMFT [33, 34, 36, 35, 37, 38, 39]. In this section, we will revisit a model which was presented in a recent paper [32] of Imai and Kawakami using the single-site DMFT and DCA methods with $N_c = 4$. They demonstrated how geometrical frustration suppresses AF correlations in the metallic state using the DCA method combined with noncrossing approximation and fluctuation exchange methods as a cluster solver. However, these cluster solvers are limited as high temperature. For this reason we employ the DCA method combined with CT QMC method to access the low temperature regions as well as to become numerically exact and SCA cluster solvers. Using panoply of the DCA, DF, CT QMC and SCA methods we measure the density of states, double occupancy and spin-spin correlations. We also test newly developed the DF method by comparing Green's function obtained from DMFT, DF and DCA methods and calculate the

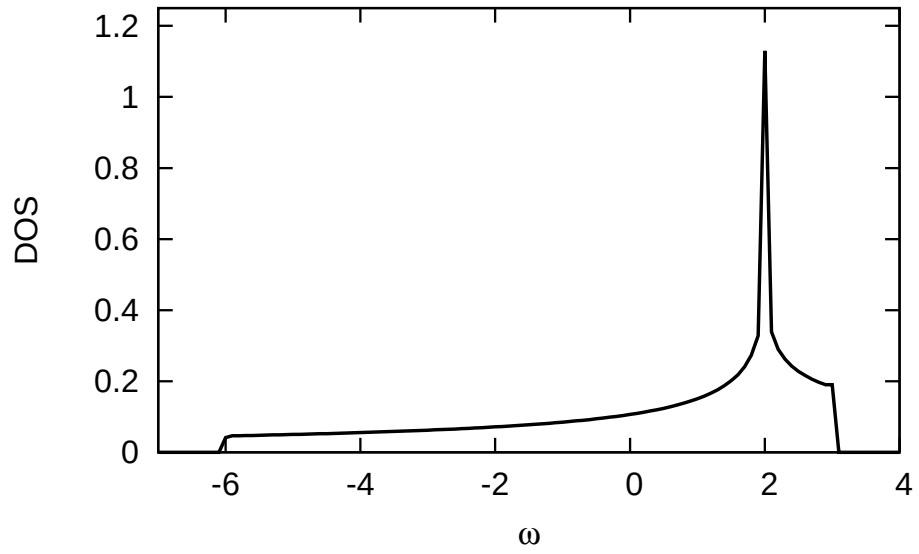

Figure 3.3: The non-interacting density of states on the triangular lattice. The Van Hove singularity is exhibited around $\omega = 2$.

spin susceptibility using the DF method.

3.3 DMFT, DCA, DF and SCA methods

DMFT and DCA methods The DMFT method is described as an average of cluster momenta of the DCA method in the momentum space. First we consider the DCA method with N_c=4 and see how to approximate from the DCA to DMFT method. As a starting point of both methods, we need to know the bare dispersion relation which is given by

$$\epsilon(k) = -2t(\cos(k_x) + \cos(\frac{k_x}{2} + \frac{\sqrt{3}k_y}{2}) + \cos(\frac{k_x}{2} - \frac{\sqrt{3}k_y}{2}), \tag{3.4}$$

for the triangular lattice. We also display the schematic representation of the triangular lattice and Brillouin zone in Figs. (3.4(a) and (c)). The DCA equation is given as

$$\overline{G}_\sigma(\mathbf{K}, i\omega_n) = \frac{1}{N}\sum_{\tilde{\mathbf{k}}} \frac{1}{i\omega_n - \epsilon_{\mathbf{K}+\tilde{\mathbf{k}}} - \Sigma_\sigma(\mathbf{K}, i\omega_n)}, \tag{3.5}$$

where N is the number of lattice sites in each first Brillouin zone which is created by partitioning the original Brillouin zone (doted line in Fig. (3.4)(c)), $\mathbf{K}$ is the cluster

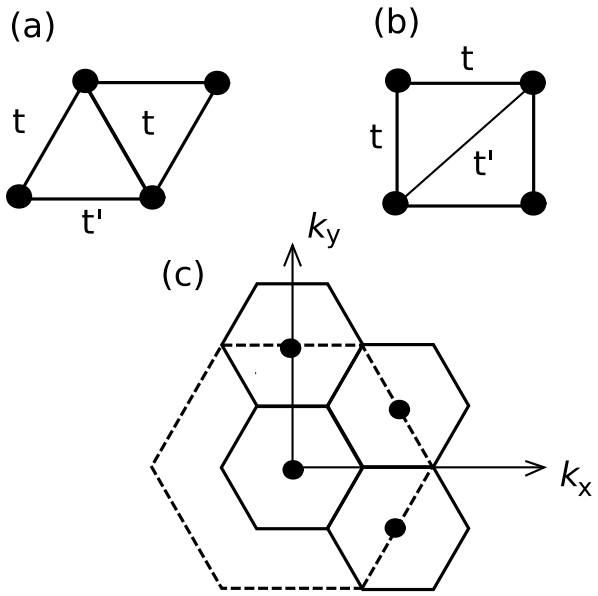

Figure 3.4: (a) Schematic representation of triangular lattice with electron hopping. (b) Equivalent representation of (a) for a square structure. (c) Example of the coarse-graining cells in the Brillouin zone for the triangular lattice (a), where the cluster size is $N_c = 4$.

momenta and the summation over $\tilde{\mathbf{k}}$ is calculated in each of them. The cluster momenta are $\mathbf{K} = (\mathbf{0}, \mathbf{0})$, $\mathbf{K} = (\pi, \pi/\sqrt{\mathbf{3}})$,$\mathbf{K} = (\pi, -\pi/\sqrt{\mathbf{3}})$ and $\mathbf{K} = (\mathbf{0}, \mathbf{2}\pi/\sqrt{\mathbf{3}})$. The detailed bare dispersion relation $\epsilon_{\mathbf{K}+\tilde{\mathbf{k}}}$ is

$$\epsilon_{\mathbf{K}+\tilde{\mathbf{k}}} = -2t(\cos(\mathbf{K_x} + \tilde{\mathbf{k_x}}) + \cos(\frac{\mathbf{K_x} + \tilde{\mathbf{k_x}}}{2} + \frac{\sqrt{3}(\mathbf{K_y} + \tilde{\mathbf{k_y}})}{2}) + \cos(\frac{\mathbf{K_x} + \tilde{\mathbf{k_x}}}{2} - \frac{\sqrt{3}(\mathbf{K_y} + \tilde{\mathbf{k_y}})}{2}). \tag{3.6}$$

The Green's function and self-energy are determined self-consistently by the Dyson equation and Eq. (3.5). The DCA method assumes that the self-energy in each first Brillouin zone is constant. On the other hand, the DMFT method assumes that the self-energy is constant in original Brillouin zone. Therefore, the DCA method with N_c=1 is the same as the DMFT method. The following equation from the DCA method with $N_c = 4$ to single-site DMFT method is

$$G_{on-site} = G(\mathbf{K} = (\mathbf{0}, \mathbf{0})) + \mathbf{G}(\mathbf{K} = (\pi, \pi/\sqrt{\mathbf{3}})) + \mathbf{G}(\mathbf{K} = (\pi, -\pi/\sqrt{\mathbf{3}})) + \mathbf{G}(\mathbf{K} = (\mathbf{0}, \mathbf{2}\pi/\sqrt{\mathbf{3}})) \tag{3.7}$$

DF method In the DF method, the self-consistent condition is given as

$$\sum_k g_\omega^{-2}[(\Delta_\omega - \epsilon_k)^{-1} + g_\omega] = 0. \tag{3.8}$$

The fast Fourier transformation is employed to integrate the self-consistent condition and the dual self-energy. However, it is quite inconvenient to integrate Eq. (3.8) using the fast Fourier transformation, because the Brillouin zone has hexagonal structure. we use the dispersion relation $\epsilon_k = -2t[\cos(k_x) + \cos(k_y) + \cos(k_x + k_y)]$ based on the correspondence of a triangular lattice to a square lattice with diagonal hopping (b) in Fig. (3.4).

SCA method In this part we will introduce the SCA method as impurity solver for DCA method with a four-site cluster (N_c=4) which is exhibited as the triangular lattice like the structure of Fig. (3.3). From standard formalism of the SCA method, the partition function is given as a functional integral over 2×4-component spin and site-dependent spinor fields $c^\dagger$ and c as

$$Z = \int \mathcal{D}[c_i^\dagger c_i] e^{-S_{eff}}, \tag{3.9}$$

where

$$S_{eff} = \int_0^\beta d\tau \int_0^\beta d\tau' d\tau \; c^\dagger(\tau)\mathbf{a}_\sigma(\tau,\tau')c(\tau') \tag{3.10}$$

$$+ \int_0^\beta d\tau \sum_{i=0}^{N_c-1} U n_{i,\uparrow}(\tau) n_{i,\downarrow}(\tau), \tag{3.11}$$

Here $\mathbf{a}_\sigma(\tau,\tau')$ is the Weiss field which is determined self-consistently by Eq. (3.5), N_c is the number of site and β is the inverse temperature. In this model we consider the paramagnetic case and $\mathbf{a}_\sigma$ is given as

$$\mathbf{a}_\sigma(\tau,\tau') = \begin{pmatrix} a_{0\sigma} & a_{1\sigma} & a_{1\sigma} & a_{1\sigma} \\ a_{1\sigma} & a_{0\sigma} & a_{1\sigma} & a_{1\sigma} \\ a_{1\sigma} & a_{1\sigma} & a_{0\sigma} & a_{1\sigma} \\ a_{1\sigma} & a_{1\sigma} & a_{1\sigma} & a_{0\sigma} \end{pmatrix}$$

We can decouple the interaction term as

$$U n_{i\uparrow}(\tau) n_{i\downarrow}(\tau) = \frac{U}{4}\left[N_i^2(\tau) - M_j^2(\tau)\right], \tag{3.12}$$

with $n_{i\uparrow}n_{i\downarrow} = \frac{1}{4}\left((n_{i\uparrow}+n_{i\downarrow})^2 - (n_{i\uparrow}-n_{i\downarrow})^2\right) = \frac{1}{4}(N_i^2 - M_i^2)$. We employ the continuous Hubbard-Stratonovich (HS) transformation in order to decouple M terms related to auxiliary field $\phi_j(\tau)$. Here we assume that $\phi_j(\tau)$ is τ independent and N term is neglected because charge fluctuations are small at half-filling ($N(\tau) = 1$). If one want to consider the charge fluctuations, it is decided in the saddle-point approximation which is given by another field. By a Grassmann integration we can rewrite the partition function as a four-dimensional integral in terms of ϕ_j and the fermionic Matsubara frequency. The partition function is

$$Z = \int d\vec{\phi_j} e^{-S_{eff}[\mathbf{a}(i\omega),\phi_j]}, \tag{3.13}$$

where the effective action $S_{eff} = \beta V$ is defined by

$$V(\vec{\phi}) = \frac{{\phi_1}^2 + {\phi_2}^2 + {\phi_3}^2 + {\phi_4}^2}{U} - T\sum_{\omega_n,\sigma} \ln\det[-\beta\mathcal{M}] \tag{3.14}$$

where $\mathcal{M}$ is defined as

$$\mathcal{M} = \begin{pmatrix} a_{0\sigma}+\phi_1\sigma_z & a_{1\sigma} & a_{1\sigma} & a_{1\sigma} \\ a_{1\sigma} & a_{0\sigma}+\phi_2\sigma_z & a_{1\sigma} & a_{1\sigma} \\ a_{1\sigma} & a_{1\sigma} & a_{0\sigma}+\phi_3\sigma_z & a_{1\sigma} \\ a_{1\sigma} & a_{1\sigma} & a_{1\sigma} & a_{0\sigma}+\phi_4\sigma_z \end{pmatrix}$$

Here σ_z is the z-component Pauli matrix. By definition the impurity Green's function is given by

$$G_j(i\omega_n) = \frac{1}{N_c}\frac{\delta \ln Z}{\delta a_j}, \tag{3.15}$$

we can calculate the local Green's function $G_0(i\omega_n)$ and nearest-neighbor Green's function $G_1(i\omega_n)$. The local Green's function $G_0(i\omega_n)$ is

$$G_0(i\omega_n) = \int d\phi_1 d\phi_2 d\phi_3 d\phi_4 e^{-\beta V(\phi)} \frac{\beta^4}{\det[\beta\mathcal{M}]}(X_1 + X_2 + X_3 + X_4 + X_5), \tag{3.16}$$

$$X_1 = (a_{0\sigma}+\phi_1\sigma_z)(a_{0\sigma}+\phi_2\sigma_z)(a_{0\sigma}+\phi_3\sigma_z)$$
$$X_2 = (a_{0\sigma}+\phi_1\sigma_z)(a_{0\sigma}+\phi_3\sigma_z)(a_{0\sigma}+\phi_4\sigma_z)$$
$$X_3 = (a_{0\sigma}+\phi_1\sigma_z)(a_{0\sigma}+\phi_2\sigma_z)(a_{0\sigma}+\phi_4\sigma_z)$$
$$X_4 = (a_{0\sigma}+\phi_2\sigma_z)(a_{0\sigma}+\phi_3\sigma_z)(a_{0\sigma}+\phi_4\sigma_z)$$
$$X_5 = \frac{a_{1\sigma}^2}{3}(12a_{0\sigma} + 3.0 \times (\phi_1\sigma_z + \phi_2\sigma_z + \phi_3\sigma_z + \phi_4\sigma_z))$$

The nearest-neighbor Green's function $G_1(i\omega_n)$ is

$$G_1(i\omega_n) = \int d\phi_1 d\phi_2 d\phi_3 d\phi_4 e^{-\beta V(\phi)} \frac{\beta^4}{\det[\beta\mathcal{M}]}(Y_1 + Y_2 + Y_3 + Y_4), \tag{3.17}$$

$$Y_1 = \frac{2a_{1\sigma}^2}{\sqrt{3}}(4a_{0\sigma} + \phi_1 + \phi_2 + \phi_3 + \phi_4) + \frac{4a_{1\sigma}^3}{3}$$
$$Y_2 = \frac{2a_{1\sigma}}{3}[(a_{0\sigma}+\phi_1)(a_{0\sigma}+\phi_2) + (a_{0\sigma}+\phi_1)(a_{0\sigma}+\phi_3)]$$
$$Y_3 = \frac{2a_{1\sigma}}{3}[(a_{0\sigma}+\phi_1)(a_{0\sigma}+\phi_4) + (a_{0\sigma}+\phi_2)(a_{0\sigma}+\phi_3)]$$
$$Y_4 = \frac{2a_{1\sigma}}{3}[(a_{0\sigma}+\phi_2)(a_{0\sigma}+\phi_4) + (a_{0\sigma}+\phi_3)(a_{0\sigma}+\phi_4)] \tag{3.18}$$

The four-dimensional integration is performed by the classical Monte Carlo method. In order to calculate the density of states in the real frequency space, we need to replace $a_\sigma(i\omega_n) = i\omega_n + \mu$ into $a_\sigma(\omega) = \omega + i\alpha + \mu$. Here α is very small value (α=0.0001) and ω_n and ω are the Matsubara frequency and real frequency, respectively. While the $V(\vec{\phi})$, which is represented as the Monte Carlo weight function, is calculated in the Matsubara frequency space, $a(i\omega)$ is replaced into $a(\omega)$ and it is calculated directly in the real frequency space.

3.4 Numerical results

In this part we present numerical results using the single-site DMFT, DCA and DF methods. The main results is that the system exhibits a first-order metal-insulator transition due to strong geometrical frustration. We also test the DF method by comparing the Green's function obtained from the single-site DMFT, DF and DCA methods. The following quantities are the Green's function, spectral function, density of states, double occupancy, spin-spin correlations and spin susceptibility. Most results in this part were seen in our paper (Phys. Rev. B 78, 205117 (2008)).

3.4.1 Metal-insulator transition within single-site DMFT method

In some ways the single-site DMFT method, which neglects spin correlations, is suitable for system with geometrical frustration, because the impurity site is already frustrated by an external bath in the paramagnetic case. In this part we measure the Green's function as a function of Matsubara frequency and the density of states as a function of real frequency using the Pade approximation for analytical continuation. The density of states is exhibited in Fig. (3.5). As the interaction is increased, the Kondo resonance in which there appears a quasiparticle peak near Fermi energy is shown around U=8.0. Mott gap around the Fermi energy is seen clearly at $U = 14.0$. As we expect, we found the metal-insulator transition due to geometrical frustration. This density of states is similar to that obtained by HFQMC method with maximum entropy method [36].

3.4.2 A first-order metal-insulator transition

Spectral function and density of states At the beginning we compare the one-particle spectral functions obtained from the SCA and CT QMC methods with Pade approximation for analytical continuation. Since the process, in which $G(i\omega)$ calculated by the CT QMC method is converted into $G(\omega)$ with Pade approximation, introduces large error, it is useful check to compare QMC results with the analytical continuation to SCA results which are directly calculated in real frequency space. Moreover, because the systems with geometrical frustration have large a critical

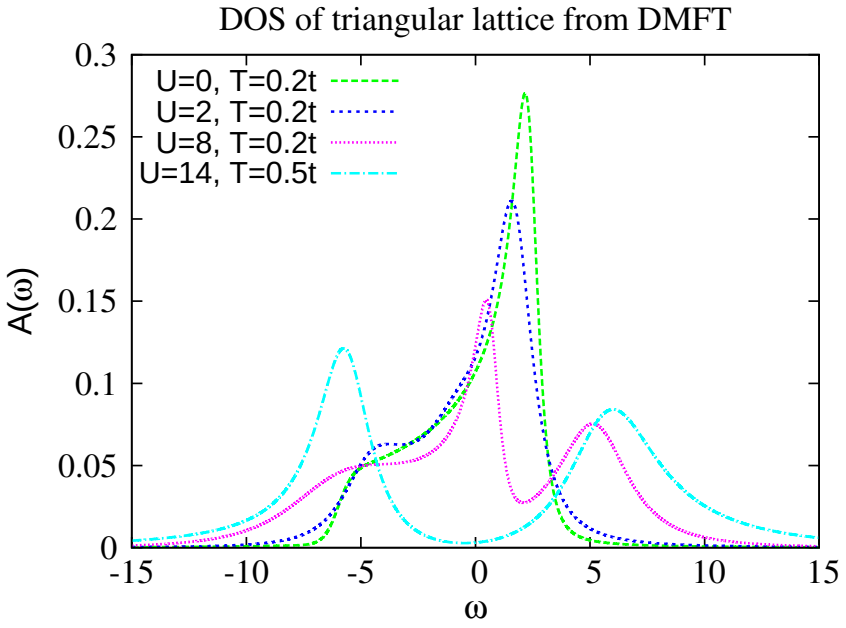

Figure 3.5: The density of states at half-filling for triangular lattice. The ω=0 line determines the location of the Fermi energy. We employ the Pade approximation for analytical continuation.

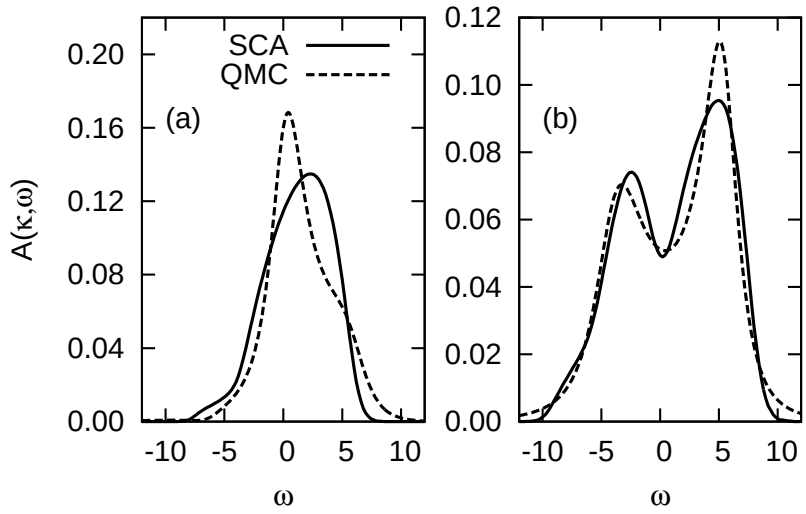

Figure 3.6: One-particle spectral function $A(K,\omega)$ corresponding to the K=(π,$\pi/\sqrt{3}$) for $\beta = 1.6667$, (a) $U = 6$ and (b) $U = 9$ by means of the SCA and CT QMC with Pade approximation.

interaction U_c, the SCA method is suitable for this frustrated model. The spectral function is given by

$$A_\sigma(K,\omega) = -\frac{1}{\pi}\mathrm{Im}G_\sigma(K,\omega) \tag{3.19}$$

We compare the spectral function on the Fermi surface K=($\pi,\pi/\sqrt{3}$). The results are shown in Figs. (3.6(a)-(b)). At $U = 6$ in Fig. (3.6(a)) the difference of both results is that the peak of quasiparticle obtained from QMC method lies around the Fermi level (ω=0) due to the geometrical frustration. On the other hand, the peak obtained from SCA method deviates from the Fermi level (ω=0) because the SCA underestimates the value of the spectral function. At U=9 in Fig. (3.6(b)) the agreement of both results is more reasonable and a (pseudo) gap structure is represented. In order to see the character of system on the triangular lattice more clearly, we compare the density of states for square lattice with that for triangular lattice. We analyze the density of states on the square lattice which is obtained by S. Moukouri and M. Jarrell [42]. Their result is shown in Fig. (3.7). They increased the system size gradually in the weak-coupling regime on unfrustrated square lattice and measured the total density of states. Eventually, even though the quasiparticle peak is clearly visible at $N_c = 1$ in DMFT method due to artificially frustration effect, there is a small gap at $N_c = 16$ which completely disappears at $N_c = 64$. In this system we did not find a metal-insulator transition because the long range AF correlations open gap by the formation of the spin density wave. However, on the triangular lattice the frustration is enough to destroy the AF correlation. In Figs.

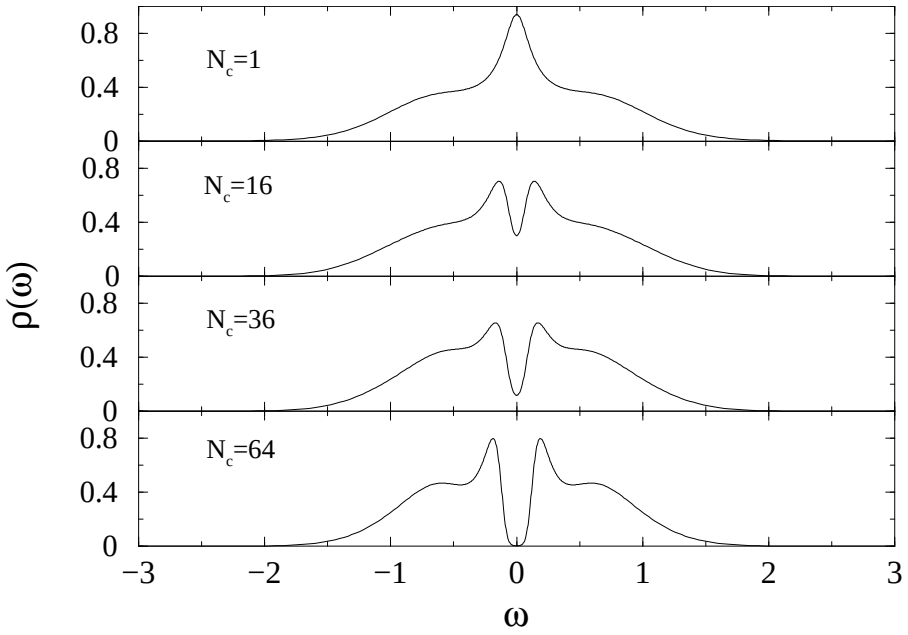

Figure 3.7: The density of states at $\beta = 32$ for $U = 4$. The results are obtained by the HFQMC method combined with the Maximum entropy method for the analytical continuation. [Phys. Rev. Lett. 87, 167010 (2001) [42]]

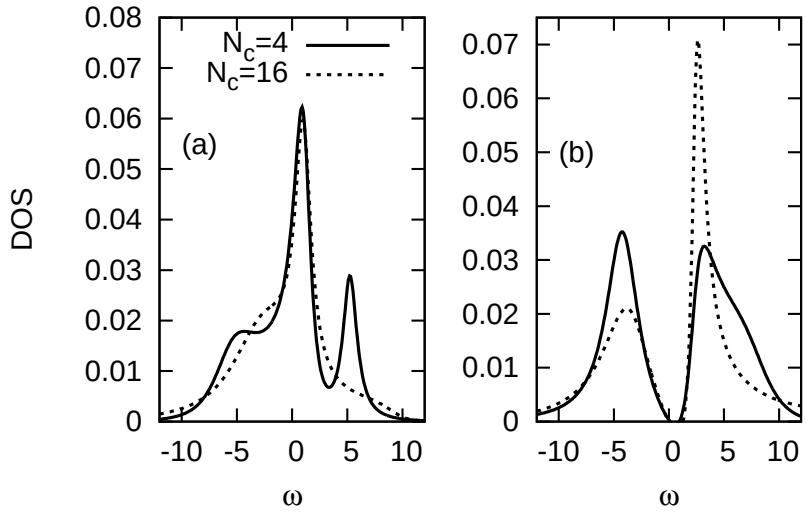

Figure 3.8: Total density of states with $N_c = 4$ and $N_c = 16$ for $\beta = 4$, (a) $U = 6$ and (b) $U = 10$ via CT QMC with Pade approximation. In both lattice sizes the metal-insulator transition is presented.

(3.8(a)-(b)), we can see the MIT by comparing the total density of states for $U = 6$, $U = 10$ and $\beta = 4$ using the DCA method with $N_c = 4$ and $N_c = 16$. Unlike the results for the unfrustrated square lattice, the quasiparticle peak around the Fermi level (ω=0) is clearly seen with increasing N_c at $U = 6$ in Fig. (3.8(a)). At U=10 in Fig. (3.8(b)) we can see the Mott insulator in both $N_c = 4$ and $N_c = 16$. This is strong evidence of a MIT on the triangular lattice.

Double occupancy In the low temperature regime we are also interested in finding whether there is a first-order transition or a continuous transition and how the geometrical frustration effects the system. We expect our system to have a first-order transition because of the recent two cellular DMFT (CDMFT) results [28, 40] which show a first-order transition on the square lattice with $N_c = 4$ and on the triangular lattice with anisotropic hoping at low temperatures. In order to find evidence of a first-order transition we measure the double occupancy as a function of U at several temperatures. Our result is shown in Fig (3.9). The system displays a crossover between metal and insulator at $T = 0.2$. At $T = 0.1$ the double occupancy has a jump behavior around critical interaction U_c and we can see hysteresis which is associated with a first-order transition and at lower temperature hysteresis is clearer.

Spin-spin correlations In order to understand the system more clearly we calculate the nearest-neighbor spin correlation function $\langle S_i^z S_{i+1}^z \rangle$ which is shown in Fig.

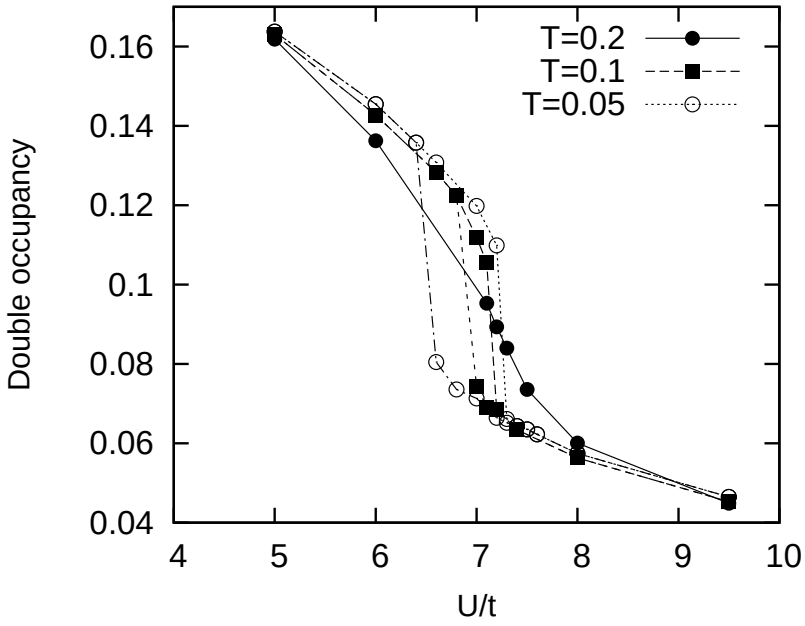

Figure 3.9: Double occupancy as a function of U/t at several temperature for $N_c = 4$. A jump behavior of the double occupancy is shown around critical interaction U_c. The critical interaction U_c are $U_c = 7.2$ for $T = 0.2$, $U_c = 6.9$ for $T = 0.1$ and $U_c = 6.7$ for $T = 0.05$.

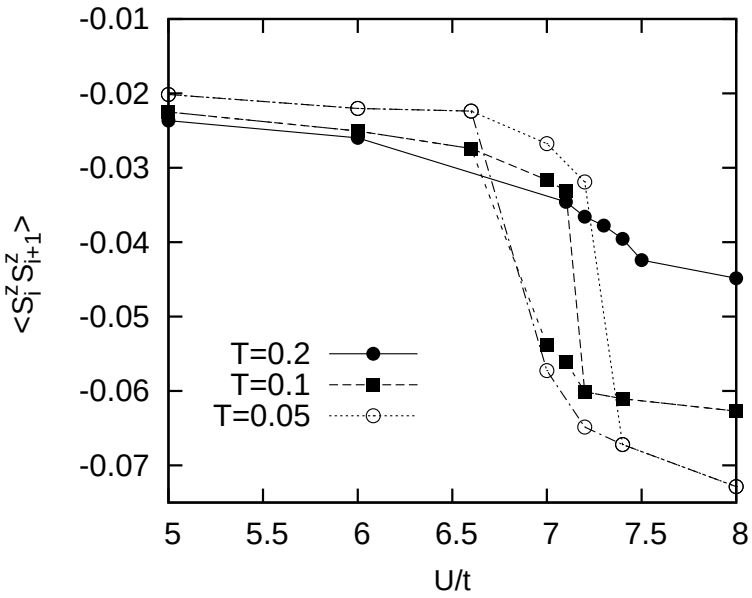

Figure 3.10: The nearest neighbor spin correlation function as a function of U/t at several temperature for $N_c = 4$. The critical inteaction U_c are $U_c = 7.2$ for $T = 0.2$, $U_c = 6.9$ for $T = 0.1$ and $U_c = 6.7$ for $T = 0.05$

(3.10). At U_c a jump of the spin correlation function indicates the MIT arising from competition between the quasiparticle formation and the frustrated spin correlation. Specifically, the spin correlation is enhanced weakly at $U_c = 7.2$ for $T = 0.2$ while it is increased rapidly at U_c in $T < 0.1$. Here is U_c=6.9 for $T = 0.1$ and $U_c = 6.7$ for $T = 0.05$. This means that the entropy at $T = 0.2$ and in $T < 0.1$ is released by geometrical frustration and spin correlation, respectively as temperature decreases and the entropy at insulator state in $T < 0.1$ has small value which triggeres a first-order transition because of a formation of AF state. Moreover, we find that the anomalous character in the metallic state is unlike the results of the nearest-neighbor spin correlation on the Kagome lattice[41]. In the metallic state the spin correlation is weak. This is the reason that geometrical frustration is more dominant than AF spin correlation at lower temperature in the metallic state because the frustration on the triangular lattice is stronger than that on the Kagome lattice. However, in the insulating state AF spin correlation is enhanced stronger than the frustration effect at lower temperature so the spin correlation is strong with decreasing temperature.

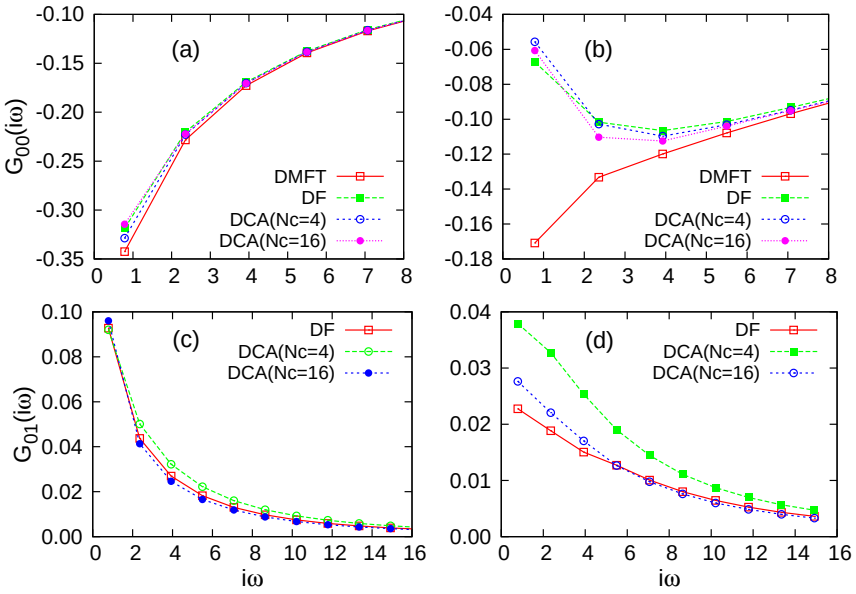

Figure 3.11: The imaginary part of the on-site Green's function for $\beta = 4$, (a) $U/t = 6$ and (b) $U/t = 10$. The real part of the nearest-neighbor Green's function for $\beta = 4$, (c) $U/t = 6$ and (d) $U/t = 10$.

3.4.3 Comparison of Green's functions among the DCA, DF and DMFT methods

In this part we are using the DMFT, DF and DCA methods with N_c=4 and N_c=16 to study the non-local correlation effects and compare the on-site and nearest-neighbor Green's functions in the Matsubara space. In Figs. (3.11(a)-(d)), we present the Green's functions obtained from DMFT, DF and DCA method with $N_c = 4$ and $N_c = 16$ for $\beta = 4$, $U/t = 6$ and $U/t = 10$. The on-site Green's function of DMFT method in Fig. (3.11(a)) is similar to the results of DCA and DF method and all of these indicate the metallic states. A remarkable point is that in Figs. (3.11(a)) and (3.11(c)), both the on-site and nearest-neighbor Green's functions obtained from DF method are closer to those of the DCA method with N_c=16 than $N_c = 4$. In Fig. (3.11(b)) at $U/t = 10$ the on-site Green's function calculated by the DMFT still shows the metallic state which overestimates the value of U_c/t because of the lack of non-local correlation. However, the DCA and DF methods can capture the insulating state and the agreement of the on-site Green's function calculated by the DF and DCA methods with $N_c = 16$ is quite reasonable. In Fig. (3.11(d)), the nearest-neighbor Green's functions obtained from DF method are still closer to those of $N_c = 16$ than $N_c = 4$. This suggests that despite the fact that the DF method is a perturbative method, it can describe physics quite well comparable to the DCA

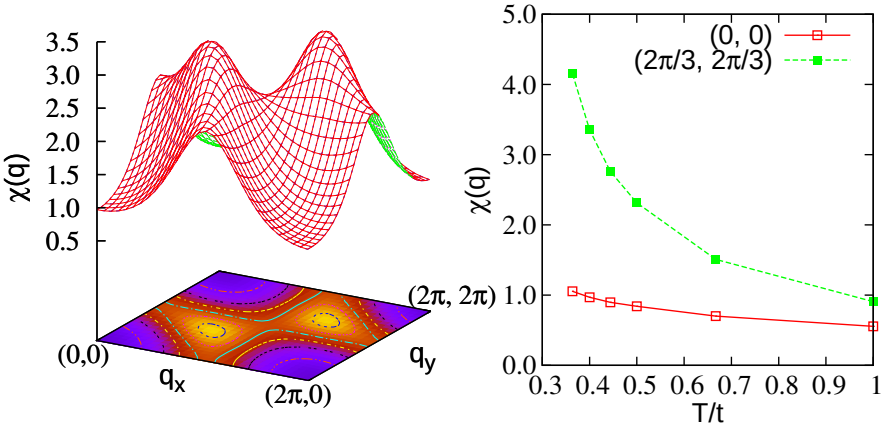

Figure 3.12: (a) The spin susceptibility $\chi(q)$ in the insulating state for U/t=10.0 and $\beta t = 2.5$. (b) The spin susceptibility as a function of temperature at $q = (0, 0)$ and $q = (2\pi/3, 2\pi/3)$.

method with small cluster size. We expect that considering high-order diagrams will improve the results of the DF method.

3.4.4 The spin susceptibility using the DF method

In order to explore the magnetic instability we measure the spin susceptibility using the DF method. The reason why we employ DF method for the spin susceptibility is that the cluster-extension method of the DMFT takes a large amount of time in order to obtain the two-particle properties. On the other hand, because the DF method includes the vertex renormalization through the Bethe-Salpeter equation, the computational burden is not serious and the results are relatively good compared to those of QMC method [18]. Fig. (3.12(a)) shows $\chi(q)$ for U/t=10.0 and $\beta t = 2.5$ where the system is in the insulating state. The $\chi(q)$ has a maximum peak at $q = (2\pi/3, 2\pi/3)$. The spin susceptibility $\chi(q)$ at $q = (2\pi/3, 2\pi/3)$ and $q = (0, 0)$ as a function of temperature is exhibited in Fig. (3.12(b)). As the temperature decreases, $\chi(q)$ at $q = (2\pi/3, 2\pi/3)$ shows strong enhancement of the AF correlations.

3.4.5 The phase diagram for the triangular lattice

In this part, we would like to discuss the phase diagram in the Hubbard model on the triangular lattice. The phase diagram was obtained by T. Ohasi et al. [40]. They explored the Hubbard model on the anisotropic triangular lattice at finite temperature using the CDMFT method combined with HFQMC method. The phase diagram is

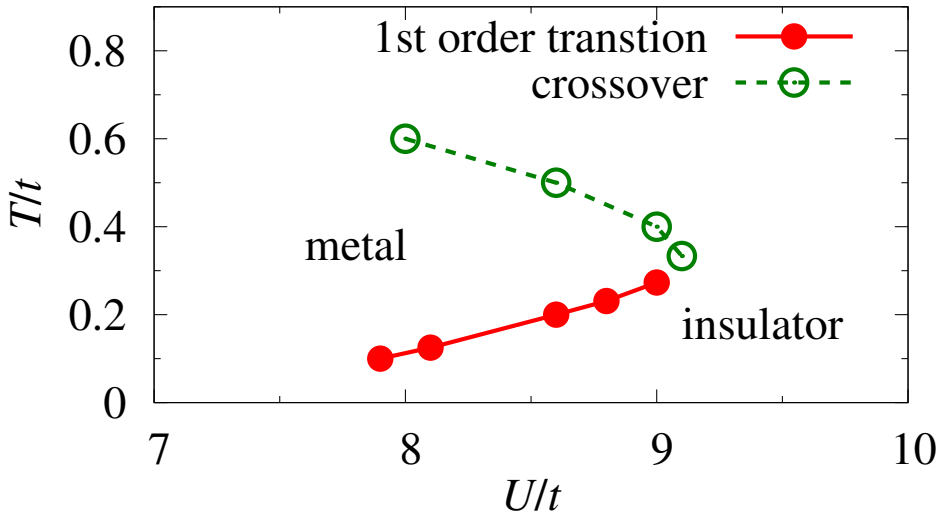

Figure 3.13: Phase diagram of Hubbard model on anisotropic triangular lattice. [Phys. Rev. Lett. 100, 076402 (2008) [40]]

exhibited in Fig. (3.13). The metal-insulator transition is seen clearly in all temperature regions. While the nature of transition shows crossover behavior at high temperature rigime, it is changed to a first-order transition at low temperature rigime. Similar experimental results with the reentrant behavior [insulator-metal-insulator] is exhibited. In our double occupancy calculation which is shown in Fig.(3.9), we found a crossover behavior at high temperature and a first-order transition at low temperature by tuning temperature. Moreover, through analyzing our results (double occupancy) we can guess that the system displays the reentrant behavior, like the case of the anisotropic triangular lattice.

3.5 Conclusion

In conclusion, we have investigated the Hubbard model on the triangular lattice using the DMFT, DCA and DF method. In the single-site DMFT calculation combined with the CT QMC method, we found the metal-insulator transition with critical interaction $U_c/t = 12$. Using the DCA method we compared the spectral functions obtained from SCA and CT QMC methods. We found a good agreement of both methods and the quasiparticle peak and gap structure are presented in the weak and the strong coupling regions, respectively. We found a metal-insulator transition with a first-order transition at low temperatures because of the effect of geometrical frustration. Moreover, we employed the DF method which considers the long range as well as short range correlations and compared the Green's functions of the DF

method to those of the DMFT and DCA method with $N_c = 4$ and $N_c = 16$. We found that the DF method does not only overcome the overestimation of U_c in DMFT method but also that its results are closer the case of $N_c = 16$ than N_c=4. Finally, we calculated the spin susceptibility $\chi(q)$ via DF method. We found that the $\chi(q)$ at $q = (2\pi/3, 2\pi/3)$ grows rapidly as temperature decreases.

Chapter 4

Mott transition in the Hubbard model on the hyper-kagome lattice

4.1 Introduction

Recently, the $Na_4Ir_3O_8$ compound with a S=1/2 three-dimensional network of corner sharing triangles, which is called the "hyper-kagome lattice", was discovered by Y. Okamoto et al [43]. Due to the structure of corner sharing triangles, the system displays the electronic correlations and geometrical frustration at the same time. Each tetrahedron in the pyrochlore lattice (a network of corner shared tetrahedra), which is shown in Fig. 1, consists of Ir (indicated as "filled" circles) and Na (indicated as "empty" circles). S=1/2 spins are carried through Ir^{4+} on the hyper-kagome lattice (blue lines in Fig. 1) because Ir is tetravalent with five electrons in $5d$ orbitals. As the result of the experiment on this compound, a spin liquid state at low temperature was found. Theoretical works, related to this experiment, have mostly addressed the strong-coupling limit using the Heisenberg model[44, 45, 46, 47]. These papers concentrate on the nature of the ground state which was identified as the spin liquid state. Even more recently, it was shown experimental hint that this material might undergoes a transition to a metallic state under pressure. The two important theoretical questions which I will address in this thesis are if the phase diagram shows a reentrant Mott phase with a first-order transition as was found for the anisotropic triangular lattice and if the spin liquid state is stable at finite temperature. For this reason we focus on the nature of the Mott transitions.

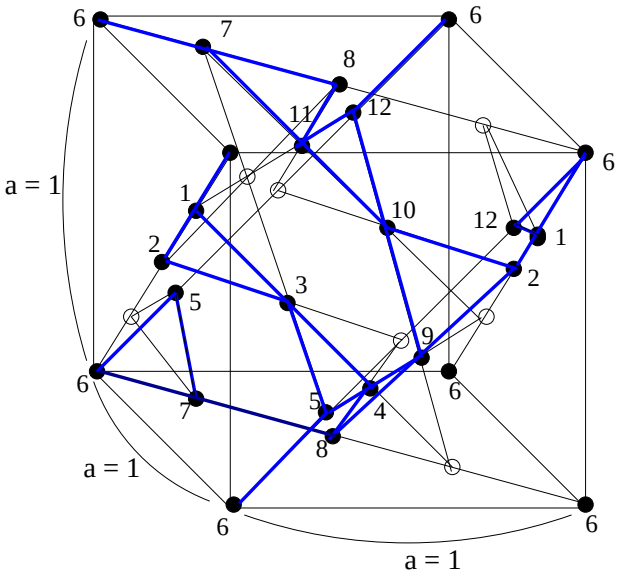

Figure 4.1: In the pyrochlore lattice, "filled" circles and "empty" circles present Ir and Na, respectively. The blue lines show the hyper-kagome lattice of Ir. a is the lattice constant. Lattice points labeled by 1,2,...,12 represent relative positions in each unit cell.

4.2 Model and numerical tool

We consider the Hubbard model on the hyper-kagome lattice at half-filling. The Hamiltonian is given as

$$H = -t \sum_{\langle i,j \rangle \sigma} c^{\dagger}_{i\sigma} c_{j\sigma} + U \sum_{i} n_{i\uparrow} n_{i\downarrow}, \tag{4.1}$$

where $c_{i\sigma}(c^{\dagger}_{i\sigma})$ is the annihilation (creation) operator of an electron with spin σ at the i-th site, t is the hopping matrix element and U represents the Coulomb repulsion. We set t=1.0 and the bandwidth is W=6t (from -4t to 2t). For the DCA method we employ the unit cell which has twelve sites (N_c=12) in the simple cubic lattice, as shown in Fig. 1. In DCA method the Green's functions are freely summed over the wave vectors $\tilde{k}$ of the superlattice due to omission of the phase factors and are determined by the self-consistency condition. Unlike the typical procedure of the DCA method with diagonal hopping matrix in the momentum space, we directly write the hopping matrix T($\tilde{k}$) with the periodic boundary condition in the real space for simulation. Here G_0, Σ and T($\tilde{k}$) are described by 12 $\times$ 12 matrices. In this case the self-consistent equation for DCA method is the same that for CDMFT

method except the hopping matrix T($\tilde{k}$). The self-consistent equation is given by

$$\begin{aligned} G_0^{-1}(i\omega_n) &= \left(\int d\tilde{\mathbf{k}} \frac{1}{i\omega_n + \mu - T(\tilde{\mathbf{k}}) - \Sigma(i\omega_n)} \right)^{-1} \\ &+ \Sigma(i\omega_n), \end{aligned} \tag{4.2}$$

where μ is the chemical potential and ω_n is the Matsubara frequency. The $T(\tilde{\mathbf{k}})$ matrix is given as

$$T(\tilde{\mathbf{k}}) = \begin{pmatrix} 0 & e^{A_0} & e^{A_1} & 0 & 0 & e^{-A_0} & 0 & 0 & 0 & 0 & 0 & e^{A_2} \\ e^{-A_0} & 0 & e^{A_3} & 0 & 0 & 0 & 0 & 0 & e^{A_4} & e^{-A_3} & 0 & 0 \\ e^{-A_1} & e^{-A_3} & 0 & e^{A_1} & e^{A_5} & 0 & 0 & 0 & 0 & 0 & 0 & 0 \\ 0 & 0 & e^{-A_1} & 0 & e^{A_2} & 0 & 0 & e^{A_0} & e^{-A_2} & 0 & 0 & 0 \\ 0 & 0 & e^{-A_5} & e^{-A_2} & 0 & e^{A_4} 0 & e^{A_5} & 0 & 0 & 0 & 0 & 0 \\ e^{A_0} & 0 & 0 & 0 & e^{-A_4} & 0 & e^{A_3} & 0 & 0 & 0 & 0 & e^{A_4} \\ 0 & 0 & 0 & 0 & e^{-A_5} & e^{-A_3} & 0 & e^{A_3} & 0 & 0 & e^{A_1} & 0 \\ 0 & 0 & 0 & e^{-A_0} & e^{-A_3} & 0 & 0 & e^{-A_4} & 0 & 0 & e^{A_0} & 0 \\ 0 & e^{-A_4} & 0 & e^{A_2} & 0 & 0 & 0 & e^{A_4} & 0 & e^{-A_5} & 0 & 0 \\ 0 & e^{A_3} & 0 & 0 & 0 & 0 & 0 & 0 & e^{A_5} & 0 & e^{-A_1} & e^{-A_5} \\ 0 & 0 & 0 & 0 & 0 & 0 & e^{-A_1} & e^{-A_0} & 0 & e^{A_1} & 0 & e^{-A_2} \\ e^{-A_2} & 0 & 0 & 0 & 0 & e^{-A_4} & 0 & 0 & 0 & e^{A_5} & e^{A_2} & 0 \end{pmatrix},$$

with $A_0 = i(-k_x - k_z)/4$, $A_1 = i(k_y - k_z)/4$, $A_2 = i(k_x - k_y)/4$, $A_3 = i(k_x + k_y)/4$, $A_4 = i(-k_y - k_z)/4$ and $A_5 = i(k_x - k_z)/4$. The Brillouin zone of superlattice also becomes simple cubic lattice, $\pi/\mathrm{a} < k_x,\ k_y,\ k_x < \pi/\mathrm{a}$, where a = 1 is the lattice constant and the summation of $\tilde{k}$ is taken over the Brillouin zone of the superlattice. 8×10^6 $\tilde{\mathbf{k}}$-points are used for integration of Eq. (4.2). We also employ the CT QMC method as cluster solver. We use 3×10^6 QMC sweeps approximately and consider twenty-one Matsubara frequency points for CT QMC simulation.

4.3 Numerical results

4.3.1 Phase diagram

Now let us investigate the phase diagram of the hyper-kagome lattice Hubbard model at half filling. In order to check the existence of a gap we estimate the density of states at Fermi level ($\omega = 0$) by using the Pade approximation and the analytic form which is given by

$$G(\beta/2) \approx \frac{1}{\beta} \rho(\omega = 0), \tag{4.3}$$

where β is the inverse temperature and $\rho(\omega)$ is the density of states. Because Eq. (4.3) is satisfied at sufficiently low temperature, we employ the Pade approximation

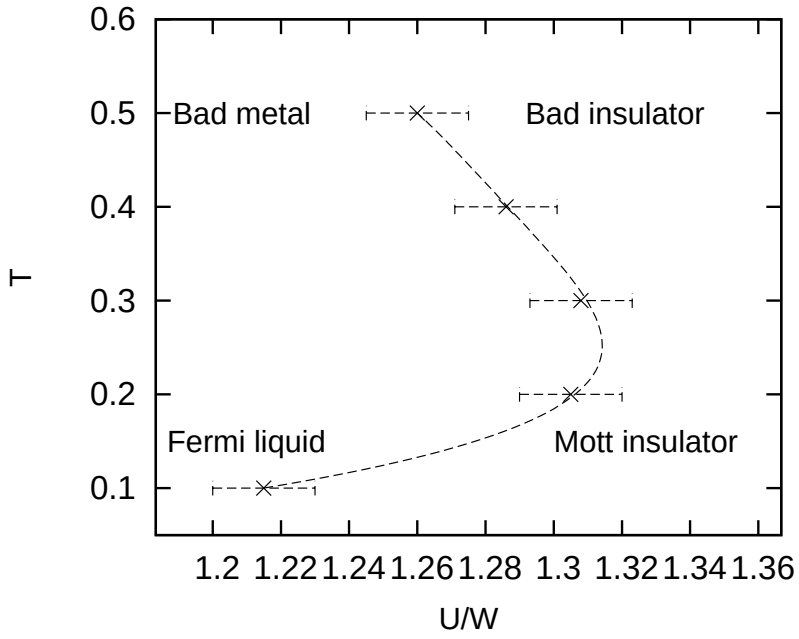

Figure 4.2: Phase diagram of the Hubbard model on the hyper-kagome lattice.

in T>0.1 regions and compare the results of both methods at T=0.1. The Pade approximation method for analytical continuation is reasonable at the high temperature regime due to very small error in CT QMC method. Moreover, the results of Eq. (4) guarantee those obtained from the Pade approximation at low temperature. The phase diagram in U-T plane is shown in Fig. (4.2). As the temperature is decreased in the transition region (U/W=1.28) above T=0.3, the system prefers the metallic state due to the development of itinerancy of electrons. Below T=0.3 the system is strongly controlled not by itinerancy electrons but by antiferromagnetic (AF) fluctuation which is ignored in the single-site DMFT, as temperature is decreased. Therefore, the Mott insulator lies in the low temperature regions. This means the reentrant behavior which is shown in the Hubbard model on anisotropic triangular lattice [40] related to the organic material κ-(BEDT-TTF)$_2$Cu[N(CN)$_2$]Cl [48, 49].

4.3.2 Continuous metal-insulator transition

We analyze the density of states close to critical U/W at T=0.1 using the Pade approximation for analytical continuation. The density of states for U/W=0.5, 1.167, 1.2 and 1.25 are exhibited in Figs. 4.3(a)-(d). At U/W=0.5 the density of states displays the van-Hove singularity and shoulder-like structure around Fermi energy

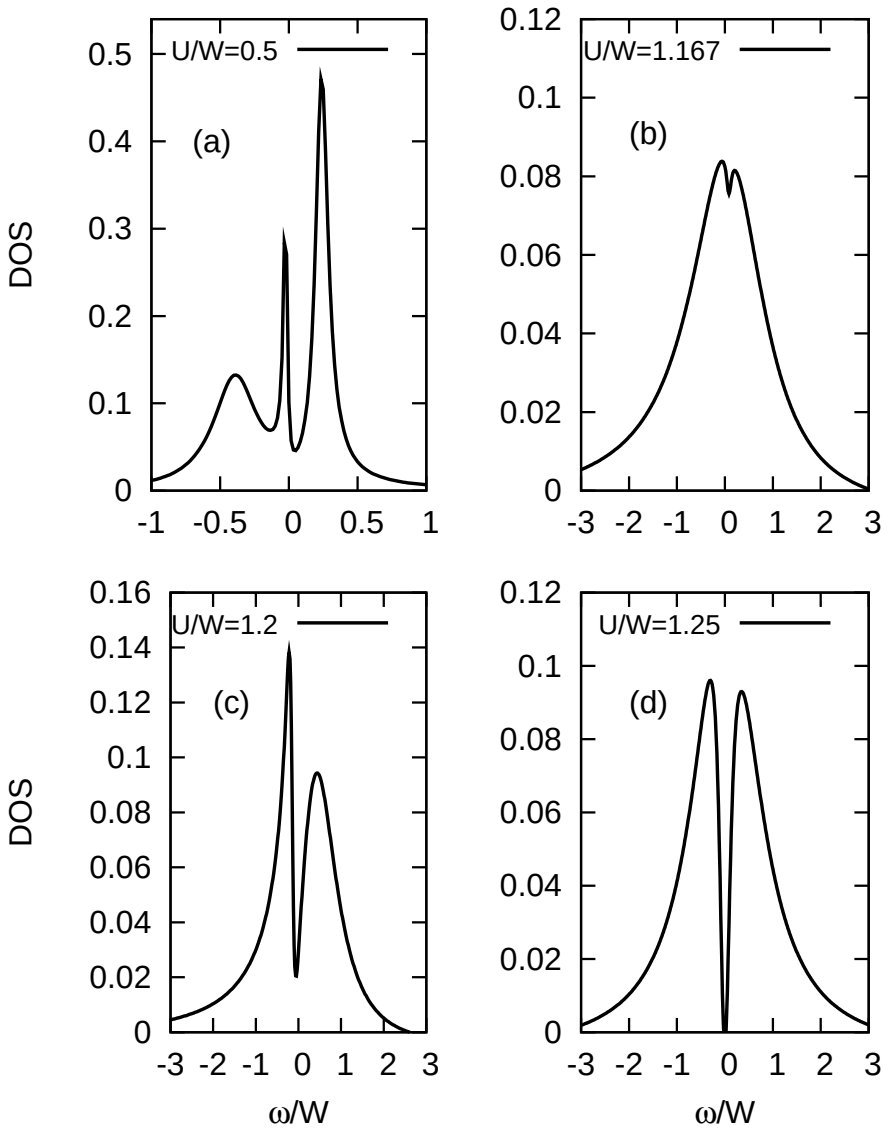

Figure 4.3: The density of state corresponding to (a) U/W=1.17, (b) U/W=1.167, (c) U/W=1.2 and (d) U/W=1.25 for T=0.1. The Pade approximation is employed for analytical continuation

same as recents obtained by the CDMFT+iteration pertubation theory [60]. At U/W=1.167, the quasiparticle peak due to itinerancy of electron is formed strongly around the Fermi level. At U/W=1.2 the density of states is changed dramatically at the Fermi level and the system turns to a Mott insulator at U/W=1.25. From these results we did not observe the evidence for the pseudogap formation like the results of kagome lattice [41]. The magnetic states are suppressed due to the geometrical frustration in contrast to the square lattice [42]. To see the character of Mott transition in more detail we present the double occupancy as a function of temperature for various interactions in Figs. 4.4(a)-(c). As temperature is decreased at weak interaction strength U/W=1.0 in Fig. 4.4(a), the double occupancy is increased. This means that the entropy due to the itinerancy of electrons (quasiparticles) is optimized by pushing the interaction in order to decrease the free energy. The non-monotonic dependence of the double occupancy is observed at intermediate interaction U/W=1.2 in Fig. 4.4(b). For T >0.3 the system displays the insulator state due to effect of the dominant local magnetic moment. As temperature is decreased, it changes into the metallic state due to development of the quasiparticle. After passing a peak temperature T_0=0.15, at lower temperatures the system reenters the insulator state again because the magnetic correlations get enhanced. These are indeed evidence of a reentrant behavior which is shown in geometrical frustrated systems like the Hubbard model on anisotropic triangular lattice. In Fig. 4.4(c), we see a small gradual increase in the double occupancy as temperature is decreased, reflecting the Mott physics effect of kinetic energy gain. Our analysis in the Fermi liquid region (U/W=1.0) and Mott insulator region (U/W=1.33) are similar to those which are obtained from the cluster-extension of DMFT and single-site DMFT on the square lattice [56]. We further investigate the double occupancy as function of interaction for various temperatures in order to see the type of transition. The result is presented in Fig. (4.5. As interaction is increased, at T=0.2 the double occupancy decreases smoothly because of the development of local magnetic moment. At T=0.1 a "critical slowing down" behavior is observed around U_c/W=1.2. This behavior is quite similar to the results of the fully frustrated Hubbard model which indicates a second-order transition in the single-site DMFT calculation [50]. Even if we did not investigate lower temperature regions due to computational load, it might be a continuous transition in the Hubbard model on the hyper-kagome lattice.

4.3.3 Spin-spin correlations

We calculate the nearest-neighbor $\langle S_i^z S_{i+1}^z \rangle$ and next nearest-neighbor spin-spin correlation $\langle S_i^z S_{i+2}^z \rangle$ which are shown in Fig (4.6). In the weak interaction regions the system displays paramagnetic metalic state, unlike the case of square lattice which is enhanced the AF state due to perfect nesting. As the interaction is increased, there is a competition between the quasiparticle formation and the frustrated spin correla-

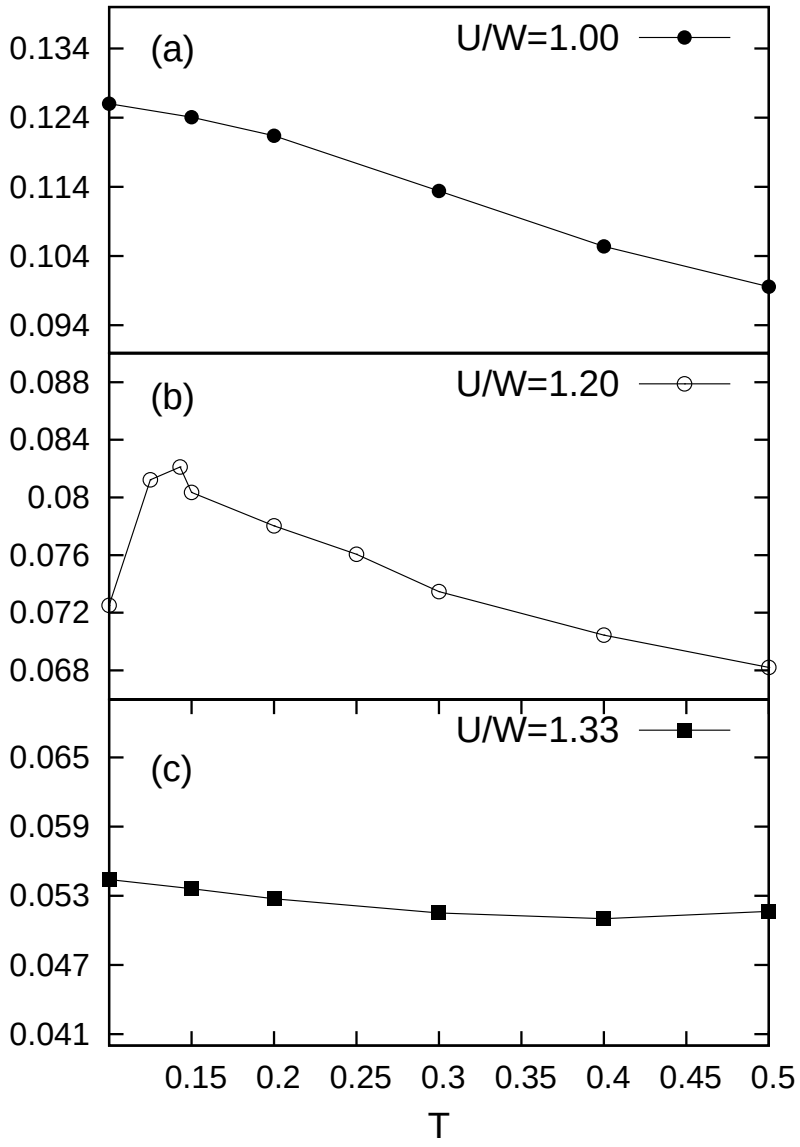

Figure 4.4: Double occupancy as a function T for (a) U/W=1.0, (b) U/W=1.2 and (c) U/W=1.333.

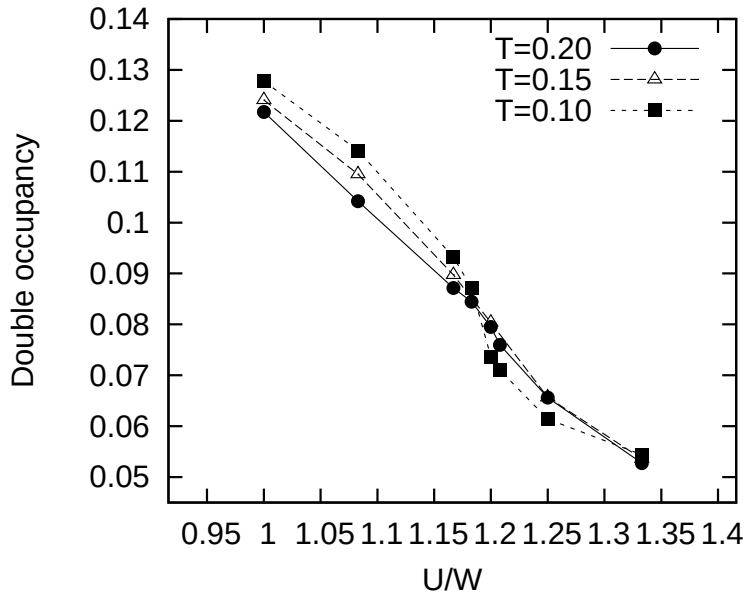

Figure 4.5: Double occupancy as a function of U/W for T=0.2 and T=0.1. There is a "critical slowing down behavior" at T=0.1 which represents the evidence of a continuous transition. U_c/W=1.2 for T=0.1

tion. At U_c/W=1.27 for T=0.2 both the nearest-neighbor and next nearest-neighbor spin-spin correlations are enhanced at the same time. In the strong interaction regions we find the AF order in the short range. Even if AF order in the cluster is shown, it is difficult to conceive a well-established long range ordering in our method. The dual fermion method, which can capture the long range correlations, might be a good candidate for this study.

4.3.4 Comparison mean-field calculation with our calculation

In this part we would like to compare our results with recent those which are obtained from the mean-field calculations. The phase diagram, which is obtained from the mean field calculation, is exhibited in Fig. (4.7) [52]. According the analysis by mean field calculation, on the insulating side the conductivity is thermally activated as temperature is decreased. On the metallic side the conductivity has a minimum value before it grows and saturates at low temperature. The resistivity has the opposite behavior of the conductivity. Both results are sketched in Figs. (4.7(b) and (c)). In respects of the phase diagram in Fig. (4.7(a)), it is quite different from our result, which is shown in Fig. (4.2). In the mean field calculation there are

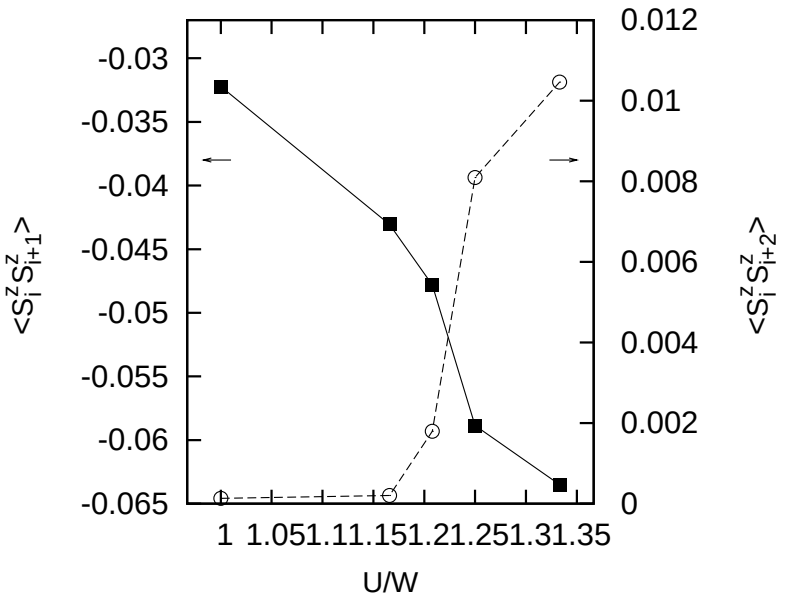

Figure 4.6: The nearest-neighbor and next nearest-neighbor spin-spin correlation function as a function of U/W for T=0.2. Both spin-spin correlations are rapidly increased at U_c/W=1.27

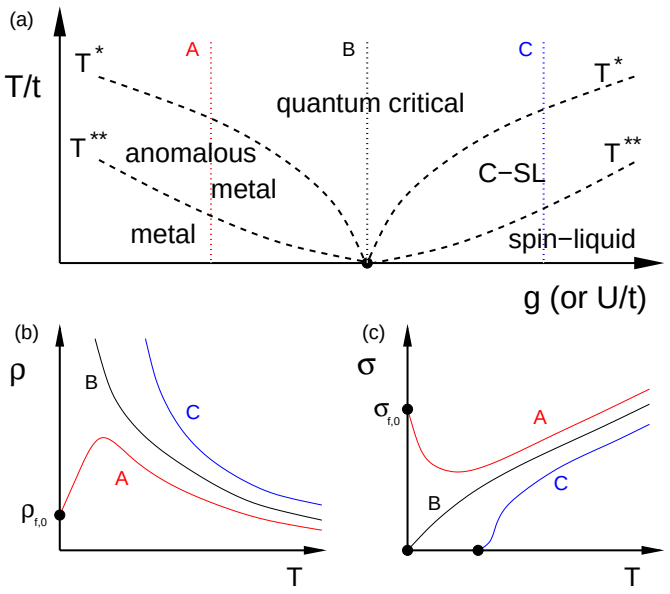

Figure 4.7: (a) Schematic phase diagram on the hyper-kagome lattice obtained from mean-field calculation. C-SL labels the Charge flutuation renomalized Spin Liquid. (b) Resistivity and (c) conductivity. [arXiv:0811.2218 [52]]

transitions in the metallic state and insulating state, as temperature is decreased. The system does not also display reentrant behavior. However, both systems present the metal-insulator transition. Moreover, the system in the mean field calculation displays a continuous metal-insulator transition at critical interaction U_c/W=1.03. These results are comparable with our results with a continuous metal-insulator transition at U_c/W=1.2 for T=0.1.

4.4 Conclusion

In conclusion, we presented the results of DCA study combined with CT QMC method as cluster solver in the Hubbard model on the hyper-kagome lattice. This hyper-kagome structure, which is a three-dimensional network formed by corner sharing triangles, is related to the $Na_2Ir_3O_8$ compound. We found that the phase diagram in the U-T plane has reentrant behavior due to geometrical frustration. This phase with reentrant behavior is analog of the layered triangular lattice organic material κ-$(ET)_2Cu_2(CN)_3$ which is described as the Hubbard model on the anisotropic triangular lattice. The difference of both results is that while the results on the hyper-kagome exhibit a continuous transition, those on the anisotropic triangular lattice display a first-order transition. Using Pade approximation for the analytical continuation, we calculate the density of states close to critical U_c/W=1.2 for T=0.1. There is rapid change in the density of states at Fermi level and the pseudogap formation is not observed because magnetic states are suppressed. We investigated the double occupancy as a function of temperature and as a function of interaction U/W to study the nature of Mott transition in more detail. For intermediate values of the interaction the double occupancy as a function of temperature has non-monotonic behavior which represents the character of reentrant behavior. We also find a "critical slowing down" of double occupancy as a function of interaction. Even if we did not explore the lower temperature regions, this might be a signal of a continuous transition. Finally, we calculated the nearest-neighbor and next nearest-neighbor spin-spin correlations as a function of interaction. We can observe the paramagnetic metallic state in the weak-coupling regions. When interaction passes the critical point, both nearest-neighbor and next nearest-neighbor spin-spin correlations are increased rapidly. In the strong-coupling regions the system shows the AF order in the cluster. We did not observe the spin liquid state (paramagnetic Mott insulator) at lower temperature (zero temperature) or large cluster due to limitation of numerical tool. However, from our calculation we expect that the continuous Mott transition with reentrant behavior will be observed experimentally.

Chapter 5

Summary

In the first part of the dissertation, we discussed the single-site DMFT, cluster-DMFT (CDMFT and DCA), DF, CT-QMC and SCA methods. Here we will summarize about each method shortly. The single-site DMFT method is described as a single-site impurity problem with an external bath. The nonlocal correlations are collapsed by integrating an external bath. It is cheap in terms of computational time and has no bad Fermionic sign problem. On the other hand, it is impossible to describe the spin-spin correlations and d-wave superconductivity due to the lacks of the nonlocal correlations. Unlike the single-site DMFT method, in the cluster-DMFT methods the cluster is inserted in a bath. While the correlations in the cluster are calculated exactly through the QMC method, the long range correlations are only considered on the mean field level. Many theoretical problems such as antiferromanetism and d-wave superconductivity have been investigated through these methods. In terms of computational time, it is expensive and meets the Fermionic sign problem at away half-filling or in the frustration system. The DF method is based on the single-site DMFT method. The local Green's function is calculated exactly within the single-site DMFT method. By a dual transformation, the system is newly described by the dual fields. Since the dual fields are nonlocal in time, the nonlocal correlations can be considered within the diagram expansion method. Like the single-site DMFT method, it is cheap in terms of computational time and has no Fermionic sign. However, the nonlocal correlations are just considered on the perturbative approach. The two CT QMC methods, based on the weak-coupling expansion and the hybridization-coupling expansion, were developed. Both methods are superior to HFQMC method in terms of computational time and face small Fermionc sign problem. The SCA method is strong-coupling approximation with assuming τ=constant and can measure the density of states in the real frequency without analytical continuation. Therefore, it is useful to check the result obtained from QMC method in the strong-coupling regions at high temperature.

In the second part, we discussed the Hubbard model on the Bethe lattice and the square lattice at half-filling using the DMFT and DCA methods. We employed the single-site DMFT method for the two-plane Hubbard model on the Bethe lattice. We found the metal, Mott-insulator and band insulator. The clear transition boundary between the metal and Mott-insulator was presented in the double occupancy and quasiparticle weight calculations. However, we did not find the transition boundary between Mott-insulator and band-insulator and found a crossover behavior at low temperature. Using the DCA method with $N_c = 4$, we explored the Hubbard model on the square lattice. Since the long range correlations are suppressed, the metal-insulator transition and the Fermi liquid physics are presented in this model. We compared the critical interaction U_c of the single-site DMFT, CDMFT and DCA methods (The DMFT and CDMFT results are obtained from Phys. Rev. Lett. 101, 186403 (2008) [28].) Even while we found that the values of the U_c were quite different due to the boundary condition of the cluster between CDMFT and DCA methods, all results displayed the metal-insulator transition which is caused by the short-range correlations or local correlation. We explored the Slater-Mott mechanism through double occupancy calculation. In the weak-coupling region the double occupancy is decreased, as the temperature is decreased. This means that the opening of the gap is related to a reduction of interaction energy (Slater mechanism) with decreasing temperature. In the strong-coupling regions, the Mott physics is dominant due to increasing local antiferromagnetic correlations. We also measure the internal energy to check the Fermi-liquid theory. Practically, an extremely accurate calculation is required, because the specific heat or the free energy is calculated by derivation. For this part we did not reach any conclusion whether there is a kink structure in the specific heat or not, due to statistical errors. The improvement of numerical accuracy and the confirmation of a kink structure is still investigating.

The physics of systems, which exhibit strong electronic correlations and geometric frustrations at the same time, is unclear and interesting. In the last part, we studied the Hubbard model on the triangular lattice in two-dimensions and hyper-kagome lattice in three-dimensions. The system on the triangular lattice is similar to oragnic conductor κ-(BEDT-TTF)$_2$X on experiment and rich phases and metal-insulator transition would be displayed. We employ the DMFT, DCA and DF approximations which is combined with the CT QMC and SCA methods as impurity solvers. In DMFT calculation we found the metal-insulator transition with overestimated large critical $U_c/t = 12.0$, because it makes the system to be more frustrated. In the DCA calculation with $N_c = 4$ the critical U_c/t is around 7.0 and a first-order transition is shown. Moreover, the reentrant behavior (insulator-metal-insulator) is presented by tunning the temperature and this situation is quite similar to the phase

diagram of oragnic conductor κ-(BEDT-TTF)$_2$X on experiment. Comparing the DF method with DMFT and DCA methods, we also test the DF method. The DF method remove overestimated critical U_c/t of the DMFT method and calculate the spin susceptibility fastly. In DF method the critical U_c/t is around 7.5 which is similar to that obtained from the DCA method and the spin susceptibility is enhanced at $q = (2\pi/3, 2\pi/3)$. The interesting $Na_2Ir_3O_8$ compound with a three-dimensional network of corner sharing triangles, which is called the "hyper-kagome lattice" was discovered in experiment. This compound is indicated as the spin-liquid state (paramagnetic insulator) at low temperature and might be experienced a Mott transition by tuning the pressure (A ambiguous signal of a Mott transition was observed in recent experiment). We explore the nature of Mott transition at finite temperature using the DCA method with $N_c = 12$. We found that this model displays a reentrant behavior like the result on the triangular lattice and antiferromagnetic state within temperature accessed by our numerical tool. Even while we did not find the spin liquid state due to limitation of numerical tools by small cluster size, we expect to observe the reentrant behavior in future experiment.

Chapter 6

APPENDIX

Luttinger-Ward functional

We follow the Luttinger-Ward functional [54] which is written by M. Potthoff [53]. The bare Green's function is given as

$$G_{t,0,\alpha,\beta}(i\omega_n) = (\frac{1}{i\omega_n + \mu - t})_{\alpha,\beta}. \tag{6.1}$$

The Green's function is written by

$$G_{t,U,\alpha,\beta}(i\omega_n) = - < c_\alpha(i\omega_n)c^*_\beta(i\omega_n) >_{t,U} = -\frac{1}{Z_{t,U}} \int DcDc^* c_\alpha(i\omega_n)c^*_\beta(i\omega_n) \exp(A_{t,U,cc*}), \tag{6.2}$$

with

$$A_{t,U,cc^*} = \sum_{n,\alpha,\beta} C^*_\alpha(i\omega_n)((i\omega_n+\mu)\delta_{\alpha,\beta} - t_{\alpha,\beta})c_\beta(i\omega_n) - \sum_{\alpha,\beta,\gamma,\delta} U_{\alpha,\beta,\gamma,\delta} \int d\tau c^*_\alpha(\tau)c^*_\beta(\tau)c_\gamma(\tau)c_\delta(\tau). \tag{6.3}$$

The self-energy is

$$\Sigma_{t,U} = G^{-1}_{t,0} - G^{-1}_{t,U}. \tag{6.4}$$

We define the functional :

$$\Omega_U[G^{-1}_0] = -T \ln Z_U[G^{-1}_0] \tag{6.5}$$

with

$$Z_U[G^{-1}_0] = \int DcDc^* \exp(A_{U,c,c^*}[G^{-1}_0]), \tag{6.6}$$

and

$$A_{U,c,c^*}[G^{-1}_0] = \sum_{n,\alpha\beta} c^*_\alpha(i\omega_n)G^{-1}_{0,\alpha\beta}(i\omega_n)c_\beta(i\omega_n) - \sum_{\alpha\beta\delta\gamma} U_{\alpha\beta\delta\gamma} \int d\tau c^*_\alpha(\tau)c^*_\beta(\tau)c_\delta(\tau)c_\gamma(\tau). \tag{6.7}$$

By the derivation of the functional $\Omega_U[G_0^{-1}]$, we can define a functional $\mathcal{G}_U[G_0^{-1}]$:

$$\mathcal{G}_U[G_0^{-1}] = \frac{1}{T}\frac{\delta\Omega_U[G_0^{-1}]}{\delta G_0^{-1}} = -\frac{1}{Z_U[G_0^{-1}]}\frac{\delta Z_U[G_0^{-1}]}{\delta G_0^{-1}}. \tag{6.8}$$

with the property $\mathcal{G}_U[G_0^{-1}] = G_{t,U}$. We define a function $G_U[\Sigma]$:

$$\mathcal{G}_U[G_U[\Sigma]^{-1} + \Sigma] = G_U[\Sigma]. \tag{6.9}$$

A function $F_U[\Sigma]$ can be defined as

$$F_U[\Sigma] = \Phi_U[G_U[\Sigma]^{-1} + \Sigma] - Tr\ln G_U[\Sigma]. \tag{6.10}$$

We can calculate the equation which is given as

$$\frac{1}{T}\frac{\delta F_U[\sigma]}{\delta\Sigma} = -\mathcal{G}_U[G_U[\Sigma]^{-1} + \Sigma](\frac{\delta G_U[\Sigma]^{-1}}{\delta\Sigma} + 1) - G_U[\Sigma]^{-1}\frac{\delta G_U[\Sigma]}{\delta\Sigma}, \tag{6.11}$$

and

$$\frac{1}{T}\frac{\delta F_U^{[}\Sigma]}{\delta\Sigma} = -G_U[\Sigma]. \tag{6.12}$$

The Legendre transform of $F_U[\Sigma_U]$ can be constructed:

$$\Phi_U[G] = F_U[\Sigma_U[G]] + Tr(\Sigma_U[G]G). \tag{6.13}$$

The evaluation of the Luttinger-Ward functional at G yields

$$\Phi_U[G_{t,U}] = \Omega_{t,U} - Tr\ln G_{t,U} + Tr(\Sigma_{t,U}G_{t,U}) \tag{6.14}$$

We can obtain

$$\frac{1}{T}\frac{\delta\Phi_U[G]}{\delta G} = \Sigma_U[G] \tag{6.15}$$

Fast-update formulars

It is necessary to calculate the inverse matrix to obtain the wight values and the Green's function in the CT QMC method. Instade of usual precedures which is taken N^3 operations, there is the fast-update formular which is taken N^2, where N is the matrix size. Matrices can be inverted blochwise by using the following analytic inversion formula:

$$H = \begin{pmatrix} A & B \\ C & D \end{pmatrix},$$

$$M_{N+1} = \begin{pmatrix} A & B \\ C & D \end{pmatrix}^{-1} = \begin{pmatrix} A^{-1} + A^{-1}B(D - CA^{-1}B)^{-1}CA^{-1} & -A^{-1}B(D - CA^{-1}B)^{-1} \\ -(D - CA^{-1}B)^{-1}CA^{-1} & (D - CA^{-1}B)^{-1} \end{pmatrix}$$

where H, A, B, C, and D are matrix sub-blocks of arbitary size. For the step $N+1$ the inversion of A matrix is A^{-1}=M_N. Let us define $\triangle = M_{N+1}^{-1} - M_N^{-1}$ and M_N is extended to be a $(N+1) \times (N+1)$ matrix with $M_{N+1,i}$=0, $M_{i,N+1}$=0 and $M_{N+1,N+1}$=1 (it does not change the ratio of determinants). The QMC weight function is

$$\frac{\det H}{\det A} = \frac{\det M_N}{\det M_{N+1}}. \tag{6.16}$$

The determinant ratio, which is related to the QMC weight function, is given as

$$\frac{M_N}{M_{N+1}} = (1 + \triangle M_N), \tag{6.17}$$

where the $(1 + \triangle M_N)$ is

$$(1 + \triangle M_N) = \begin{pmatrix} 1 & B \\ CA^{-1} & D \end{pmatrix}.$$

Thus is the $\det[\frac{M_N}{M_{N+1}}]$ is $(D - CA^{-1}B)$. Now we would like to calculate the inverse matrix M_{N+1}. For simple notation we define $D - CA^{-1}B$ as λ. Since we know the A^{-1} and λ, we can finally calculate the inverse matrix M_{N+1} which is given by

$$M_{N+1} = \begin{pmatrix} A & B \\ C & D \end{pmatrix}^{-1} = \begin{pmatrix} A^{-1} + A^{-1}B\lambda^{-1}CA^{-1} & -A^{-1}B\lambda^{-1} \\ -\lambda^{-1}CA^{-1} & \lambda^{-1} \end{pmatrix}$$

The formular of the step N-1 is similar to that of the step N+1.

Measurement of the Green's function for the CT QMC method

In the CT QMC method the Green's function is calculated by

$$G(i\omega_n) = G_0(i\omega_n) - G_0(i\omega_n)[\frac{1}{\beta}\sum_{i,j} M_{i,j} e^{i\omega_n(\tau_i - \tau_j)}]G_0(i\omega_n). \tag{6.18}$$

(K $\times$N) operations are requared, where K is the matrix size of $M_{i,j}$ and N is the number of Matsubara frequeyncy. However, we need not to calculate all Matrix elements in Eq. (6.18) from the idea of the fast-update formular. The $M_{i,j}$ matrix is

$$\begin{pmatrix} A^{-1} + A^{-1}B\lambda^{-1}CA^{-1} & -A^{-1}B\lambda^{-1} \\ -\lambda^{-1}CA^{-1} & \lambda^{-1} \end{pmatrix}.$$

We only need to calculate the matrics which are defined as

$$B[k, i\omega_n] = B[k] \times e^{i\omega_n \tau_i} \tag{6.19}$$

$$C[k, i\omega_n] = C[k] \times e^{-i\omega_n \tau_j}, \tag{6.20}$$

where K is the matrix size. Since we know $A^{-1}[k, i\omega_n]$ and the λ through the fast-update formular, the Green's function is also updated by operation of $\square kN$.

Tangent versus secant tetrahedron method

For this part I learned the work, which was presented in Phy. Rev B 57, 2217 (1998) [55], will follow notation of this paper. The density of states is given as

$$D(\epsilon) = -\frac{1}{\pi}\Im G(\epsilon). \tag{6.21}$$

Clearly, the Green's function $G(\epsilon)$ is

$$G(\epsilon) = \int dk \frac{1}{\epsilon - \omega(k) + i\alpha} = \int dk \frac{1}{\epsilon - E(k)}, \tag{6.22}$$

where $\omega(k)$ is real, α is very small positive value and $E(k) = \omega(k) - i\alpha$. The integral of Eq. (6.22) runs over one tetrahedron, and the contributations from all tetrahedrons have to be summed up. For prectical calculation we will define the number of the corners of the tetrahedron by μ=0, 1, 2, and 4 and the energy is determined by $E_\mu = E(k_\mu)$. The linearly interpolated function $E(k)$ is

$$E(k) = E_0 + \sum_{l=1}^{3} (E_l - E_0) r_l \dot{k}. \tag{6.23}$$

If we expand the k vector in the triple k_i by $k = \sum_{i=1}^{3} x_i k_i$, then we can tranform $E(k)$ into

$$E(x) = E_0 + \sum_{l=1}^{3} (E_l - E_0) x_l. \tag{6.24}$$

Finally, the Green's function is given as

$$G(\epsilon) = \int_0^1 dx_1 \int_0^{(1-x_1)} dx_2 \int_0^{(1-x_1-x_2)} dx_3 \frac{1}{\epsilon - E_0 - \sum_{l=1}^{3} (E_l - E_0) x_l} \tag{6.25}$$

By an analytical integration we obtain final result:

$$G(\epsilon) = \sum_{\mu=0}^{3} \frac{1}{P_\mu} (\epsilon - E_\mu)^2 [1 + (3 + (\epsilon - E_\mu) S_\mu) \times \ln(\epsilon - E_\mu)], \tag{6.26}$$

where $P_\mu = \prod_{\nu=0, \nu\neq\mu}^{3} (E_\nu - E_\mu)$ and $S_\mu = \sum_{\nu=0, \nu\neq\mu}^{3} \frac{(A_\nu - A_\mu)}{(E_\nu - E_\mu)}$.

List of Figures

Bibliography

[1] W. Kohn and L. Sham, Phys. Rev. 140 (4A): A1133-A1138 (1965)

[2] N. Mott, Proc. Phys. A, 62, 416 (1949)

[3] J. Bendorz and K. Muller, Z. Phys. B 64, 189 (1986)

[4] S. Kondo et al, Phys. Rev. Lett. 78, 3729 (1997)

[5] A. Georges, G. Kotliar, W. Krauth and M. Rozenberg, Rev. Mod. Phys. 68, 13 (1996)

[6] W. Metzner and D. Vollhardt, Phys. Rev. Lett. 62, 324 (1989)

[7] A. Georges and G. Kotliar, Phys. Rev. B, 45, 6479 (1992)

[8] M. Hettler, A. Tahvildar-Zadeh, M. Jarrell, T. Pruschke and H. Krishnamurthy, Phys. Rev. B 58, R7475 (1998)

[9] T. Maier, M. Jarrell, T. Pruschke and M. Hettler, Rev. Mod. Phys. 77, 1027 (2005)

[10] G. Kotliar, S. Savrasov, G. Palsson and G. Biroli, Phy. Rev. Lett. 87, 186401 (2001)

[11] A. Rubtsov, M. Katsnelson and A. Lichtenstein, Phys. Rev. B 77, 033101 (2008)

[12] T. Marier, M. Jarrell, T. Schulthess, P. Kent and J. White, Phys. Rev. Lett. 95, 237001 (2005)

[13] A. Rubtsov, V. Savkin and A. Lichtenstein, Phys. Rev. B 72, 035122 (2005)

[14] P. Werner, A. Comanac, L. de Medici, M. Troyer and A. Millis, Phys. Rev. Lett. 97, 076405 (2006)

[15] J. Hirsch and R. Fey, Phys. Rev. Lett. 56, 2521 (1986)

[16] S. Okamoto, A. Fuhrmann, A. Comanac and A. Millis, Phys. Rev. B 71, 235113 (2005)

[17] S. Berner, H. Hafermann, A. Rubtsov, M. Katsnelson and A. Lichtenstein, Phys. Rev. B 77, 195105 (2008)

[18] Gang Li, Hunpyo Lee and Hartmut Monien, Phys. Rev. B 78, 195105 (2008)

[19] H. Hafermann, Gang Li, A. Rubtsov, M. Katsnelson and A. Lichtenstein, arXiv:0812.2456 (2008)

[20] F. Wang and D. Landau, Phys. Rev. Lett. 86, 2050 (2001)

[21] F. Wang and D. Landua, Phys. Rev. E 64, 056101 (2001)

[22] M. Troyer, S. Wessel and F. Alet, Phys. Rev. Lett. 90, 120201 (2003)

[23] Z. Shen, Phys. Rep. 253, 1 (1995)

[24] H. Ding, Phys. Rev. Lett. 76, 1533 (1996)

[25] S. Kancharla and S. Okammoto, Phys. Rev. B 75, 193103 (2007)

[26] A. Fuhrmann, D. Heilmann and H. Monien, Phys. Rev. B 73, 245118 (2006)

[27] K. Bouadim, G. Batrouni, F. Hebert and R. Scalettar, Phys. Rev. B 77, 144527 (2008)

[28] H. Park, K. Haule and G. Kotliar, Phys. Rev. Lett. 101, 186403 (2008)

[29] A. Toschi, M. Capone, C. Castellani and K. Held, arXiv:0712.3723 (2007)

[30] O. Trovarelli et al, Phys. Rev. Lett. 85, 626 (2000)

[31] R. Mckenzie, Science 278, 820 (1997)

[32] Y. Imai and N. Kawakami, Phys. Rev. B 65, 233103 (2002)

[33] H. Morita, S. Watanabe and M. Imada, J. Phys. Soc. Jpn. 71, 2109 (2002)

[34] T. Mizusaki and M. Imada, Phys. Rev. B 74, 014421 (2006)

[35] N. Bulut, W. Koshibae and S. Maekawa, Phys. Rev. Lett. 95, 037001 (2005)

[36] A. Aryanpour, W. Pickett and R. Scalettar, Phys. Rev. B 74, 085117 (2006)

[37] J. Merino, B. Powell and R. McKenzie, Phys. Rev. B 73, 235107 (2006)

[38] J. Merino, M. Dumm, N. Drichko, M. Dressel and R. McKenzie, Phys. Rev. Lett. 100, 086404 (2008)

[39] O. Parcollet, G. Biroli and G. Kotliar, Phys. Rev. Lett. 92, 226402 (2004)

[40] T. Ohashi, T. Momoi, H. Tsunetsugu and N. Kawakami, Phys. Rev. Lett. 100, 076402 (2008)

[41] T. Ohashi, N. Kawakami and H. Tsunetsugu, Phys. Rev. Lett. 97, 066401 (2006)

[42] S. Moukouri and M. Jarrell, Phys. Rev. Lett. 87, 167010 (2001)

[43] Y. Okamoto, H. Arugu-katori and H. Takagi, Phys. Rev. Lett. 99, 137207 (2007)

[44] G. Chen and L. Balents, Phys. Rev. B 78, 094403 (2008)

[45] M. Lawler, H. Kee, Y. Kim and A. Vishwanath, Phys. Rev. Lett. 100, 227201 (2008)

[46] J. Hopkinson, S. laskov, H. Kee and Y. Kim, Phys. Rev. Lett. 99, 037201 (2007)

[47] Y. Zhou, P. Lee, T. Ng and F. Zhang, Phys. Rev. Lett. 101, 197201 (2008)

[48] S. Lefebvre00 et al, Phys. Rev. Lett. 85, 5420 (2000)

[49] F. Kagawa, T. Lito, K. Miyagawa and K. Kanoda, Phys. Rev. B 69, 064511 (2004)

[50] M. Rosenberg, R. Chitra and G. Kotliar, Phys. Rev. Lett. 83, 3498 (1999)

[51] E. Gull, P. Werner, M. Troyer and A. Millis, cond-mat/08053778 (2008)

[52] D. Podolsky, A. Paramekanti, Y. Kim and T. Senthil, cond-mat/0811.2218

[53] M. Potthoff, cond-mat/0406671 (2004)

[54] J. Luttinger and J. Ward, Phys. Rev. 118, 1417 (1960)

[55] M. Taut, Phys. Rev. B 57, 2217 (1998)

[56] E. Gull, P. Werner, X. Wang and M. Troyer and A. Millis, EPL 84. 37009 (2008)

[57] E. Gull, P. Werner, A. Millis and M. Troyer, Phys. Rev. B 76, 235123 (2007)

[58] B. Kyung, J. Landry, D. Poulin and A. Tremblay, Phys. Rev. Lett. 90, 099702-1 (2003)

[59] G. Moeller, V. Dobrosavljevic and A. Ruckenstein, Phys. Rev. B 59, 6846 (1999)

[60] Journal of Physics: Conference Series 145, 012013 (2009)